The Pennsylvania State University

The Graduate School

Department of Electrical Engineering

MICROMACHINED SWITCHES AND CANTILEVER ACTUATORS BASED ON PIEZOELECTRIC LEAD ZIRCONATE TITANATE (PZT)

A Thesis in

Electrical Engineering

by

Steven J. Gross

Submitted in Partial Fulfillment
of the Requirements
for the Degree of

Doctor of Philosophy

August 2004

The thesis of Steven J. Gross was reviewed and approved* by the following:

Thomas N. Jackson
Robert E. Kirby Chair Professor of Electrical Engineering
Thesis Co-Advisor, Co-Chair of Committee

Srinivas Tadigadapa
Associate Professor of Electrical Engineering
Thesis Co-Advisor, Co-Chair of Committee

Susan Trolier-McKinstry
Professor of Ceramic Science and Engineering

Kenji Uchino
Professor of Electrical Engineering

Chris Rahn
Professor of Mechanical Engineering

W. Kenneth Jenkins
Professor of Electrical Engineering
Head of the Department of Electrical Engineering

*Signatures are on file in the Graduate School

Abstract

In this work, the first piezoelectric surface-micromachined switches were developed and demonstrated. To date, MEMS switches based on electrostatic actuation have exhibited excellent RF performance including low loss, high isolation, and low power consumption. Many systems stand to benefit from these switches and other RF MEMS devices. A significant drawback to MEMS switches so far has been the high actuation voltages, typically greater than 50V. This work has empirically confirmed that exploiting piezoelectric actuation offers a considerable advantage over electrostatics. A switching time of 2 μs was measured with only 30 volts applied. This is one of the fastest reported switching speeds for MEMS device, as well as a comparatively low actuation voltage.

The piezoelectric switches in this study were designed based on unimorph cantilevered bender actuators. Electrical switching was accomplished by a metal contact on the end of the actuator that makes and breaks a connection with a gold transmission line. A low-stress silicon nitride was used as the structural layer. Sol-gel deposited lead zirconate titanate (PZT) films were selected as the actuation material due to their comparatively high piezoelectric response. These films exhibited good ferroelectric properties with remanent polarizations of 20-25 $\mu C/cm^2$ and coercive fields of 50 kV/cm. Gold interdigitated electrodes were used to pole and drive the microactuators and switches. The PZT, and remaining films in the stack, were patterned using ion-beam etching. Hard chromium and titanium masks, used in conjunction with oxygen, were developed for ion milling, and found to have an etch-rate selectivity over PZT of roughly 3 to 1. The devices were released by etching sacrificial silicon in gas-phase xenon difluoride.

Released cantilevers had a propensity for upward curvature due to unbalanced residual stresses in the films. A systematic approach, based on varying the PZT thickness, was devised to produce flat cantilevers, and ultimately, functioning switches. An investigation into the stress mechanisms was undertaken to gain insight into the stress mechanisms with the aim of improving yield. The study revealed that the stress of the sol-gel deposited zirconia was not stable when exposed to the atmosphere. Presumably, this was a result of hydration due to the porous nature of the film. Reactively sputtered titania films were explored as an alternative barrier layer. PZT films deposited on 100 nm of titania exhibited good ferroelectric properties, comparable to those deposited on zirconia. Unimorph actuators using titania were fabricated, and the field-induced deflection was measured. Due to the symmetric nature of the bimorph, and its predicted superior performance, this structure was explored as an alternative to the unimorph. It was found that the curvature of these structures could be controlled post-release by increasing the annealing temperature. Based on these initial results, bimorph actuators look very promising for MEMS switches.

The deflection of a zirconia buffered actuator, 280μm in length, was measured to be 10 μm at 100 volts (160 kV/cm). A 280 μm long titania actuator exhibited a 15 μm at 200 volts (333 kV/cm). A switch with a tapered geometry was used to measure the transmitted RF power as function of frequency, and was found to have an isolation of more than 60 dB up to 10 MHz.

Table of Contents

List of Figures

List of Tables

Acknowledgements

I express my most sincere gratitude to all the individuals, who have help make this work possible. I thank my advisors, Srinivas Tadigadapa and Thomas Jackson for their guidance and support. My thanks also go out to my committee members. Also, I have to recognize the much-appreciated assistance given to me by my friends and coworkers: Ravi Jayraman, Eunki Hong, Qingqi Zhang, Nazanin Bassiri Gharb, Chris Nordquist, Shelby Kuo, Chris Sheraw, Jon Nichols, Lisong Zhou, Karthik Shankar, Cheryl George, Soyoun Jung, Jeffery Huang, Ivan Divlianski, Seugn-Gu Lim, Randy Koval, Hagen Klauk, Lloyd Peterson, Srivatsa Srinath, and anybody else who I'm forgetting. Lastly, I offer my most heartfelt thanks to my parents, Joseph and Maria Pia Gross, my sister Paola, Diane Chan and Yuyan Zhang for their unending support and encouragement throughout the years.

Chapter 1

Introduction & Objectives

1.1 MEMS switches & RF switching

The switching of an electrical signal is arguably the most fundamental aspect of any electronic system. Discussed here is a new type of switching technology, part of a larger group of microdevices that will alter the performance and design of many RF electronic systems. Existing RF switching technologies are listed and a comparison is made.

1.1.1 RF MEMS

In the last several decades, there has been explosive growth in the number and functionality of devices in the communications industry. This advancement is coupled to, and is a result of, the tremendous success of the semiconductor and electronics industries that have enabled large amounts of data to be processed quickly and cheaply. The demand for smaller and more versatile products such as cell phones, internet-capable portable computers, GPS receivers, and remote sensors is driving greater integration and the development of novel technologies to realize these next-generation requirements.[1] RF MEMS, which include voltage-tunable capacitors, micromachined inductors, thin-film and micromechanical resonators, is emerging as a technology able to fulfill many of these next generation requirements. Other application areas that stand to benefit include radar systems for military and civilian use, satellite communications, global positioning and instrumentation systems.[2] Though not yet fully mature, MEMS appear attractive for RF and wireless applications for many reasons including: miniaturization and integration, power consumption, functionality, and batch fabrication. The required performance, such as sharp resonance (high Q), of discrete passive components has yet to be matched by IC's.[1] The need for these off-chip components limits the further miniaturization of some systems. RF MEMS are more suited for integration, and thus a significant reduction in size is attainable along with a decrease in power consumption. The availability of components with improved performance will allow greater flexibility is system design, and batch fabrication will potentially reduce cost when replacing discrete components. This is very important for portable devices when the power source is made smaller along with the device. Due to superior performance, RF MEMS switches could be used as the T/R switch that connects an antenna to either the transmitter or receiver in the duplexer. Additionally, MEMS could replace the switches in the delay elements in phased arrays, in generating the desired waveform in digital modulation, and in routing a signal to an instrument.[3]

1.1.2 MEMS switches

In 1979, K.E. Peterson at IBM introduced a new class of electrical switching device.[4] Using existing microfabrication technology developed for semiconductor processing, he was able to demonstrate a micro-relay with a moving arm of less than 1/10 of a millimeter long. Although not specifically designed for AC signals, the potential benefits for high frequency applications were readily apparent. He was one of the first in the new field of micro-electro-mechanical systems (MEMS) that included optical modulators made from moveable silicon oxide membranes[5], ink jet nozzles[6], and various types of sensors.[7] Sponsored by the Defense Advanced Research Projects Agency (DARPA), in 1991 L. Larson at Hughes realized a similar MEMS switch with outstanding RF performance up to 50 GHz. Spurred on from his success, by 1995 Rockwell Science Center had a DC to 60 GHz device and Texas Instruments was testing their 10 to 120 GHz switch. By now, the advantages over semiconductor-based devices were evident, as was the commercial potential, and by 2001 there were over thirty electronics companies and many research universities pursuing the technology.

To date, MEMS switches have demonstrated excellent broadband RF performance, from DC to 100GHz, with very low insertion losses in the on-state and high isolation in the off-state. Power consumption is extremely low in most switches, which is an important factor, especially in portable systems. Inherently, switching is more linear resulting in lower signal distortion and intermodulation products compared to semiconductor switches. Due to batch fabrication and micromachining, the prepackaged fabrication cost is typically low and in some cases, integration with signal conditioning electronics is possible. Switching speeds are slow compared to semiconductor switches, on the order of microseconds and even milliseconds, and although this is adequate for many RF applications, certain systems could benefit from faster devices.[8] The voltage required for reliable operation remains high at 20-100 volts, which necessitates step-up electronics to boost the voltage in certain systems. Signal power has been limited to around 200mW with a couple exceptions demonstrating 500 mW. Reliability and packaging of mature switches are still key issues that limit full commercialization, and are areas of on going research. As a result of the costly hermetic packaging, to date, MEMS switches have been limited to defense related and high-value commercial applications.[9]

1.1.3 Switching parameters

Several types of technologies exist for switching RF signals and the choice depends on the application. Designing an RF system requires knowledge of the device operating parameters. Select parameters for RF switching devices are listed and defined below.

Isolation is a measure of the RF power that leaks through to the output as a result of capacitive coupling and surface leakage in the off-state. For a two port device, the ratio of the transmitted (port 2) to incident (port 1) wave amplitudes is given by the scattering parameter S_{21}.[10] The isolation is then given as the square of the S - parameter: $|S_{21}|^2$.

Insertion loss is the power absorbed by a device, and is usually expressed in decibels. The bulk resistivity of the transmission line, if included as part of the device, and contact resistance contribute to the insertion loss at lower frequencies. Skin effects dominate at higher frequencies. The insertion loss is the incident power minus the reflected and transmitted power. When the device is well matched and the reflected power is minimal, the insertion loss can be given by, $1 - |S_{21}|^2$, but sometimes simply S_{21} is quoted. Both the insertion loss and isolation are functions of the frequency.

Switching time and speed - Although there is inconsistency in the literature with these terms, the switching time will be defined as the time necessary to change the state of the device from on to off, and vise versa. Herein, the switching on time, τ_{on}, is defined as the time required for the output power to reach 90% of full value and the off time, τ_{off}, as the time required to reach 10% of the off state. Figure 1.1 illustrates how both τ_{on} and τ_{off} are measured with respect to the control signal. The time required for the output to change from 10% to 90% (90% – 10%) is known as the rise time (fall time). The switching on time is also referred to as the switching speed.

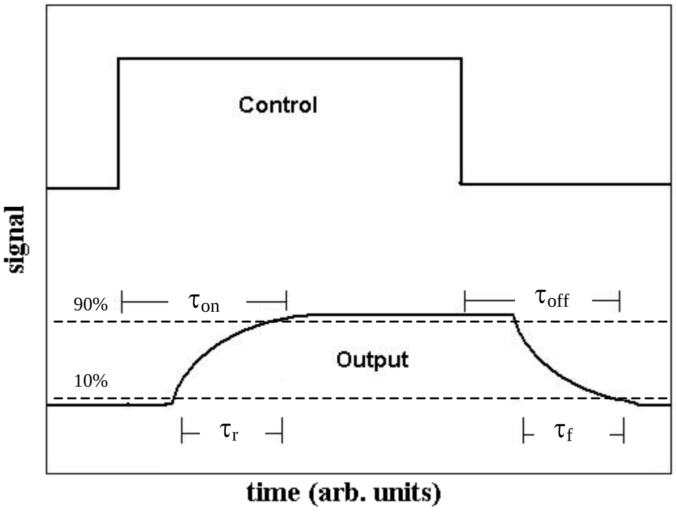

Figure 1.1 Illustration of switching time, τ_{on}, and $\tau_{off,}$, and the rise $\tau_{r,}$ and fall τ_f times.

Equivalent Series Resistance, R_s, is the real portion of the impedance of a switch, configured in series, in the on state. R_s results in a degradation of signal and contributes to the loss.

A ***Figure of Merit*** *(FOM)* is sometimes used to compare various switching devices and is defined as the product of the off-state capacitance, and the on-state resistance. It is derived from the ratio of the on-state and off-state impedance, and is a function of frequency. In general, a lower FOM is better but the specific application will dictate the optimum choice.

1.1.4 RF switching technologies

As with any technology, the intended application ultimately dictates the operating specifications. The most commonly employed RF switching devices today can be classified as either mechanical, or relay type, and semiconductor based – each occupying a specific niche of the performance spectrum. An accurate comparison between switching technologies is difficult to make since the performance parameters vary widely depending on the design and application. Table 1.1 provides typical values for a general comparison.

Table 1.1 Comparison of RF switching devices

	Relays	FET[1]	PIN[2]	MEMS
Switching Time, τ_{on}	>5 ms	1-100 ns	1 – 100 ns	1-300 μs
Resistance R_s (Ω)	0.005 –0.01	4 – 6	2 - 4	0.5 - 5
Insertion loss 1 GHz (dB)	0.01 - 0.3	0.4 – 2.5	0.3 – 1.2	0.2 – 0.5
Isolation 1-30 GHz (dB)	50-80	20 - 30	20 - 30	20 - 50
Actuation Voltage (V)	12-30	3-50	3-5	5-100
Power consumed (mW)	400	0.05 – 0.1	5 - 100	0.05 – 0.1
Signal Power (W)	100 – 1500 kW	<10	<10	0.2 – 0.5
FOM (fs)	N/A	500	110-220	0.01-12

[1] Field Effect Transistor, [2] P-type Intrinsic N-type, Sources: Ref. 6,5,10

For high power (kW to MW) applications such as television and radio broadcasting electromagnetic relays are typically used. RF relays are available in various configurations, normally open or closed, with coaxial or waveguide connection ports. These devices exhibit high isolation due to the large gap between contacts and low insertion losses due to direct metal contact. The signal bandwidth ranges from dc to as high as 26 GHz for specific models.[11] Although relay switches exhibit good RF characteristics, their comparatively large size limits integration, and results in slow switching speeds.

For solid-state switches, the impedance of the semiconductor is controlled by an electric field. The lack of moving components allows much faster switching speeds - on the order of nanoseconds. Batch fabrication reduces per unit cost and allows integration, which makes possible the miniaturization of the final system – a key requirement for portable equipment. The most frequently used switching element for RF applications is the silicon diode based on a P-type Intrinsic N-type (PIN) structure. When used as a switching element, PIN diodes are turned on or off by a DC voltage. Design configurations include either series or shunt, and single or multi-throw. When forward biased, electrons and holes are injected into the intrinsic region. The charge stored in this region is due to the finite lifetime of these carriers. Below a critical frequency, the PIN diode behaves as a p-n junction, with the diode's incremental resistance determined by the I-V behavior at the quiescent point. At frequencies above the transit time of the carriers, the series resistance becomes a strong function of the width of the I-layer and the charge stored. In zero or reverse bias, the device can be modeled as a parallel plate capacitor, the value of which can be calculated from the width of the I-layer. To attain a high isolation and break down voltage, the width of the I-layer is increased.[12] This however also drives up the on-state insertion losses. The performance depends on the geometry, impurities in the intrinsic region, and on parasitics arising from packaging. The choice of diode depends on the circuit, but tradeoffs are inevitable. Field effect transistors (FET) produced from silicon or GaAs are also used as RF switching elements. In these three terminal devices, the channel current is controlled by a voltage applied to the gate. This makes the on-state power requirements lower than with PIN diodes. Silicon FETs in general can handle large RF signal power at lower frequencies but the performance degrades at higher frequencies. The higher electron mobility of GaAs allows for faster switching and better high frequency operation than with silicon. Typically, however, at signal frequencies above 1 GHz, solid-state devices exhibit poor isolation in the off-state and a large insertion loss in the on-state.[13]

1.1.5 MEMS switch configurations

Numerous configurations for MEMS switches are possible and most have been demonstrated. Switching in MEMS devices is accomplished by the deflection of a freestanding structure to cause a metal-to-metal contact or capacitive coupling with the transmission line. This deflection has been achieved using various actuation methods, including electrostatic,[14] electromagnetic,[15] thermal,[16] and piezoelectric.[17] To date, electrostatic actuation is the most prevalent, due in part to the simplicity of design and fabrication, as well as the achieved level of performance. Mechanically, the structure can be designed to deflect vertically, normal to the substrate, or laterally. Laterally actuating devices tend to have larger moving components and hence exhibit slower switching speeds. Vertically deflected beam structures are designed as either bridge type, fixed at two ends, or cantilevered - free at one end. The beam is arranged either perpendicular to the signal line with two contact points, or in-line as part of the transmission line with only a single contact. Electrically, the device is configured in a shunting mode and must be designed accordingly. Shown below are two electrostatic switches that incorporated several of the design configurations. Figure 1.2 shows an in-line, series, cantilever-type DC-contact (metal to metal) arrangement with a strip line transmission line. A bridge-type, capacitive shunt switch with coplanar wave-guides is shown in figure 1.3. The switch configuration and material properties determine the RF performance characteristics. Electromagnetic models of two common MEMS switch configurations are presented to reveal the origins of certain performance parameters.[9] An ideal series switch introduces infinite signal isolation in the up-state and zero losses in the down-state. Series switches typically have metal-to-metal contacts and can operate down to DC. Figure 1.4 shows an equivalent lumped element model for a series DC-contact switch and transmission line (t-line) in the up-state (1.4a) and down-state (1.4b). Z_o is the

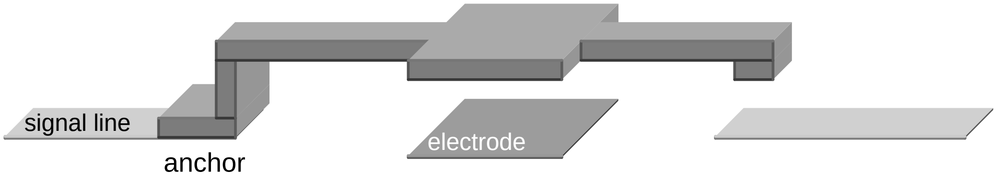

Figure 1.2 Representation of an in-line, series, cantilever-type DC-contact (metal to metal) electrostatic MEMS switch with strip line transmission line.

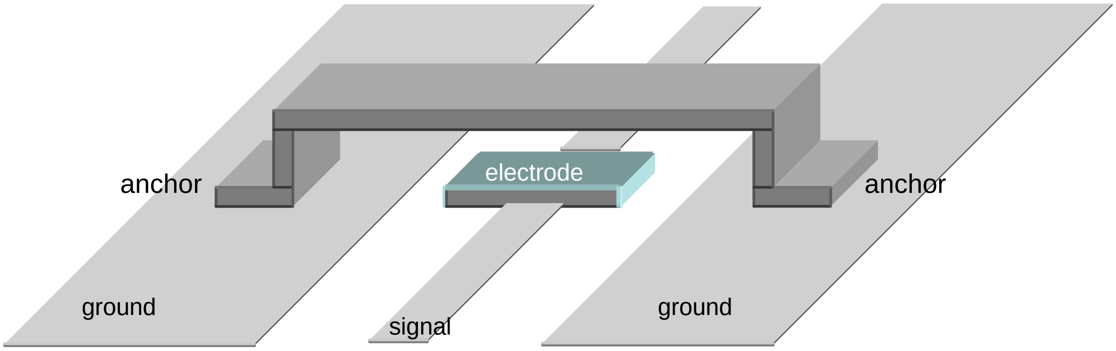

Figure 1.3 Representation of a bridge-type, capacitive shunt electrostatic MEMS switch with coplanar wave guide.

characteristic impedance of the t-line and Z_A is the impedance of the moving structure. The total capacitance in the up-state, C_u, is comprised of the two series capacitances, $C_{s,}$ between the contacts and t-lines (only one for in-line designs) and a capacitance, C_p, in parallel between the open ends of the t-lines. The series capacitance, C_s, is usually the larger of the two, and is a function of the gap spacing. Values for C_u are typically around 2 to 6 fF. The isolation is a function of the of the up-state and given as,[9]

$$\left|S_{21}\right|^2 \cong 4 Z_0 \omega^2 C_u^2 \tag{1.1}$$

In the down state (1.4b), the switch can be modeled as a section of t-line with one or two contact resistances, R_c, in series. The contact resistance is a function of the metal used, and decreases with increasing contact force. The total series resistance, R_s (1-3Ω)$_,$ is the sum of all the resistances, but is dominated by R_c. The loss can be expressed as R_s/Z_o and

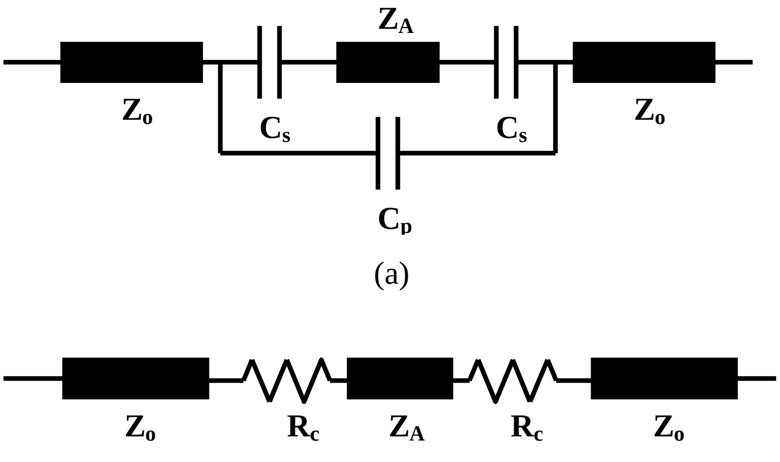

(a)

(b)

Figure 1.4 Equivalent circuit model for a typical MEMS series DC-contact switch in the off-state (a) and the on-state (b).

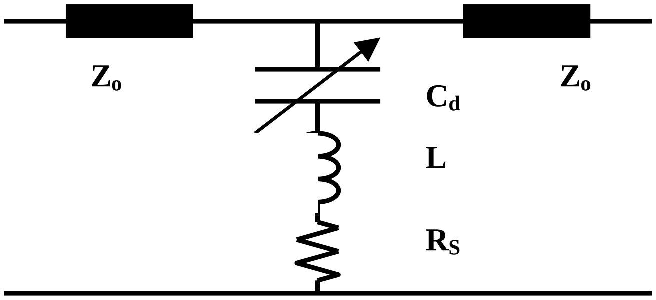

Figure 1.5 Equivalent circuit model for a typical MEMS capacitive shunt switch.

is nearly frequency independent. Typical values for the loss in MEMS series switches are 0.1 to 0.3 dB. Based on this model, a larger gap spacing decreases the up-state capacitance, C_u, which decreases S_{21} (improves the isolation). A larger gap however increases the required actuation voltage.

In the down-state, by providing a short circuit to ground, the ideal shunt switch exhibits very good isolation. In the up-state position, the ideal switch behaves as a simple transmission line with zero insertion loss. Shunt switches typically are capacitive, and are better suited for higher frequency operation than are series switches. A circuit model for a capacitive shunt switch is shown in figure 1.5 with the capacitance determined by the position of the beam. The parallel plate down-state capacitance, C_d, can be calculated using the thickness and permittivity of the dielectric film. Since this capacitance is small (2-5pF), capacitive switches typically are utilized above 8GHz.[9] The up-state capacitance can be modeled as two parallel plate capacitors in series; one filled with air, and the other with the dielectric film. The inductance and capacitance in series introduce an electric resonance. In the up state, this resonance is typically around several hundred GHz. For both series and shunt switches the values for the lumped elements can be extracted from the measured s-parameters.

Listed in Table 1.2, is a select group of electrostatic MEMS switches with corresponding characteristics, electrical and mechanical configuration, and key dimensions. The Raytheon switch, listed first in the table and shown in figure 1.6, is an aluminum bridge

Table 1.2 Comparison of MEMS RF switches for select parameters

	RAYTHEON	U. MICH.	ROCKWELL	MOTOROLA	NORTH-EASTERN U.
Configuration	b,t,p	b,t,p	b,s,m	c,s,m	c,s,m,i
Length (μm)	270-350	500-700	250	140	75
Spring Const. (N/m)	6-20	1-10	15	35-40	>100
Actuation Voltage	30-50	6-20	50-60	40-60	60-80
Switching D/U(μs)	3/5	20-40(D)	8-10	2-4	2-3
Gap (μm)	3-5	4-5	2.5	2-3	0.6-1.2
Capacitance Ratio	80-120	30-50	_	_	_
Resistance (Ω)	0.25-0.35	0.2-0.3	0.8-2	1-2	1-1.5
Loss (dB)/(GHz)	0.07 /10-40	0.1/ 1-40	0.1/ 0.1-50	0.15/ 0.1-6	0.15/ 0.1-20
Isolation (dB)/(GHz)	20/ 10	25/ 30	50/ 4	44/ 2-4	40/ 4
Isolation (dB)/(GHz)	35/ 30	_	30/ 40	_	27/ 20
Years	1995-2000	1997-2000	1995-2001	2001	1999

s – series, t – shunt, c – cantilever, b - bridge, m – metal, p – capacitive, i - in-line Source: [9]

capacitive shunt switch and considered one of the most mature designs.[14] The University of Michigan device is also a bridge capacitive shunt design but the pull down electrodes are separate from the signal line. A unique feature is the serpentine like suspension supports used to reduce the spring constant and hence achieve a lower actuation voltage. Figure 1.7 shows an SEM image of the device from Northeastern University.[18] This is an example of an inline series design with an electroplated gold cantilever.

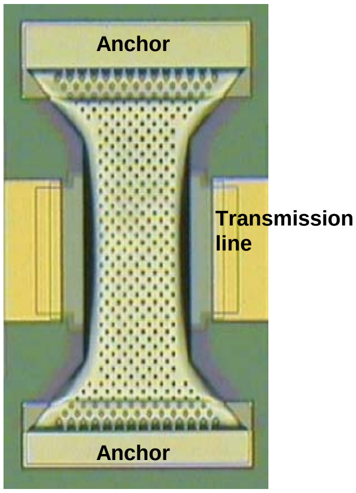

Figure 1.6 Microscope image of the Raytheon clamped-clamped capacitive shunt switch. [14]
© 1999 IEEE

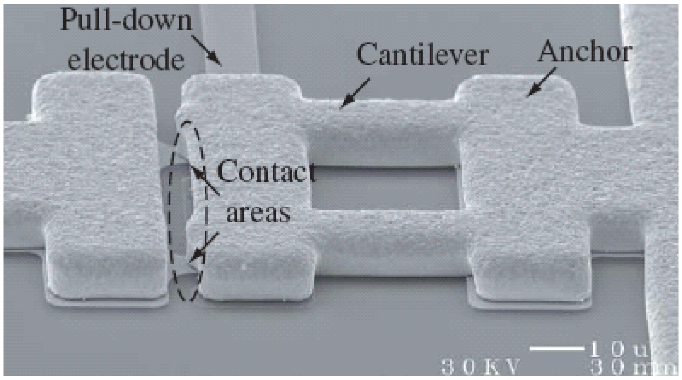

Figure 1.7 SEM image of the Northeastern University electrostatic cantilever switch.[18]

1.2 Actuation in MEMS

The principle component in the vast majority of microsystems is either a sensor or actuator. The choice of transduction mechanism depends on many factors, and ultimately dictates the performance of the system. Presented in this section are four of the most common mechanisms; thermal, magnetic, electrostatic and piezoelectric, and their use in microsystems.

1.2.1 Scaling laws

A starting point in a comparison of actuation mechanisms for microsystems inherently includes scaling laws. As the dimensions of a system are reduced isometrically, the relative influence of different physical and chemical effects is altered. A common example is the change in the surface area to volume ratio, as objects are made smaller. A simple yet revealing technique was put forth by Trimmer to determine how a given parameter, such as force, scales into the micro domain.[19] Based on this matrix formalism, forces that scale as [s^1] or [s^2], where s is a scaling parameter, are most promising when the transit time is decreased and the power per unit volume is increased. However, care must be taken to make the correct initial assumptions and to include non-linear behavior, such as the Paschen effect, that may arise at small dimensions.

1.2.2 Actuation mechanisms

Thermal Various forms of thermal actuation have been employed in microsystems including bimetallic, thermopneumatic, and shape memory alloys. Thermal actuation exploits the volume change of a material when heated. Since the strain it typically small, various structures are used to amplify the displacement. One structure, a bimetallic actuator, is composed of two materials with difference coefficients of thermal expansion bonded together. Alternatively, the buckling of a clamped beam is used. Shown in figure 1.8 is a MEMS switch based on this design. A thermopneumatic device operates by heating a gas trapped in a chamber and the resulting pressure rise causes a diaphragm to deflect.[20] In both cases, joule heating using resistive films is used for heating. Since the structure needs to cool, macro-scale thermal actuators are relatively slow. Microactuators however benefit from scaling by an increase in the heat transfer to mass ratio, allowing more rapid cooling. Power consumption is relatively high.

Magnetic In the macro-world, magnetic forces are dominant, as is evidenced by the wide spread use of electromagnetic motors, solenoids, and other devices. Based on simple scaling arguments, there is a significant reduction in the available force using

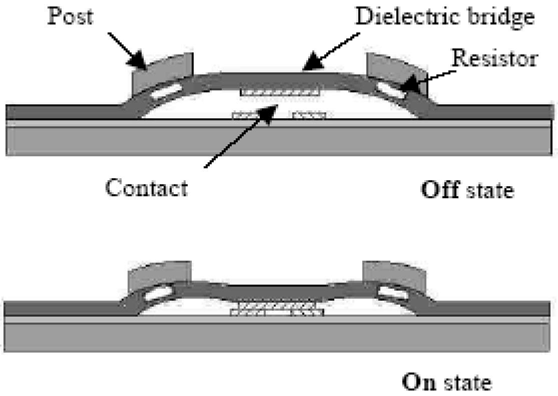

Figure 1.8 Thermally actuated RF MEMS switch based on a buckling fixed-fixed beam. [16] © 2001 IEEE

magnetic actuation - both electromagnetic and permanent magnet.[21] This however depends on the assumptions made in the analysis. The magnetic flux, and hence force, can be increased by increasing the current density through a coil. This generates more heat, but again in microsystems this is allowable to a certain degree. Compared with electrostatic actuation the power consumption and design complexity are typically higher, and integration is more difficult. Magnetic actuation may be justified for certain applications. A micromachined magnetic relay has been demonstrated and is being commercialized by Microlab Inc. The design incorporates a latching permalloy cantilever which results in a bistable operation.

Electrostatic To date, electrostatic actuation has been the most common method for MEMS switches because of favorable scaling, and a simpler fabrication that is usually CMOS compatible. An electrical potential applied to conducting electrodes separated by a dielectric results in an attractive electrostatic force between the electrodes. The force, F, on parallel plate electrodes can be derived from the change in internal energy, E, and given as,

$$F_z = \frac{\partial E}{\partial z} = \frac{1}{2}\frac{dCV^2}{dz} = \frac{1}{2}\frac{\varepsilon A V^2}{g^2} \tag{1.2}$$

where z is the direction normal to the plate electrodes, g is distance between the electrodes, A is the area, V is the voltage, C is the capacitance, and ε is the permittivity between the electrodes. The electrostatic force is a function of the distance, or gap, between the electrodes. This force increases exponentially as the gap is reduced. For MEMS switches, this force must be balanced by the restoring spring force of the structure. As the suspended beam is deflected and the gap is made smaller, a point of instability is reached at 2/3 the gap height for parallel plate electrodes.[9] The 'pull-in' voltage, at this position is given by,

$$V_p = \left(\frac{8kg^{3}}{27\varepsilon A} \right)^{1/2} \tag{1.3}$$

where k is the spring constant of the beam. Due to a positive feedback effect, at this point the beam collapses to the bottom electrode. The applied voltage is sometimes reduced after contact has been made.

Piezoelectricity In the late nineteenth century, the Curie brothers observed that the application of weight upon certain crystals, including quartz, resulted in the accumulation of charge on the crystal surfaces. This phenomenon became known as the direct piezoelectric effect, and is defined as the linear coupling between the electrical and mechanical domains. Likewise, by the converse piezoelectric effect, a strain is induced as a result of an applied electric field. Piezoelectricity is only observed in crystalline dielectrics whose structure lacks a center of symmetry. Of the 32 possible point groups, based on crystallographic symmetry, 21 are non-centrosymmetric and 20 are potentially piezoelectric.[22] The result of an asymmetry in structure, and therefore in potential, is a net displacement of the ions.[23] Another related electromechanical coupling found in all dielectric materials is electrostriction, in which the strain is proportional to the square of the field. Electrostrictive strain is typically positive while piezoelectric strain depends on the polarity of the applied field.

Equations 1.4 –1.7 relate the applied electric field E (V/m) and electric displacement D (C/m^2) to the mechanical stress σ (N/m^2) and stain S (m/m).[24] When used as superscripts these variables denote that this parameter is held constant. It is convenient to use the d coefficient (m/V or C/N) for actuation, and the e coefficient (C/m^2) for sensing mode.

Voigt or compressed matrix notation has been adopted to reduce the number of indices from three to two.[22] This allows the strain, for example, which is a second rank tensor to be written with only a single index. The third ranked piezoelectric tensor is then expressed as a matrix.

$$d_{ij} = \left(\frac{\partial S_i}{\partial E_j}\right)_{\sigma} = \left(\frac{\partial D_i}{\partial \sigma_j}\right)_{E} \tag{1.4}$$

$$e_{ij} = \left(\frac{\partial D_i}{\partial S_j}\right)_{E} = \left(-\frac{\partial \sigma_j}{\partial E_i}\right)_{S} \tag{1.5}$$

$$g_{ij} = \left(-\frac{\partial E_i}{\partial \sigma_j}\right)_{D} = \left(\frac{\partial S_j}{\partial D_i}\right)_{\sigma} \tag{1.6}$$

$$h_{ij} = \left(-\frac{\partial \sigma_j}{\partial D_i}\right)_{S} = \left(-\frac{\partial E_i}{\partial S_{jk}}\right)_{D} \tag{1.7}$$

1.2.3 Piezoelectric films for MEMS

Since piezoelectricity is expected to scale favorably,[19] there has been a growing interest in piezoelectric films for MEMS. The most common piezoelectric films are compared in table 1.3 opposite relevant material properties. Zinc oxide and aluminum nitride films are used commercially in film bulk acoustic resonators (FBAR) and surface acoustic wave (SAW) devices. MEMS devices using ZnO include CMOS integrated microphones, accelerometers and probes for atomic force microscopes.[25] To maximize the piezoelectric behavior, these films must be grown in the wurtzite structure with a strong c-axis orientation.[26] This can be achieved relatively easily by reactive magnetron sputtering at 230°C, and work has been conducted correlating deposition conditions and properties for ZnO. Although ZnO has higher piezoelectric constants, AlN exhibits a lower dielectric loss and higher acoustic velocity. Both are compatible with existing semiconductor fabrication lines.[27]

Certain polymers are also piezoelectric, including polyvinylidene fluoride (PVDF) and its copolymer with trifluoroethylene (PVDF-TrFE). P(VDF-TrFe) is the most widely used and exhibits the best performance.[28] The copolymer is capable of high strain (>5%) without fatigue and its unique properties make it attractive for certain applications such as micro-fluidic systems, artificial muscles and micro-reactors. The material can be deposited by solution or spin casting methods.

Table 1.3 Properties of piezoelectric films for MEMS applications

	AlN	ZnO	P(VDF-TrFE)	PZT (52/48)
d_{33} (pm/V)	3.4-5.1	7.5-12	-33	90-120
d_{31} (pm/V)	-2	-2.3	N/A	-40
ε_r	10-11	8-12	8	900-1300
Stiffness (GPa)	260-350	160	2-8	100

Source: [25,29,30,60,52]

Compared with the previous films, lead zirconate titanate (PZT) possesses significantly higher piezoelectric coefficients, which is a clear advantage for actuators.[31] PZT is discussed in detail in the next section.

1.3 Lead Zirconate Titanate (PZT) & PZT microsystems

Piezoelectric films are attractive for MEMS actuators and sensors due to their high energy density and low power requirements.[32] Compared to most piezoelectric films, the lead zirconate titanate (PZT) material system, exhibits a much larger piezoelectric response. This section introduces the fundamental properties of this ceramic and various PZT microactuators.

1.3.1 Ferroelectricity

Polarization Application of an electric field upon dielectric materials induces a small displacement in the center of charge. This electric polarization originates from a shifting of the electron cloud around atoms and a reorientation of ions or dipoles.[33] For linear dielectrics, the constant of proportionality between the applied electric field, E, and the polarization, P, is known as the relative electric susceptibility χ_e. It is easier to work with and measure the relative permittivity ε_r (dielectric constant) which is related to the susceptibility by,

$$\varepsilon_r = 1 + \chi_e = \frac{\varepsilon}{\varepsilon_o} \tag{1.8}$$

where ε and ε_o are the permittivity and vacuum permittivity respectively. For convenience, the displacement field is introduced to account for the free charge and is defined as,

$$D = \varepsilon_o E + P \tag{1.9}$$

Substitution of the P and χ_e, and the displacement field can be directly related to the electric field by,

$$D = \varepsilon E \tag{1.10}$$

For high permittivity dielectrics, the polarization is approximately equal to the displacement field.

Ferroelectricity Crystals that possess a polarization in the absence of an externally applied electric field, are known as polar, or pyroelectric. The material is said to be ferroelectric if this spontaneous polarization can be reoriented by applied electric field. Ferroelectricity is found in 10 of the 20 piezoelectric point groups. The allowed polarization directions within each grain are dictated by the crystal structure, and regions that share the same polar axis are known as domains. As depicted in figure 1.9,[34] ferroelectric materials exhibit hysteretic behavior in polarization versus electric field, which is a direct result of polarization switching. Domains aligned with the field grow at the expense of those that are not. Three parameters that quantify the ferroelectric behavior are labeled on the diagram. The maximum degree of alignment occurs at the highest field - the saturation polarization, P_s. Its value can be determined by the extrapolation of the linear potion of the loop back to the polarization axis.[35] A net remenant polarization, P_r, is present after removal of the applied field. A coercive field, E_c, is required to bring the total polarization to zero.

From theory put forth by Devonshire and work by Haun[36], the intrinsic portion of the transverse piezoelectric coefficient can be attributed to the dielectric, ferroelectric and electrostrictive properties of the material. For PZT, coefficients for the tetragonal and rhombohedral phases are given by equations 1.11 and 1.12 respectively,

$$d_{31} = 2\varepsilon_o \varepsilon_{33} Q_{12} P_3 \tag{1.11}$$

$$d_{31} = 2\varepsilon_o [\varepsilon_{11} Q_{12} + \varepsilon_{12} (Q_{11} + Q_{12})] P_3 \tag{1.12}$$

where Q is the electrostricitve coefficient and P_3 is the spontaneous polarization.

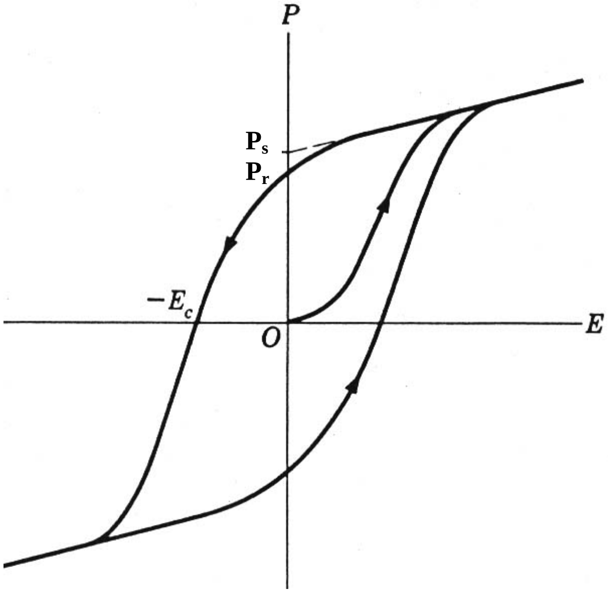

Figure 1.9 Characteristic polarization – electric field hysteresis loop of ferroelectric materials. Source: [34]

1.3.2 Lead Zirconate Titanate

Due to the strong piezoelectric behavior of lead zirconate titanate, discovered by B. Jaffe in the 1955, it has become the most widely employed piezoelectric material - replacing barium titanate for almost all applications.[37]

Structure & properties PZT is a solid solution between lead zirconate ($PbZrO_3$) and lead titanate ($PbTiO_3$) and like barium titanate possesses the perovskite (ABO_3) crystal structure. The phase diagram for the PZT material system is given in figure 1.10.[38] Above the Curie temperature, the material is paraelectric or non-ferroelectric at all material compositions. At lower temperatures, a transition occurs to either the tetragonal or rhombohedral ferroelectric phases. A monoclinic phase between these two phases was recently discovered.[39] Depicted in figure 1.11 is the prototypic cubic form of PZT, with the lead cations located at the corners of the unit cell, the zirconium or titanium occupying the center, and oxygen at the vertices of an octahedron surrounding the center anion. At temperatures below the Curie point, T_c, small displacements of the ions result in a separation of the positive and negative charge creating an electric dipole, which is accompanied by an elongation of the unit cell along the polarization direction. In the tetragonal phase, the polar axis is along one of the 6 <001> directions, and along one of

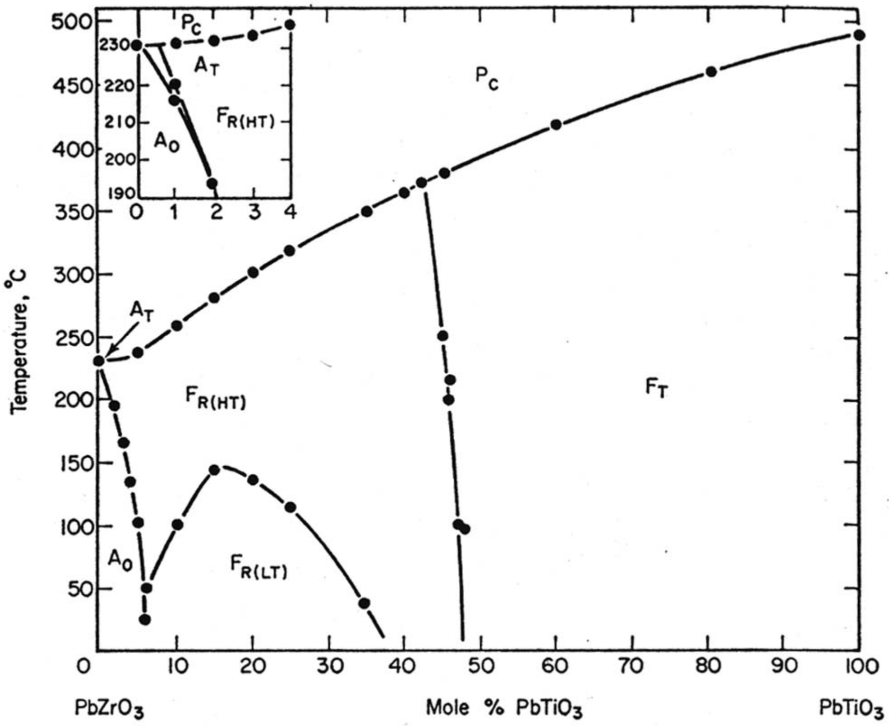

Paraelectric Phase
P_c Cubic

Ferroelectric Phases
F_T Tetragonal
F_R Rhombohedral
$F_{R(HT)}$ High Temp.
$F_{R(LT)}$ Low Temp.

Antiferroelectric Phases
A_o Orthorombic
A_T Tetragonal

Figure 1.10 Phase diagram for lead zirconate titanate $Pb(Zr_{1-x}Ti_x)O_3$.[37]

the 8 <111> directions in the rombohedral phase. Application of an electric field can reorient the spontaneous polarization along any of the equivalent directions. Above the Curie temperature, the spontaneous polarization and P-E hysteresis disappear, and the material becomes paraelectric.

The compositional dependence of the piezoelectric and dielectric properties of both bulk and film PZT have been studied. A peak in permittivity and the piezoelectric coefficients was observed for bulk ceramics at a Zr/Ti ratio of 52/48 along the morphotropic phase boundary (MPB).[38] Work by Chen and Xu confirmed this relationship for PZT films.[40]

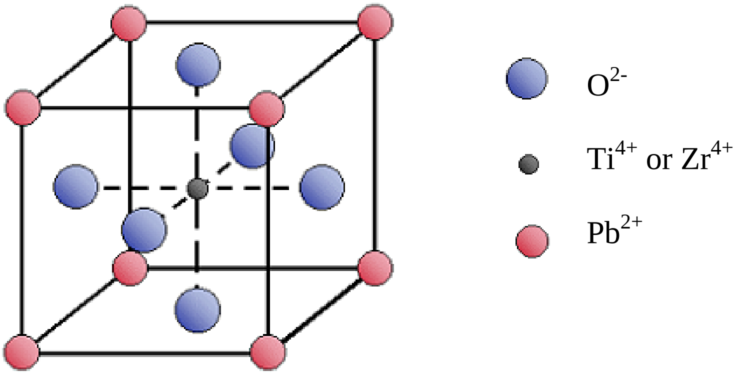

Figure 1.11 Prototype form of the cubic perovskite structure of PZT.

Piezoelectricity and actuation modes in PZT The physical origins of the piezoelectric effect are categorized as intrinsic or extrinsic. The deformation of the unit cell in response to an applied field is known as the intrinsic component, and is responsible for the strain of the individual domains. Most of the extrinsic contribution can be attributed to non-180° domain wall motion. For bulk PZT ceramics, the extrinsic effect comprises 60% –70% of the measured piezoelectric response at room temperature.[41]

Based on symmetry arguments, the piezoelectric matrix for a poled PZT sample can be simplified to,

$$d_{ij} = \begin{pmatrix} 0 & 0 & 0 & 0 & d_{15} & 0 \\ 0 & 0 & 0 & d_{15} & 0 & 0 \\ d_{31} & d_{31} & d_{33} & 0 & 0 & 0 \end{pmatrix} \tag{1.13}$$

All but five of the coefficients are zero, and only three are unique. This implies that three modes of operation exist; these are illustrated in figure 1.12. The dashed line represents the resulting strain (much exaggerated). The first shown is the $d_{33,}$ or longitudinal mode. The electric field is applied in the direction of the polarization and the resulting strain in the same direction is utilized. This however, also induces a lesser strain in the transverse direction – the d_{31} mode. An electric field applied perpendicular to the polarization, causes a shear strain, and is known as the d_{15} mode. For bulk PZT(52/48), the piezoelectric coefficients are: d_{33} = 330 - 675 pm/V, d_{31} = -165 to --310 pm/V, and d_{15} = 850 - 920 pm/V.[42] The negative value of d_{31} indicates that the material contracts in this direction. To generate a positive strain, the electric field is applied opposite the polarization.

1.3.3 PZT films

Deposition Ferroelectric thin films have been deposited by a variety of techniques that can be classified as based on either the vapor or liquid phase. Included as vapor-phase methods are sputtering,[43] pulsed laser deposition (PLD),[44] metal-organic chemical-vapor (MOCVD), and molecular-beam epitaxy (MBE). In chemical solution deposition, such as metal-organic decomposition (MOD) and sol-gel methods,[45] the precursors are dissolved in a liquid solvent. This solution is then applied to the substrate by spinning, misting, spraying or dip coating. Control of stoichiometry is more difficult with multi-cation systems such as PZT, and is an important factor affecting the choice of deposition technique.[46] Other determining factors include coverage uniformity, temperature requirements, step-coverage, compatibility with other processing, deposition rate, and maximum thickness. Ion bombardment during sputtering can result in high stress levels in PZT films. Controlling these residual stresses is of paramount importance in free-standing MEMS structures. Sol-gel and spin coating were chosen as the deposition method for this study because it produces good quality films with relatively low residual stresses. Other advantages include easy composition control, large area coverage, thicknesses up to 10 μm, and comparably lower equipment cost.

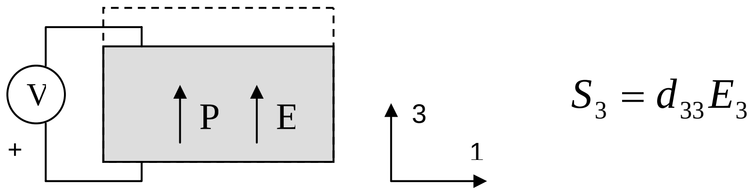

(a) d_{33} or longitudinal mode

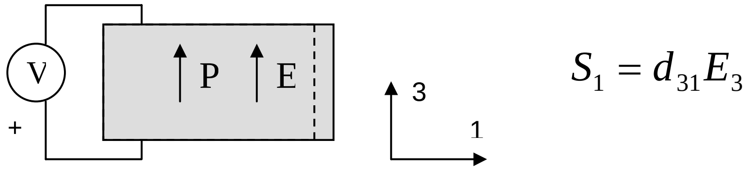

(b) d_{31} or transverse mode

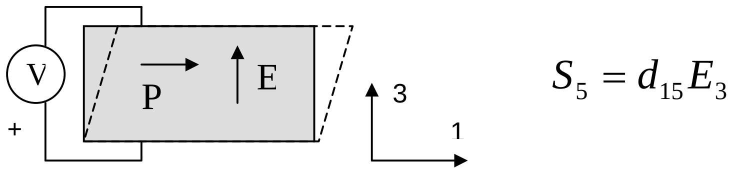

(c) d_{15} or shear mode

Figure 1.12 Actuation modes for piezoelectric lead zirconate titante (a) longitudinal, (b) transverse and (c) shear. S = Strain, E = Electric field, P = Polarization, d = piezoelectric coefficient, V = voltage.

Substrates and electrodes Single crystal silicon wafers, as used by the semiconductor industry, have been the most widely used substrates for MEMS and PZT MEMS. Since MEMS evolved from the IC industry, there is an extensive technology base and a historical tendency to use silicon. Integration with microelectronics is also a key reason. Silicon also has excellent mechanical properties and does not fatigue easily, making it a good choice for moving structures.[47] The deposition of PZT on silicon substrates however, presents a problem. Lead oxide reacts with silicon at temperatures lower than those required to fully crystallize the ferroelectric phase in PZT (> 500°C). The depletion of lead from the PZT degrades the electrical properties, and for this reason, a barrier layer is required. The barrier layer must prevent diffusion, and must not react with the PZT or the substrate. The bottom electrode, such as platinum can serve this purpose. Since Pt also reacts with silicon, a stack based on Pt/Ti/SiO_2/Si, is commonly utilized, with the thin Ti acting as an adhesion layer.[48] Other barrier layers include conducting RuO_2,[49] nonconducting ZrO_2,[50] and $LaNiO_3$. The choice of electrode and substrate, like the deposition method and conditions, can influence the properties of the film.[51] Xu controlled the texturing of sol-gel deposited PZT films by depositing on <111> and <100> oriented platinum.[52] For several compositions near the MPB, he observed that the effective piezoelectric constant was slightly larger for <111> oriented films.

Piezoelectric properties In general, the properties of thin films are often different from those of bulk samples. Measurements have shown that both the longitudinal and transverse piezoelectric coefficients of PZT films are significantly lower than those of the bulk material. Typical values for PZT films were given in table 1.3. The smaller piezoelectric response can be partially attributed to substrate clamping through two distinct mechanisms. Since the substrate is typically much thicker than the film, the in-plane strain of the film is restricted. Measurement of the strain normal to the substrate, leads to the calculation of an effective coefficient, $d_{33f.}$ If the plane strain and normal stress are zero, the effective longitudinal piezo-coefficient is related to the real coefficient by,[53]

$$d_{33f} = d_{33} - \frac{2d_{31}s_{13}^E}{(s_{11}^E + s_{12}^E)} \qquad (1.14)$$

where, s_{xy}, is the compliance of the film measured under constant field. The equation indicates that the effective coefficient is always smaller. The influence of effective parameters on the design of devices is discussed in more detail in chapter two. The clamping effect has also been suggested to affect the strain response directly. Xu found that in fine grained (50-100nm) thin (<2 μm) PZT films that the extrinsic contribution to the piezoelectric response was small, and that the pinning of non-180° domain walls is likely the cause.

1.3.4 PZT MEMS

PZT based MEMS Due to the superior piezoelectric properties of PZT over other piezoelectric films, there has been a steady and increasing effort toward the integration of this material with MEMS. PZT films deposited by several techniques have been successfully used in a variety of MEMS devices. Typically, the film is deposited on a membrane or beam, and released by bulk etching the substrate or removing a sacrificial layer. Although most devices are similar in design and exploit the d_{31} mode, the range of applications is quite wide. Acoustic transducers used for monitoring the integrity of structures and acoustic imaging have been demonstrated.[54] Along with pressure sensors, accelerometers are one of the most mature MEMS devices. Wang developed a PZT micromachined accelerometer based on cantilevers, trampolines and circular diaphragms.[55,56] A bridge-type sensor that enclosed a sealed cavity was fabricated, and was responsive to acoustic and temperature changes.[57] Peristaltic micropumps were demonstrated for dispensing small quantities of liquids for biochemical analysis. More recently, similar pumps were investigated for pumping gases for micromachined mass spectrometers.[58] A bridge-type (clamped-clamped beam) resonant structure was used as a resonator for filtering electrical signals.[59] Thin PZT films were also used as vibrators to drive micro-motors.[60]

PZT cantilever microactuators Micromachined unimorph cantilever transducers have been demonstrated by several groups for various applications, but all were designed to operate in the transverse mode. Polla's group conducted some of the early work in PZT MEMS and demonstrated a surface micromachined cantilever released by etching a silicon oxide sacrificial layer.[61] Brooks instead used KOH to bulk etch the silicon substrate and measured the resonance frequency and coupling factor of the cantilevers.[62] Two groups out of Japan fabricated PZT unimorph cantilevers by bulk substrate etching for use as the styli in atomic force microscopy.[63, 64] The PZT was sputtered and sol-gel deposited. A German group has fabricated similar cantilever actuators with the ultimate goal of realizing a PZT based miroswitch.[65] Their design consists of sol-gel deposited PZT on a platinum coated polysilicon passive layer. The device is released by bulk etching in TMAH. Researchers from Marconi Caswell Ltd reported the successful fabrication of a sol-gel-deposited PZT based micromachined RF switch.[17] The switch is based on a transverse mode unimorph cantilever actuator that is released by a combination of bulk silicon etching and deep reactive-ion etching. To contact the transmission lines, the actuator was flip-chip bonded onto a GaAs substrate likely to be integrated with high speed microelectronics.

1.4 Research objectives

Electrostatic MEMS switches have demonstrated, in key areas, superior performance over existing RF switches, and have therefore established a niche among the other technologies. The advantages over semiconductor based devices include: low loss and good isolation at high frequencies (>1GHz), near-zero power consumption, and linear operation. Existing drawbacks are low switching speeds (>2 μs), high actuation voltages (>30V), and low signal power (<1W). Based on the characteristics of realized PZT actuators and modeling, an improvement over electrostatic switches is expected by utilizing piezoelectric actuation. The required force and deflection for reliable operation can be generated with a significantly reduce voltage. This is an advantage in many systems. An analytical comparison showed that a cantilever-type switch required 25 volts when actuated by electrostatics, but only 2.4 volts by using PZT – more than an order of magnitude difference.[66] Alternativly, PZT can be exploited to design a device with a faster switching speed. Stiction between contacts and transmission lines is one of the failure modes for electrostatic switches. Since the piezoelectric effect is bipolar, a PZT switch can be made to switch-off and overcome stiction related problems. Additionally, due to the instability in electrostatic actuation, the impact force of the contact cannot be controlled easily. With piezoelectric actuation, this contact force can be controlled and the composition of the contact material can be tailored specifically, yielding improved reliability. However, the advantages of piezoelectric actuation and PZT specifically, are realized through greater fabrication complexity as will be explained in the subsequent chapters.

The objectives of this research were:

1) Design of a piezoelectric, PZT based, MEMS RF switch with high speed switching.
2) Development of an actuator microfabrication process
3) Development of a switch microfabrication process
4) The fabrication of devices and the successful demonstration of concept
5) Measurement of the operating characteristics of the devices:
    a. Switching characteristics
    b. Characteristics of microactuators

References

---

[1] C. T.-C. Nguyen, " Communications applications of microelectrocmechanical systems," Proc. Sensors Expo., May 19-21, pp.447, 1998.

[2] G. Rebeiz, J. Muldavin," RF MEMS switches and switch circuits," IEEE Microwave Mag. 2, pp. 59, 2001.

[3] E. Brown, "RF-MEMS switches for reconfigurable integrated circuits," IEEE Trans. on Microwave Theory and Techniques, 46, 1998.

[4] K.E. Petersen, "Micromechanical membrane switches on silicon," IBM J. Res. Develop. 23**,** 376 (1979)

[5] R. N. Thomas, J. Guldberg, H.C. Nathanson, P.R. Malmberg, "The mirror matrix tube: A novel light valve for projection displays," IEEE Trans. Electron Devices, 22, pp. 765, 1975

[6] E. Bassous, H.H Taub, L. Kuhn, "Ink jet printing nozzle arrays etched in silicon," Appl. Phys. Lett. 31, pp. 135, 1977.

[7] S.Sugiyama, T. Suzuki, K. Kawahata, K. Shimaoka, M. Takigawa, I. Igarashi, "Micro-diaphragm sensor," IEDM, pp. 184, 1986.

[8] P.D. Grant, R.R. Mansour, M.W. Denhoff, "A comparison between RF MEMS switches and semiconductor switches," Can. J. Electrical and Computer Engineering, (27)1, 2002.

[9] G.M. Rebeiz, *RF MEMS Theory, Design, and Technology*, John Wiley & Sons, 2003.

[10] S-Parameter Design, Application Note 154, Hewlett Packard, 1990

---

[11] Dow-Key Microwave Corporation, “Types of microwave switches,” Design guide Section II.

[12] Alpha Industries Inc.,” Design with PIN diodes,” application note APN1002.

[13] J. J. Yao, “RF MEMS from a device perspective,” J. of Micromechanics and Microengineering 10, pp. R9, 2000.

[14] Z. Jamie Yao, S. Chen, S. Eshelman, D. Denniston, C.L Goldsmith, “Micomachined low-loss microwave switches,” IEEE J. of Microelectromechanical systems, 8(2), 1999.

[15] M. Ruan, J. Shen, C.B. Wheeler, “Latching magnetic relays with multistrip permalloy cantilevers,” 14th IEEE Intl. Conf. on Micro Electro Mechanical Systems, 224, 2001.

[16] P. Blondy, D. Mercier, D.Cros, P. Guillon, P. Rey, P. Charvet, B. Diem, “Packaged millimeter wave thermal MEMS switches,” Proc. Gallium Arsenide applications symposium, 2001.

[17] C.M. Beck, M.M Ahmed, C.J. Brierley, A.P. Needham, S.P. Marsh, “Microwave filters and switches produced using micro-machining techniques,” IEEE Intr. Microwave Symposium, 2000.

[18] N.E. McGruer, P.M. Zavracky, R. Morrison, S. Majumder, D. Potter, M. Schirmer, “RF and current handling performance of electrostatically actuated microswitches,” Sensors Exposition, Cleavland, OH, September, 1999.

[19] W.S.N. Trimmer, “Microbots and Micromechanical systems,” Sensors and Actuators A, 19, pp. 267, 1989.

---

[20] F.C.M van de Pol, H.T.G van Lintel, M. Elvenspoek, J.H.J. Fluitman, "Thermopneumatic micropump based on micro-engineering techniques," Sensors and Actuators A, 21, pp.198, 1990.

[21] M. Madou, *Fundamentals of Microfabrication*, CRC press, 1997.

[22] J.F Nye, *Physical Properties of Crystals*, Oxford Science Publishing, 1985.

[23] K. Uchino, *Ferroelectric Devices*, Marcel Dekker, 2000.

[24] IEEE Standard, *IEEE Standard on Piezoelectricity*, IEEE, 2001.

[25] D.L.DeVoe, A.P.Pisano, " Surface micromachined piezoelectric accelerometers (PiXLs),"J. Microelectromechanical Systems, 10(2), 2001.

[26] R.S. Muller, "From IC's to microstructures: materials and technologies," Proc. IEEE Micro Robots and Teleoperators Workshop, Hyannis, MA, 1987.

[27] M.J. Vellekoop, C.C.G. Visser, P.M. Sarro, A. Venema, "Compatability of zinc oxided with silicon IC processing," Sensors and Actuators A, 23, pp. 1027, 1990.

[28] Q.M. Zhang, Feng Xia, Z.-Y. Cheng, H. Xu, H. Li, M. Poh, C. Huang, "Poly(vinylidene fluoroethylene-trifluoroethylene) based high performance electroactive polymers," 11th Inter. Symp. on Electrets, 2002.

[29] W. Tjhen, T.Tamagawa, C.-P. Ye, C.-C Hsueh, P.Shiller, D. L. Polla, "Properties of piezoelectric thin films for micromechanical devices and systems," Proc. IEEE Micro Electro Mechanical Systems (MEMS'91), Japan, pp.114, 1991.

[30] C.M. Lueng, H.L. Chan, C. Surya, C.L. Choy, "Piezoelectric coefficient of aluminum nitride and gallium nitride," J. Appl. Phys. 88(9), pp. 5360, 2000.

---

[31] R. Wolf, "Temperature dependance of the piezoelectric response of lead zirconate titantate films for MEMS applications," Master's thesis, The Pennsylvania State University, 2001.

[32] S. Trolier-McKinstry,"Piezoelectric films for MEMS applications," J. Ceramic Society of Japan, 109(5), 2001.

[33] M. Zahn, Electromagnetic field theory a problem solving approach, Krieger Publishing Company, 1979.

[34] Michael Foeth, "Determination of the Thermal Broadening of Ferroelectric Domain Walls using Quantitative Transmission Electron Microscopy," Doctorate thesis, No. 2022, Dept. Phys., Ecole Polytechnique Federal de Lausanne, 1999.

[35] F. Jona, G. Shirane, *Ferroelectric Crystals*, Pergamon Press NY, 1962.

[36] M.J. Haun, "Thermodynamic Theory of the Lead Zirconate Titanate Solid Solution System," Ph.D. Thesis, The Pennsylvania State University, 1988.

[37] S. Fujishima, "History of ceramic filters," IEEE Trans. UFFC, 47(1), 2000.

[38] B. Jaffe, W.R.Cook, H. Jaffe, *Piezoelectric Ceramics*, Academic Press NY, 1971.

[39] B. Noheda, J.A. Gonzalo, L.E. Cross, R. Guo, S.-E. Park, D.E. Cox, G. Shirane, "Tetragonal-to-monoclinic phase transition in a ferroelectric perovskite: The structure of $PbZr_{0.52}Ti_{0.48}O_3$," Phys. Rev. B, 61(13), pp. 8687, 2000.

[40] H.D. Chen, K.R. Udayakumar, C.J. Gaskey, L.E. Cross, "Electrical properties' maxima in thin films of the lead zirconate-lead titanate solid solution system," Appl. Phys. Lett., 67(23), pp.3411, 1995.

---

[41] A.G. Luchaninov, A.V. Shil’Nikov, L.A. Shuvalov, Shikova, “The domain processes and piezoeffect in polycrystalline ferroelectrics,” Ferroelectrics, 98 (123), 1989.

[42] TRS Ceramics, Dielectric and piezoelectric properties of soft piezoelectrics, www.trsceramics.com

[43] S. Kalpat and K. Uchino, "Highly Oriented Lead Zirconate Titanate Thin Films: Growth, Control of Texture, and Its Effect on Dielectric Properties," J. Appl. Phys., 90 (6), 2703-2710 (2001).

[44] T. Yoshimura, S. Trolier-McKinstry, “Growth and piezoelectric properties of $Pb(Yb_{½}Nb_{½})O_3$-$PbTiO_3$ epitaxial films,” J. Appl. Phys., 92(7), pp. 3979, 2002.

[45] K.D. Budd, S.K. Dey, D.A. Payne, “Sol-gel processing of $PbTiO_3$, $PbZrO_3$, PZT, and PLZT thin films,” Brit. Ceram. Proc., 36, pp.107, 1985.

[46] L.E Cross, S. Trolier-McKinstry, “Thin-Film Integrated Ferroelectrics,” Encl. Appl. Phys. 21, pp. 429, 1997.

[47] K.E. Petersen, “Silicon as a mechanical material,” Proc. of IEEE, 70(5), pp.420, 1982.

[48] G.R. Fox, S. Trolier-McKinstry, S.B. Krupanidhi, L.M. Casas, “Pt/Ti/SiO_2/Si substrates,” J. Mat. Res., 10(6), 1995.

[49] T. Maeder, P. Muralt, L. Sagalowicz, N. Setter, “Conducting barriers for direct contact of PZT thin films on reactive substrates,” J. Electrochemical Soc., 146(9), 199.

[50] B. Xu, Y. Ye, L.E.Cross, J.J. Bernstein, R.Miller, “Dielectric and hysteresis from transverse electric fields in lead zirconate titanate thin films,” App. Phy. Lett., 74, pp. 3549, 1999.

---

[51] D. Polla, L. Francis, “Processing and characterization of piezoelectric materials and integration into micromechanical systems,” Annual Review of Materials Science 28, pp.563 1998.

[52] F. Xu, F. Chu, S. Trolier-McKinstry, “Domain wall motion and its contribution to the dielectric and piezoelectric properties of lead zirconate titanate films,” J. App. Phy., 89(2), 2001.

[53] K. Lefki, G.J.M. Dormans, “Measurement of piezoelectric coefficients of ferroelectric thin films,” J. Appl. Phys 76(3), pp. 1764, 1994.

[54] J.J. Bernstein, S.L. Finberg, K. Houston, L.C. Niles, H.D. Chen, L. E. Cross, K.K. Li, K. Udayakumar, “ Micromachined high frequency ferroelectric sonar transducer,” IEEE Trans. on UFFC, 44(5), 1997.

[55] L.-P.Wang, “Microelectromechanical systems (MEMS) sensors based on lead zirconate titanate (PZT) films,” Ph.D. Thesis, The Pennsylvania State University, 2001.

[56] Han Geun Yu, L. Zou, K. Deng, R. Wolf, S. Tadigadapa, S. Trolier-McKinstry, “Lead zirconate titanate MEMS accelerometer using interdigitated electrodes,” Sensors and Actuators A: Physical, 107(1), pp. 26-35, 2003.

[57] T. Tamagawa, D.L. Polla, “Lead Zirconate Titanate (PZT) thin films in surface micromachined sensor structures,” IEEE Int. Electron Devices Meeting, San Francisco, 1990.

[58] E. Hong, Surface micromachined peristaltic pumps using lead zirconate titanate film, Ph.D. thesis, The Pennsylvania State University, 2004.

---

[59] B. Piekarski, D. DeVoe, M. Dubey, R. Kaul, J. Conrad, R. Zeto, "Surface micromachined piezoelectric resonant beam filters," Sensors and Actuators A, 90(3), pp. 313, 2001.

[60] P. Muralt, M. Kohli, T. Maeder, A. Kolkin, K. Brooks, N. Setter, R. Luthier, "Fabrication and characterization of PZT thin-film vibraotors for micromotors," Sensors and Actuators A, pp. 157, 1995.

[61] J. H. Kim, L. Wang, S. M. Zurn, L. Li, Y. Yoon, D. L. Polla, "Fabrication process of PZT piezoelectric cantilever unimorphs using micromaching," Integrated Ferroelectrics, 15, pp. 325, 1997.

[62] K.G. Brooks, D. Damjanovic, N. Setter," Piezoelectric resonponse of PZT thin film actuated micromachined silicon cantilever beams," IEEE Inter. Symp. Appl. of Ferroelectrics, pp.520, 1994

[63] T. Fujii, S. Watanabe, " Feedback positioning cantilever using lead zirconate titanate thin film for force microscopy observation of micropattern," Appl. Phys. Lett. 68(4), 1996.

[64] C. Lee, T. Itoh, T. Suga, "Self-excited piezoelectric PZT microcantilevers for dynamic SFM – with inherent sensing and actuating capabilities," Sensors and Actuators A, 72, 1999.

[65] H. Kueppers, T. Leuerer, U. Schnakenberg, W. Mokwa, M. Hoffmann, T. Schneller, U. Boettger, R. Waser, " PZT films for piezoelectric microactuator applications," Sensors and Actuators A, 97-98, 2002.

[66] G. Klaasse, R. Puers, H.A.C. Tilmans, "Piezoelectric versus electrostatic actuation for a capacitive RF-MEMS switch," Proc. SeSens, Veldhoven, The Netherlands, November 29, 2002.

Chapter 2

Device Analysis & Design

This chapter discusses the design of the microactuators and microswitches. Cantilevered bender actuators were used to increase the piezoelectrically-induced deflection. Surface micromachining by etching a sacrificial layer was selected as a process to fabricate the actuators. The layout of the transmission lines and contacts is presented to complete the switch design. Finally, an analysis of the performance of the actuators was performed to determine the optimum design parameters.

2.1 Switch & microactuator design

2.1.1 Bender actuators

Despite the comparatively high piezoelectric coefficient of PZT, the actual magnitude of the strain is quite small, typically 0.1%. Although the resulting displacement is too small for many applications, the elastic modulus (70 –100 GPa) and the forces generated are quite large. Many applications, therefore, employ structures that amplify the displacement at the expense of the force. The most common of these are bender actuators, which include unimorphs, bimorphs, and multimorphs. Due to the direct effect, piezoelectric bender transducers are used as sensors as well as actuators, and are used in many diverse applications and devices such as gyroscopes, accelerometers, phonographs, position control, and acoustics.[1] The piezoelectric bimorph dates back to 1931.[2]

The unimorph, also known as a heterogeneous bimorph or monomorph, structure is quite simple and is shown in figure 2.1a in a cantilevered support configuration. The unimorph is composed of a piezoelectric material bonded to a passive, non-piezoelectric and mechanically elastic material. Application of an electric field to the piezoelectric induces the generation of stress and strain. The passive material resists the strain, resulting in an internal moment and the bending of the structure. Upon removal of the field, the elastic restoring forces cause a return to the original curvature. A bimorph structure, shown in figure 2.1b, is made up of two piezoelectric layers separated by a thin electrode. In this case, the field-induced strain is present in both layers. Several configurations are possible for both the unimorph and bimorph based on the direction of polarization and applied field. For the d_{31} mode, both the poling and applied electric field point in the thickness direction, while the lateral or transverse stress and strain are exploited. The d_{31} coefficient is therefore used.

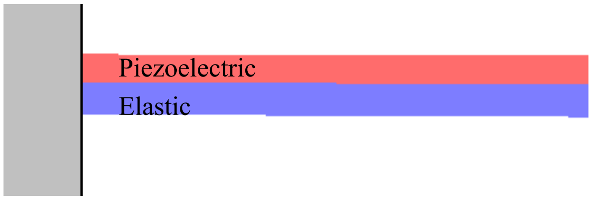

(a) Unimorph

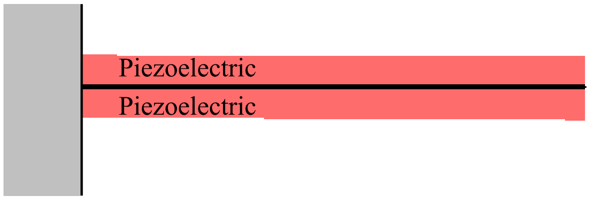

(b) Bimorph

Figure 2.1 Unimorph (a) and bimorph (b) cantilevered bender actuators.

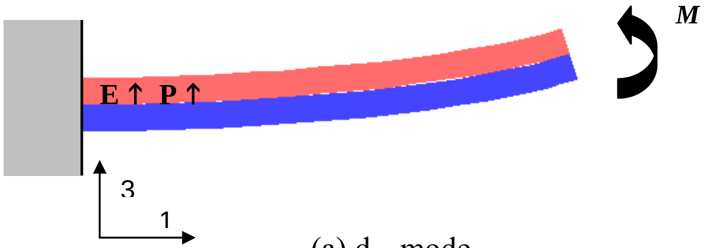

(a) d_{31} mode

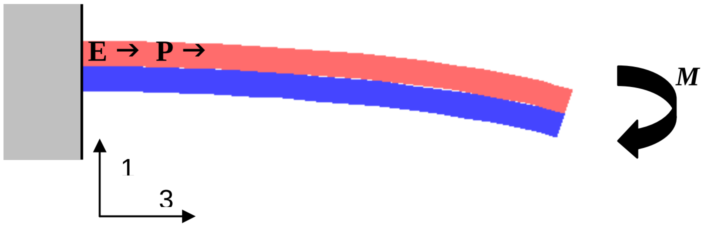

(b) d_{33} mode

Figure 2.2 Two modes of operation for unimorphs actuators showing the direction of **P**olarization and **E**lectric field in the structures. (a) transverse or d_{31} mode. (b) longitudinal or d_{33} mode.

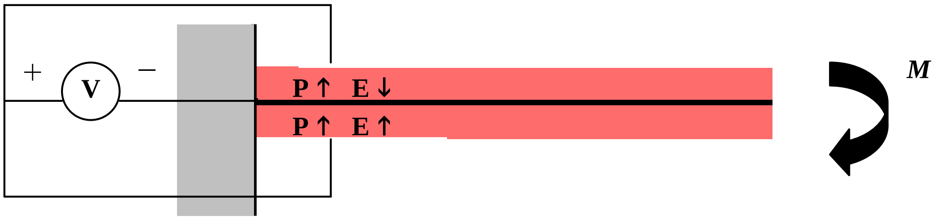

(a) Parallel

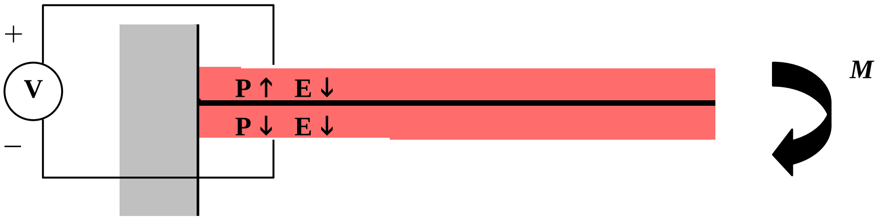

(b) Series

Figure 2.3 Electrical configurations of d_{31} bimorph actuators showing resulting moment. (a) Parallel (b) Outward series.

Alternatively, for the d_{33} mode, the polarization, field and exploited strain and stress lie in the longitudinal direction. Figure 2.2 illustrates these two modes for a unimorph actuator. Figure 2.3 shows two electrical configurations, including the polarization direction and resulting bending moment for a d_{31} mode bimorph actuator. At a given voltage, the field generated across the piezoelectric in the parallel connection is twice greater than in the series type. As a consequence, the tip deflection and force are twice greater. As shown in the figure, both actuators produce a downward deflection. A d_{33} mode bimorph is not discussed.

2.1.2 MEMS bender actuators

The fabrication of MEMS actuators and sensors typically involves three basic steps. The first is the deposition of thin or thick films upon a substrate. The second step is the etching of some or all of the films to delineate the device geometry. Steps one and two may be repeated depending on the fabrication sequence. Lastly, a sacrificial layer is removed to make the structures freestanding. The sacrificial layer can be a deposited film as in surface micromachining, or the substrate itself as in bulk micromachining. Piezoelectric cantilevers, based on PZT and ZnO, have been reported using both approaches.[3] Surface micromachining was used in this work. Following common designs, silicon oxide was chosen as the sacrificial layer.[4] It was quickly discovered that the PZT, although protected, was easily damaged by the hydrofluoric acid used to remove the oxide. The wet nature of the release etch also resulted in stiction related losses. Therefore, the release process was changed to a dry etch, and the sacrificial layer was changed to polysilicon. Although not the best choice from an RF perspective, oxidized silicon wafers were chosen as the substrate since most of the available data from the literature was based on silicon.

2.1.3 Transverse mode microactuators

Unimorph cantilever microactuators were selected initially for the switch design for two reasons. First, PZT unimorphs had been demonstrated successfully, and secondly, it was believed that for reliable operation, a mechanically robust and stiff passive layer was necessary. Due to its properties, silicon nitride deposited by low pressure chemical vapor deposition (LPCVD) was chosen. It was understood from the beginning that a large difference in the residual stresses in the PZT and nitride would result in an unwanted curvature of the cantilevers upon release. From the literature, the residual stress of sol-gel deposited PZT on silicon substrates, was thought to be about 100 MPa.[5] Stoichiometric LPCVD silicon nitride exhibits a residual stress of 600 to 800 MPa.[6] To more closely match the value of PZT, Si-rich low-stress nitride (100 – 400 MPa) was chosen.[7] Rather than developing the process to deposit the films in-house, the service was provided by Cornell and Berkeley Universities. A known hurdle in the integration of PZT films with mainstream commercial microfabrication is the CMOS compatibility of the elemental constituents.[4] Since lead is forbidden from the dedicated furnace tubes used to deposit the silicon nitride, the PZT layer was deposited last. This forced the active layer in the structure to lie above the passive layer.

For parallel plate electrodes, as in the case of d_{31} mode devices, the capacitance, C, can be calculated by equation 2.1.

$$C = \frac{A\varepsilon_0\varepsilon_r}{t} \tag{2.1}$$

A is the electrode area, t is the distance between the electrodes which is the PZT thickness, and ε_r and ε_o are the relative and vacuum permittivities. The area is also used in the measurement of the induced polarization.

Since the platinum/titanium bottom electrode is the most common and well characterized, it was chosen for the design of the d_{31} mode unimorphs. These devices were fabricated and demonstrate the microactuator concept. Designing microswitches required the addition of transmission lines and a contact at the end of the cantilever. The downward deflection of the d_{31} type devices is limited to a maximum applied electric field of E_c. This is not the case for the d_{33} mode as the field is applied in the same direction as the polarization. This suggested that the transmission lines be positioned above the cantilever in the d_{31} mode and below the cantilever for the d_{33} mode. It was believed that bottom transmission lines would require fewer steps and therefore be less complex from a fabrication point of view. In addition, the d_{33} coefficient of PZT film is usually two times larger than the d_{31} coefficient, meaning that for the same electric field, the piezoelectric strain is expected to be two times larger.[8] For these reasons, d_{33} mode unimorph cantilevers were chosen for the switch design.

2.1.4 Longitudinal mode microactuators

Exploiting the longitudinal piezoelectric strain requires that the PZT be poled along the length of the cantilever, and that the electric field be applied in the same direction. Interdigitated electrodes (IDE) on top of PZT, such as those used in SAW devices, were used to accomplish both. Instead of the bottom platinum electrode, the new actuation mode required that the PZT be deposited on an electrically insulating buffer layer. The buffer, or barrier, layer must not react chemically with the PZT or nitride, and must also prevent diffusion between the two. Sol-gel deposited zirconium oxide was reported to act as an effective barrier layer for this purpose. It has been suggested that a minimum thickness and/or density is required to prevent Pb diffusion and the formation of the pyrochlore phase in PZT.[9] Results have shown that 300 nm of sol-gel zirconia annealed at 700° C is adequate for PZT deposited on silicon rich nitride.

Shown in figure 2.4, is a top and cross-sectional view of the IDE, along with a model used for the analysis. Based on the model, the capacitance of the configuration is given by,

$$C = \frac{t_{PZT} l \varepsilon}{d}(n-1) \tag{2.2}$$

As denoted in the figure, t_{PZT} is the thickness of the PZT, l is the distance between the rails (180μm), d is the distance between fingers (6μm), ε is the permittivity, and n is the number of fingers. Several assumptions are made in the use of equation 2.2. The electric field beneath the electrodes is small compared to the region between the electrodes, and so is considered to be zero. The field in the PZT between the electrodes is uniform, and is equal to the voltage divided by d. Using numerical modeling these assumptions were validated.[9] Since the dielectric constant of the silicon nitride (6) and zirconia (20) are

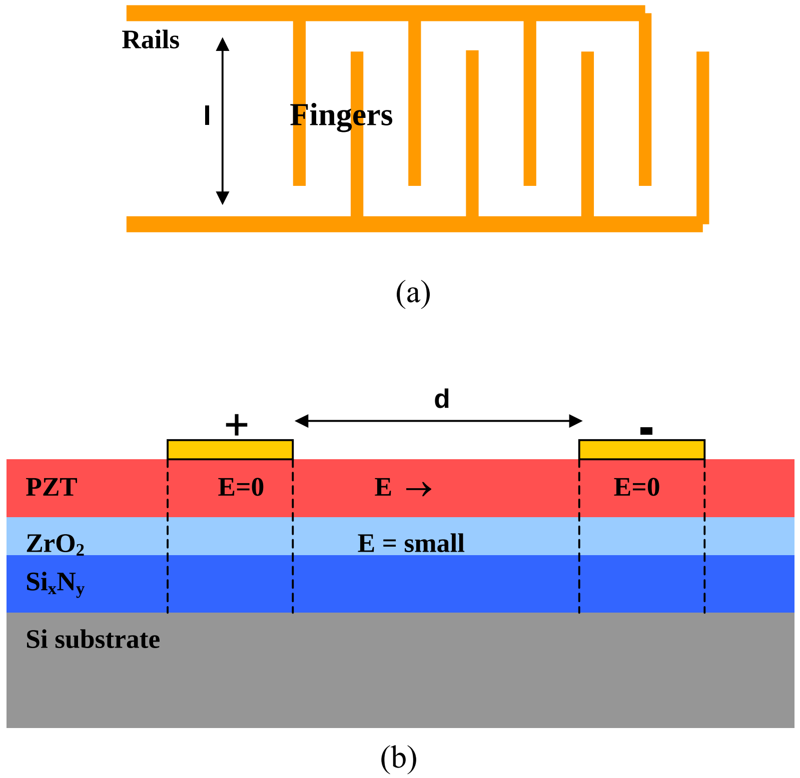

Figure 2.4 The d_{33} actuation mode (a) Top view of interdigitated electrodes (IDE) with rails and fingers and (b) model used in analysis.

small compared to PZT (900), the contribution of these films to the total capacitance is small, and is therefore neglected. This is also a valid approximation because the electric field is weaker further from the electrodes. Since the field is negligible below the electrodes, this volume does not contribute to the overall strain and deflection of the actuator. For this reason, the finger width should be made as small as possible. The design width was 3 µm, but the actual width of the IDE fingers depends slightly on the fabrication process.

2.1.5 Transmission lines and contacts

The final design of the d_{33} mode unimorph switch is presented in figure 2.5 with all the elements previously discussed. Gold was chosen as the metal for the transmission lines and due to its high conductivity, low contact resistance and its chemical inertness. Since

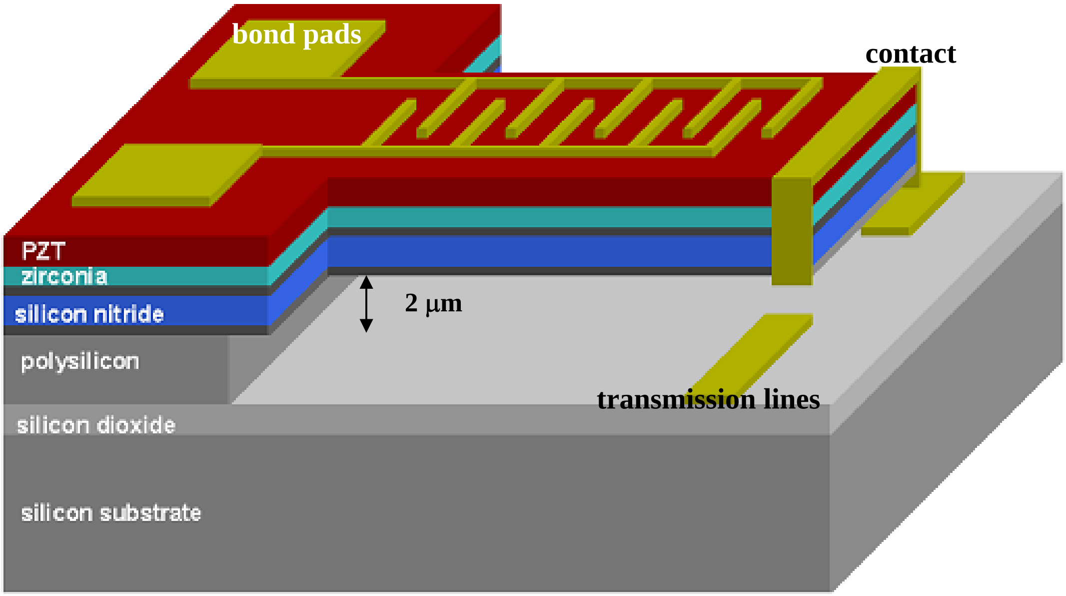

Figure 2.5 Longitudinal (d_{33}) mode unimorph actuator microswitch with interdigitated electrodes and dc transmission lines.

the transmission lines are located below the actuators, it is logical to deposit and pattern the transmission lines on the substrate beneath the sacrificial layer. This was not possible because, as is the case with PZT, gold is not compatible with CMOS processing since it forms midlevel traps in silicon, and is therefore forbidden from furnace tubes that are not specifically dedicated for MEMS. The metallization step to create the IDE and transmission lines was performed after the deposition and patterning of all the films. The contact was therefore deposited above the end of the cantilevers. Contact with the transmission lines is made by the gold on the cantilever edges.

2.2 Micro-actuator analysis

A quantitative analysis of the quasi-static tip deflection and blocking force as a function of applied field for bender actuators is provided in this section. As the derivation of the constituent equations is explained by several other sources, it is not repeated here.[10] The pertinent equations however, are presented and the implications on the design and performance of piezoelectric microswitches are discussed. The analysis is extended by including the influence of effective parameters in micro-scale actuators on the performance characteristics.

2.2.1 Actuation characteristics

The operational characteristics of bending actuators have been studied by numerous individuals including Steel [11] and extensively by Smits.[1] More recently, Weinburg[12] and DeVoe[3] focused on multilayer microbenders. The analysis presented herein is based on the work of Wang and is similar to that originally employed by Timoshenko for a thermal bimorph.[10,13] The quasi-static deflection and blocking force as a function of applied electric field, and the bending curvature due to internal stresses of a piezoelectric multilayer cantilevered bender actuator can be determined using beam theory.

Unlike a bimorph, the unimorph actuator has an asymmetric structure due to the difference in stiffness moduli and material thickness. This asymmetry causes a simultaneous axial extension and bending. The complete solution is a superposition of each case treated independently. Using this analysis, Wang obtained the quasi-static tip deflection δ as,

$$\delta = \frac{3L^2}{2t}\Delta \cdot S_L \qquad \Delta = \frac{2AB(1+B)^2}{AB + 2A(2B + 3B^2 + 2B^3) + 1} \tag{2.3}$$

where S_L is the piezoelectric-induced longitudinal strain, which depends on the mode of actuation, and L is the length of the cantilever. Δ is a dimensionless parameter with A, B, and C defined by equation 2.6, and S_L is given by equations 2.4 and 2.5.

$$S_L = S_1 = d_{31}E_3 \qquad \text{Transverse mode} \tag{2.4}$$

$$S_L = S_3 = d_3E_3 \qquad \text{Longitudinal mode} \tag{2.5}$$

$$A = \frac{Y_E}{Y_P} \quad B = \frac{t_E}{t_P} \quad C = \frac{\rho_E}{\rho_p} \tag{2.6}$$

where Y is the elastic modulus, t is the film thickness and ρ is the material density. The subscripts P and E denote the piezoelectric and elastic (passive) layers.

The blocking force, F_b, defined as the external force required at the tip to prevent deflection, and is given as,

$$F_b = \frac{3Wt^2Y_a}{8L}\Pi \cdot S_L \qquad \Pi = \frac{2AB}{(AB+1)(1+B)} \tag{2.7}$$

with Π as the dimensionless parameter. The effect of elastic stiffness and film thickness

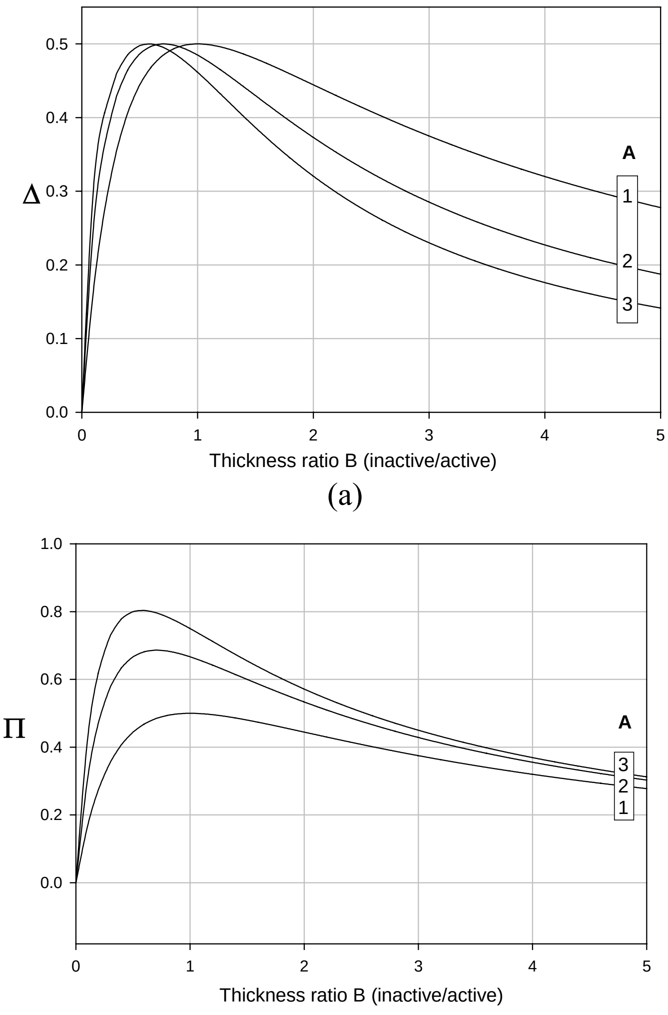

(a)

(b)

Figure 2.6 Deflection parameter delta (a), and force parameter pi (b) as a function of the ratio of the elastic modului (A) and of the thickness ratio (B).

on Π and Δ, and hence on deflection and blocking force is demonstrated in figure 2.6. The blocking force can be increased by increasing the stiffness ratio, A. The blocking force is important because it affects the contact resistance and hence the insertion loss of the switch. As is evident from equation 2.7, the force varies with the width of the actuator. The maximum deflection and blocking force both occur at a thickness ratio given by,

$$B = \sqrt{\frac{1}{A}} \tag{2.8}$$

This equation indicates the optimum thickness parameter. However, as is discussed in more detail in later chapters, the choice of parameters is affected by stress-compensation and fabrication issues.

The deflection and blocking force of a bimorph actuator are given by the same equations, 2.3 and 2.7, but Δ and Π are unity. The analysis for the bimorph neglects the mechanical influence of electrodes. As is readily observed from equation 2.3, the deflection of a unimorph is at most half that of a bimorph. The blocking force however depends on the elastic moduli, but for stiff passive materials can approach the value of a bimorph (ie A=3, Π=0.8).

As previously discussed, the electric field below the electrodes is small and therefore the piezoelectric material in that volume does not contribute significantly to the deflection. To account for the reduction in deflection and blocking force, a simple model is adopted. It was assumed that the material in the dead volume is rigid and does not detract from the piezoelectric strain. An IDE factor is introduced, given by,

$$IDEf = \frac{active \quad volume}{total \quad volume} \approx \frac{6\mu m}{3\mu m + 6\mu m} = 0.67 \tag{2.9}$$

The fringing field at the end of the fingers and the dead volume below the rails is not included in the calculation.

Figure 2.7 compares the tip deflection per unit electric field for d_{31} and d_{33} unimorphs and bimorph cantilever actuators based on the equations given above. The bimorph considered here is in the parallel connection. An average elastic stiffness for the passive layer is calculated from the silicon-rich nitride (250 GPa) and zirconia (150 GPa) at 200 GPa. With the modulus of PZT (100 GPa), the elastic ratio is A=2.0. The thickness ratio, B=2.67, is obtained from fabricated devices. From figure 2.6 the delta parameter for A and B is about 0.31. This is not optimal, but is necessary for stress compensation. Figure 2.7 shows that the unimorph deflection is greater for the d_{33} mode than the d_{31} mode for the same electric field. This advantage is mitigated somewhat due to fabrication issues with the IDE. A large IDE spacing requires a larger voltage to maintain the same field value. This trade-off then depends on the technology used to pattern the IDE. The bimorph exhibts deflections several times larger than than either unimorph. In principle therefore, a bimorph switch would have a lower turn-on voltage, and, due to a greater blocking force, more reliable operation.

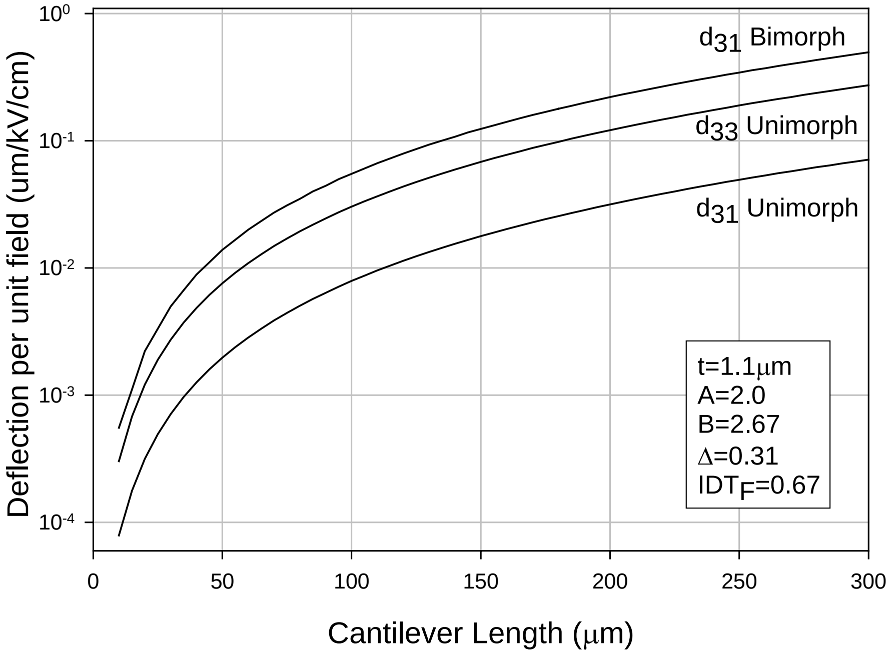

Figure 2.7 Tip deflection per volt for three designs as a function of length.

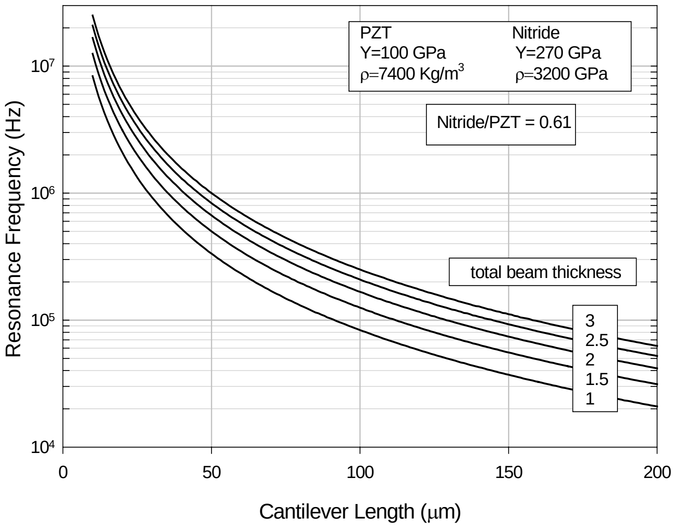

Figure 2.8 Resonance curves for a unimorph microactuator.

As is explained in chapter five, the switching performance of the devices is dictated by the mechanical resonance frequency of the structure. The natural, or resonance, frequency of a non-symmetric cantilever structure can be obtained by calculating the location of the neutral axis using the transformed cross section method, and the second moment of inertia using the parallel axis theorem. The resonant frequency, f_n, of a bilayer unimorph is given by,[10]

$$f_n = \frac{3.52t}{4\pi L^2}\sqrt{\frac{Y_p}{3\rho_p}}\Theta \qquad \Theta = \left[\frac{A^2B^4 + 2A(2B+3B^2+2B^3)+1}{(1+BC)(1+AB)(1+B)^2}\right]^{\frac{1}{2}} \tag{2.10}$$

where L is the length, Y_p and ρ_p are Young's modulus and the density of the piezoelectric material, and t is the total thickness. The factor Θ is a dimensionless parameter that is a function of the thickness, stiffness and density ratios. The resonant frequency for a simple bilayer structure consisting of PZT and silicon nitride of various beam thicknesses is displayed in figure 2.8. By tapering a cantilever its natural frequency can be increased. Calculating an average length, the natural frequency, f_t, of a tapered uniform cantilever relative to a non-tapered beam is given as,

$$\frac{f_t}{f_n} = \frac{L^2}{\bar{l}^2} = \left[\frac{1 + 2\dfrac{L}{W}\tan\theta}{\dfrac{L}{W}\tan\theta + 1} \right]^2 \tag{2.11}$$

where $\bar{l}$ is the average length. Figure 2.9 plots this normalized frequency as a function of the taper angle θ, and the width to length ratio. An increase of almost four fold is achieved by tapering, however, the blocking force is also decreased.

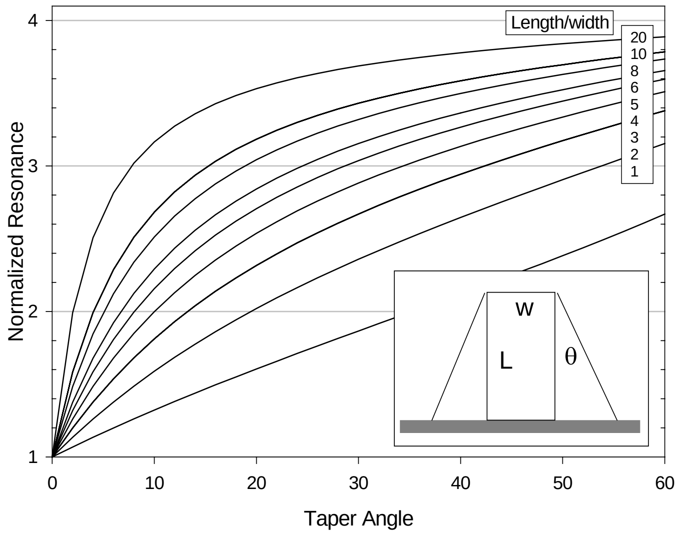

Figure 2.9 Normalized resonance for tapered cantilever beams.

2.2.2 Effective parameters

The analysis discussed above was derived for macro-scale actuators, and its applicability to micro-scale devices requires the adoption of effective parameters. As was discussed in chapter one, the mechanical clamping of thin films from the substrate affects the piezoelectric strain response. For micro-actuators, the thickness of the films is generally small compared with the length and width. For this condition, De Voe and Weinberg considered the beam to be in a state of plane strain.[3,12] In this state, the stress in the thickness direction and the in-plane strain are zero. The total strain is obtained when the generalized form of Hooke's law is added to the piezoelectric strain and is given by,

$$S_1 = \frac{\sigma_1}{Y} - \frac{\upsilon\sigma_2}{Y} - \frac{\nu\sigma_3}{Y} + d_{31}E_3 \qquad (2.12)$$

$$S_2 = -\frac{\sigma_1}{Y} + \frac{\nu\sigma_2}{Y} - \frac{\nu\sigma_3}{Y} + d_{31}E_3 \qquad (2.13)$$

$$S_3 = -\frac{\sigma_1}{Y} - \frac{\nu\sigma_2}{Y} + \frac{\nu\sigma_3}{Y} + d_{33}E_3 \qquad (2.14)$$

where ν is Poisson's ratio of the material. For the case of the d_{31} mode, a state of plane strain indicates that $\sigma_3 = 0$, and $S_1=S_2=0$. When these conditions are substituted into the above equations, effective values for the transverse piezoelectric coefficient and the elastic modulus are obtained and given by,

$$\begin{aligned} &d_{31} \rightarrow d_{31}(1+\nu) \\ &Y \rightarrow \frac{Y}{(1-\nu^2)} \end{aligned} \qquad d_{31} \text{ mode} \qquad (2.15)$$

For PZT, with ν =0.3, this indicates an increase in d_{31} of 30% and an increase in modulus of 10%. The assumption made in this analysis however, is that the material is isotropic with respect to the elastic properties. This however is certainly not the case for poled PZT ceramic. For bulk PZT (52/48) the ratio between $Y_1/Y_3 = 1.2$.[14] The width however does have an effect on the deflection. This was observed by Hou, in release cantilevers deflected by residual stresses. Computer modeling supports this and is discussed in chapter five.

2.2.3 Actuator Reliability

An analysis can be performed to predict the maximum acceleration or g-forces that the actuators and switches can endure. As a simple model, a uniform silicon nitride cantilever is used with a thickness of 1 μm and a length of 300 μm. The properties of vapor deposited silicon nitride films are listed in Table 2.1.[15] Only acceleration normal to the substrate is considered. A positive acceleration causes the cantilever to deflect toward the substrate until the gap is closed and contact is made with the transmission lines. This case is considered first. A negative acceleration causes the actuator to deflect away from the substrate. A sufficiently great acceleration causes the stress at the support to exceed the fracture strength of the nitride. The acceleration results in a uniform load on the cantilever given by the total mass multiplied by the acceleration. Using beam theory and the flexure formula,[16] the maximum stress, σ, a the support is given by,

$$\sigma_{\max} = \frac{3\rho a L^2}{h} \tag{2.16}$$

where ρ is the density, a is the acceleration, h is the thickness of the cantilever, and L is the total length. By using the values for the cantilever geometry and the mechanical properties of the silicon nitride, it can be calculated that such a device can withstand a negative acceleration of $6\text{x}10^6$ m/s^2 or about $6\text{x}10^5$ G. A similar calculation can be made for a positive acceleration. The positive acceleration required to turn the switch on is given by,

$$a = \frac{2\delta Y h^2}{3\rho L^4} \tag{2.17}$$

where Y is the elastic modulus of the nitride and δ is the gap between the free end of the cantilever and the transmission lines. Using the formula and the given properties, the device can handel up to 1400 G before switching on. These results indicate that MEMS strucutres, and these switches in particular, are substantially robust.

Table 2.1 Properties of LPCVD silicon nitride films

Density	3000 kg/m^3
Elastic modulus	250 GPa
Fracture strength	5 GPa

* Source: [15]

2.3 Conclusions

This chapter discussed the design of the microactuators and switches based on a surface micromachining approach. A unimorph, with low-stress silicon nitride as the passive layer was selected as the microactuator. The final design consisted of gold transmission lines deposited on a silicon oxide dielectric layer below the free end of the cantilever actuator. A quasi-static analysis base on beam theory revealed that an optimum thickness ratio exists based on the elastic properties of the materials used. The analysis also showed that a greater deflection and blocking force are possible using the longitudinal mode. However, this advantage is mitigated by the design of the electrode structure. It was also shown that bimorph actuators are capable of greater deflection and blocking forces and are therefore a possible alternative.

References

---

[1] J.G.Smits, S.I. Dalke, T.K.Cooney, “The constituent equations of piezoelectric bimorphs,” Sensors and Actuators A, 28, 1991.

[2] C.B.Sawyer “The use of Rochelle salt crystals for electrical reproducers and microphones,” Proc. Inst. Radio Eng. 19(11), 1931.

[3] D.L. DeVoe, A.P. Pisano, “Modeling and optimal design of piezoelectric cantilever microactuators,” J. of MEMS, 6(3), pp. 266-270, 1997.

[4] D. Polla, L. Francis, “Processing and characterization of piezoelectric materials and integration into micromechanical systems,” Annual Review of Materials Science 28, pp.563 1998.

[5] B.A. Tuttle, J.A. Voigt,T.J. Garino, D.C. Goodnow, R.W. Schwartz, D.L. Lamppa, T.J.Headly, M.O. Eatough, “Chemically prepared $Pb(Zr,Ti)O_3$ thin films: the effects of orientation and stress,” Proc. 8th Inter. Sym. Application of Ferroelectrics, 344, 1992.

[6] M. Madou, *Fundamentals of Microfabrication*, CRC press, 1997.

[7] M. Sekimoto, H. Yoshihara, T. Ohkubo,” Silicon nitride single-layer x-ray mask,” J.Vac. Sci. Technology, 21(4), 1982.

[8] B. Xu, Y. Ye, L.E.Cross, J.J. Bernstein, R.Miller, “Dielectric and hysteresis from transverse electric fields in lead zirconate titanate thin films,” App. Phy. Lett., 74, pp. 3549, 1999.

[9] E. Hong, Surface micromachined peristaltic pumps using lead zirconate titanate film, Ph.D. thesis, The Pennsylvania State University, 2004.

---

[10] Q.-M. Wang, X.-H. Du, B. Xu, L.E. Cross, "Constitutive Equations of symmetrical triple layer piezoelectric benders," IEEE Trans UFFC, 46(6), pp. 1343-1351, 1999.

[11] M.R Steel, F. Harrison, P.G. Harper, "The piezoelectric bimorph: an experimental and theoretical study of its quasistatic response," J. Phys D: App. Phys., vol. 11, pp. 979-989 1978.

[12] M.S. Weinberg, "Working equations for piezoelectric actuators and sensors, Journal of microelectromechanical systems," 8(4), pp. 529-533, 1999.

[13] S. Timoshenko, "Analysis of bi-metal thermostats" J. Optic Soc Am, 11(3), pp. 233-255, 1925.

[14] K. Uchino, *Ferroelectric Devices*, Marcel Dekker, 2000.

[15] R.L. Edwards, G. Coles, W.N. Sharpe, "Comparison of tensile and bulge test for thin-film silicon nitride," Experimental Mechanics, 44(1), pp. 49-54, 2004.

[16] R.C. hibbeler, Mechanics of Materials, Prentice Hall, 1994.

Chapter 3

Actuator & Switch Microfabrication

3.1 Microfabrication sequence

The process flow used to fabricate switches is presented in this section. This final process outlined here, is the result of numerous iterations. The fabrication sequences for unimorph and bimorph actuators are also presented. Greater detail pertaining to each process step is provided in section 3.2 and in chapter 4. An alternative version of the switch fabrication process is also given.

3.1.1 Fabrication sequence: microswitches

The Self-Aligned Contact (SAC2) process is outlined in this section and depicted in figure 3.1. The figure shows a cross-sectional view at the end of the cantilevers. Fabrication began with the wet thermal oxidiation (1.5μm) of silicon wafers to produce insulating substrates. The wafers used were single-side polished n and p type, <100> with 1-10 Ω-cm resistivity. Outsourcing of deposition of the silicon nitride and polysilicon films, required that 4” diameter wafers be used. Two microns of sacrificial polysilicon was deposited by low-pressure chemical vapor deposition (LPCVD) at 625°C. This service was provided by the University of Michigan and typically done in lots of 20-25 wafers. Following a standard RCA clean, a thermal oxide was grown on the polysilicon in dry oxygen at 1000°C for about an hour to obtain a thickness of 600-650Å. This oxide acts as an etch-stop layer in the final release. A low-stress silicon nitride Si_xN_y (0.4-0.6

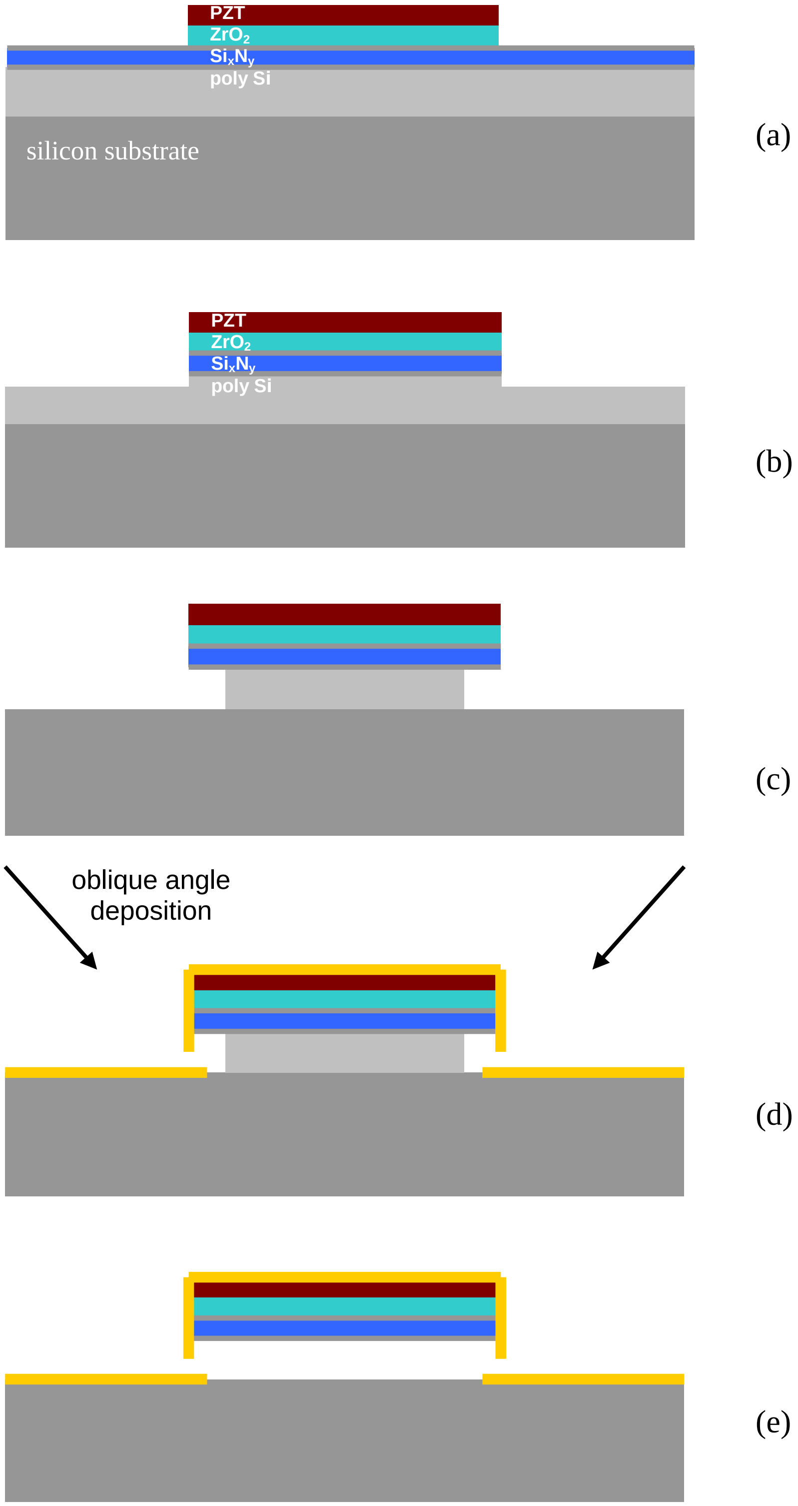

Figure 3.1 Cross-sectional lengthwise view of the SAC2 switch fabrication sequence (a) Pattern definition by ion beam etching, (b) RIE of nitride (c) removal of field polysilicon, (d) contact and wave-guide metallization, (e) structure release.

μm) was deposited as the structural layer by LPCVD at 835°C at the University of California at Berkeley. A thin (≈500 Å) silicon oxide layer was then reactively ion-beam sputtered to promote adhesion of subsequent films with the silicon nitride. A 300 nm buffer layer of zirconia was spun on using sol-gel techniques. Samples were then annealed in a furnace at 700C for one to three hours in an air ambient. Whole wafers were typically processed up to this point and then broken into quarters for further processing. Two to six layers (150 – 450 nm) of PZT were deposited, also using sol-gel. The stack was then patterned using a combination of ion-beam etching for the PZT and Zirconia, and reactive ion etching (RIE) for the silicon nitride. Photoresist or chromium masks were used to define the pattern during etching. The samples were masked and milled for about 20-40 min. Due to the lack of an etch-stop layer or end point detection capabilities, the etch proceeds through the zirconia into the nitride. It is critical that the ion-beam etching proceed completely through the zirconia (figure 3.1a). The remaining nitride, thin barrier oxide and part of the sacrificial polysilicon was etched by reactive ion etching (RIE) for 5-10 min (figure 3.1b). Any remaining zirconia will prevent the etching of the nitride. The polysilicon in the field region between the devices was etched in gaseous XeF_2 (figure 3.1c). This etch terminated on the thick thermal oxide and undercuts the structures (5-10μm). The silicon nitride was protected from the XeF_2 by the thin oxide layer. A blanket Cr(100Å)/Au(4000Å) layer was sputter deposited at an angle of 45° to facilitate deposition beneath the structures (figure 3.1d). The transmission lines and contacts were patterned by wet etching the gold and dry plasma etching the chromium. The interdigitated electrodes were patterned using a bi-layer lift-off technique. A Cr(100Å)/Au(2200Å) deposition was performed followed by resist liftoff in acetone and developer. The structures were then released by removing the remaining polysilicon in XeF_2 (figure 3.1e). The dry nature of the etch eliminates stiction related yield losses.

3.1.2 Alternative Process

The Self-Aligned Contact (SAC1) process sequence and design is depicted in figure 3.2. This process was developed to produce ‘winged’ contacts with a larger contact area than that in the SAC2 process. The stack deposition is the same in both and is described in section 3.1.1. Pattern definition was also accomplished by ion-beam etching (figure 3.2a). After milling, the exposed sacrificial polysilicon was used as surface on which to deposit the ‘wing’ portion of the contacts. Platinum was ion-beam sputter deposited and patterned by lift-off to create the contacts (figure 3.2b). Deposition on the side-walls of the photoresist, known as flagging, was intentional as it created a three dimensional structure which increased rigidity. The polysilicon in the field region and below the contacts was then removed with XeF_2. The structures were undercut about 5 μm after the etch. A blanket Cr(10nm)/Au(400nm) deposition was performed at 45° of normal to aid in deposition below the contact. Transmission lines were patterned by wet etching the gold and dry etching the chrome (figure 3.2c). The samples, pieces of a wafer, were then coated with resist and diced into rectangular dies. The resist covering each die was then removed in acetone and rinsed in DI water. The devices were released by removing the remaining, supporting silicon in XeF_2 (figure 3.2d). Completed dies were then examined using optical and interference microscopes and an SEM. On a probe station, functioning devices were identified. Those dies were then glued to 40 pin ceramic packages, and the operational devices were wire bonded.

3.1.3 Fabrication sequence: unimorph microactuators

The fabrication process for unimorph actuators was the same as that presented for switch with several simplifications. First, the transmission lines and contacts were omitted. The polysilicon and insulating oxide are not necessary so the stack, beginning with the silicon nitride and thin oxide, was deposited directly on a silicon wafer. The wafer itself acts as the sacrificial layer. The IDEs were deposited on the PZT using lift-off prior to ion milling when resist masks were used. When chrome masks were used, the stack was first patterned by ion milling and RIE, and then the IDE were deposited and patterned by lift-off.

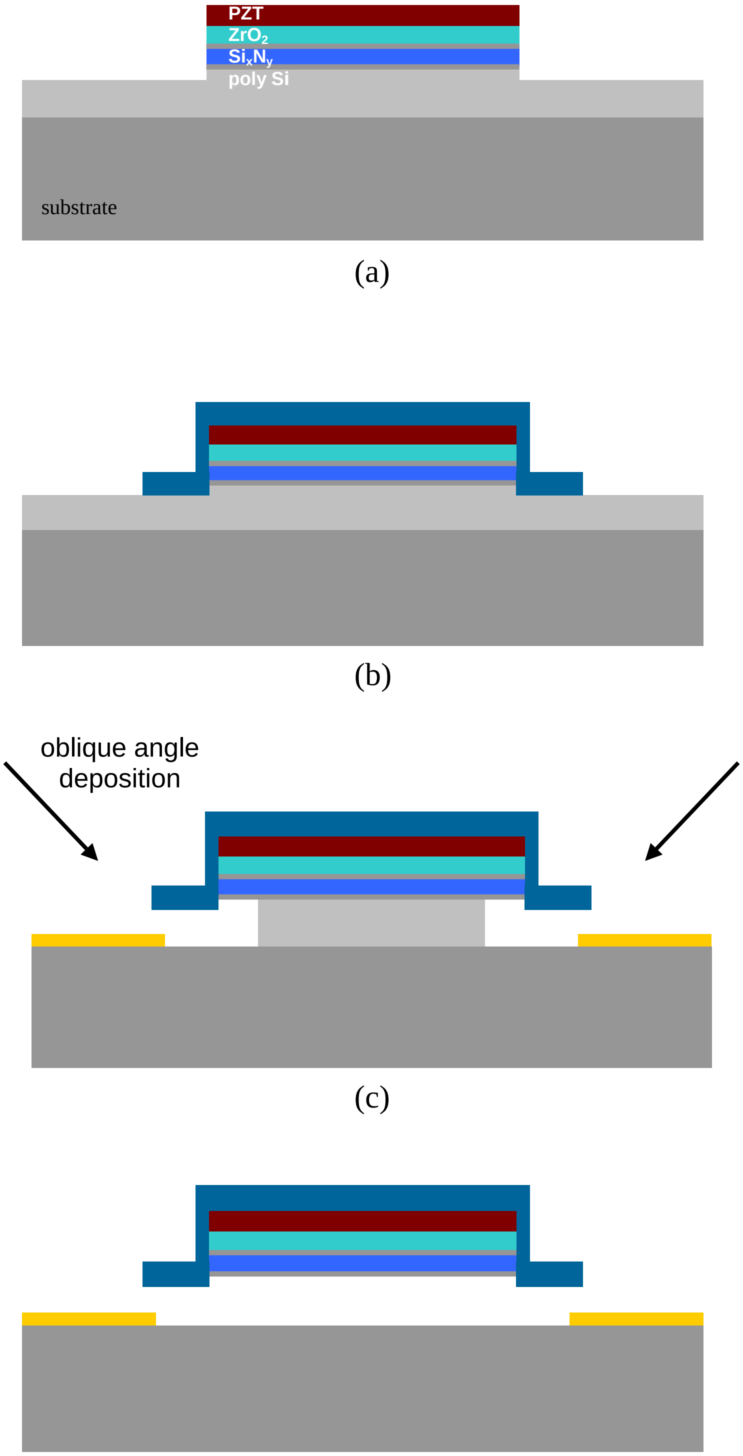

(a)

(b)

(c)

(d)

Figure 3.2 Cross sectional view of the SAC1 switch fabrication sequence. (a) Pattern definition by ion beam etching. (b) Contact definition by lift-off (c) Removal of field polysilicon in XeF$_2$, waveguide, and IDE (lift-off) metallization. (d) Release by etching remaining polysilicon.

3.1.4 Fabrication sequence: bimorph microactuators

The fabrication sequence for the bimorph actuators is depicted in figure 3.3 as a cross-sectional side-view of a cantilever and contact windows. The fabrication of bimorph actuators began with the dry thermal oxidation of a 4” silicon wafer at 1000°C to obtain a 100 nm silicon oxide barrier layer. This layer is required to prevent the platinum from reacting with the silicon. Titanium (20nm) and platinum (200nm) were sputtered consecutively without breaking vacuum at 300°C and 5 mtorr to form the bottom electrode. At this point the wafers were broken into quarters. Three to four layers (450-600 nm) of PZT were spun-on and annealed using the sol-gel method described in section 3.3 to form the bottom piezoelectric layer. The middle electrode was deposited by sputtering platinum under the same conditions and thickness as the first. The same number of layers of PZT were again spun-on and annealed. To complete the stack, platinum was sputtered at the same conditions and thickness to create the top electrode. Some samples were then annealed at 700°C for five minutes to increase the room-temperature stress of the platinum in the top layer.

Ion-beam etching was used to pattern the bimorph cantilevers and to open windows in the stack to contact the bottom and middle platinum electrodes. A CrO_x/Cr (0.9-1.1µm) mask was sputtered on the sample. The chrome mask was patterned using an acid based wet chrome etch and the photoresist was then removed. Additional information on hard masks is given in section 3.4.3. The first ion-beam etch step was performed to partially pattern the cantilevers (figure 3.3a). An etch depth in excess of the bottom electrode and silicon oxide thickness’ combined (310nm) was required at this step. Due to time constraints, for the actual manufactured bimorphs only the top and middle platinum electrodes were contacted. The second window to contact the bottom platinum was not opened, but the process steps are as follows. A window in the chrome mask is opened by wet etching. The second ion-beam etch step is performed to a depth of the PZT and platinum thickness’ combined (figure 3.3b). A second window is opened in the chrome mask again by wet etching using the same photolithographic mask shifted relative to the first window. The final ion-beam etch is performed to a depth not exceeding the PZT and platinum thickness’ (figure 3.3c). At this point the middle and bottom platinum should be

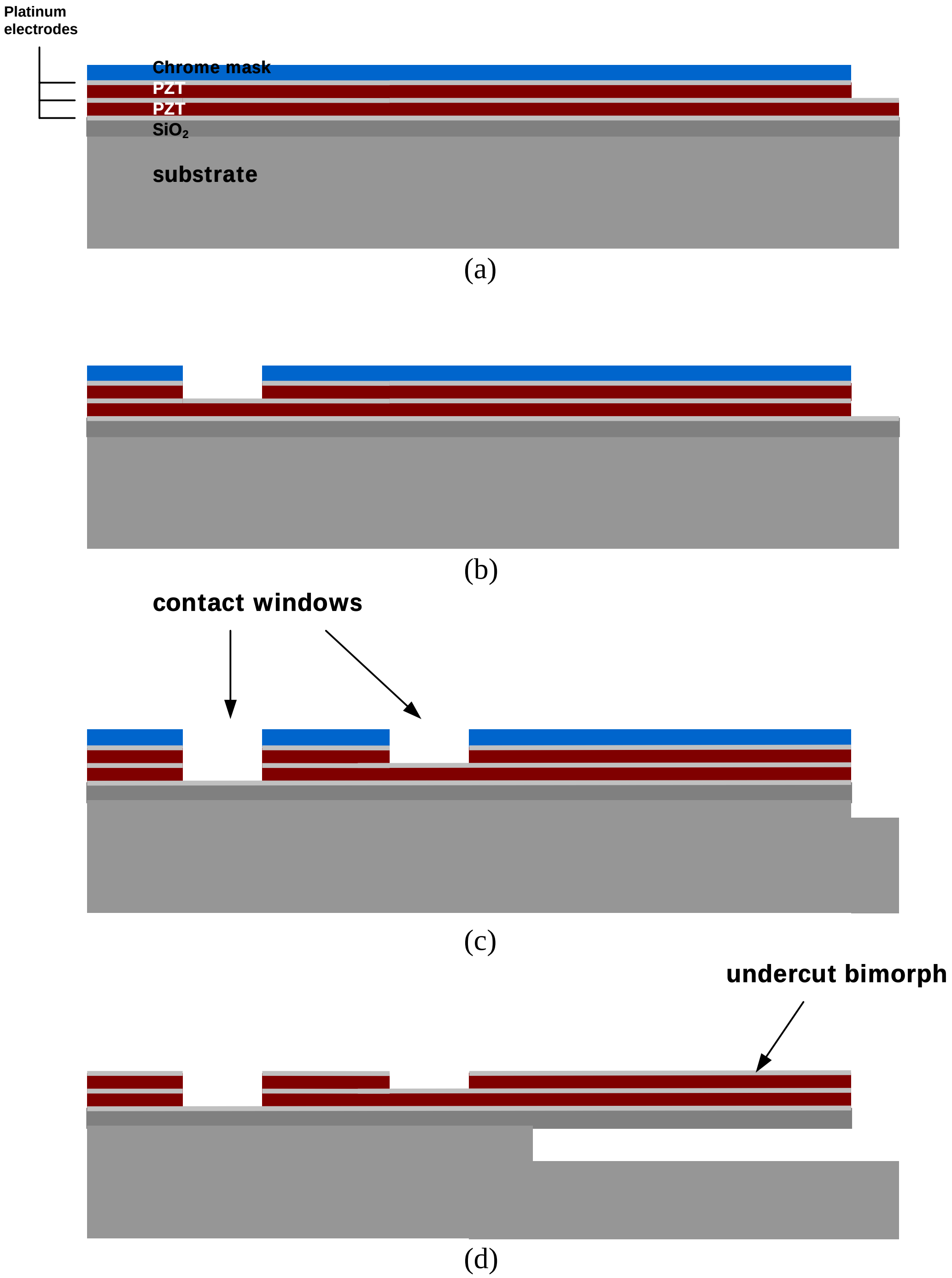

Figure 3.3 Cross-sectional lateral view of bimorph fabrication sequence. (a) Partial device pattern definition (b) Initial bottom Pt window etch (c) Middle Pt window, and completion of bottom Pt window and device (d) Remove mask and release bimorph in XeF

exposed but additional milling may be necessary. Remaining PZT could also be removed with dilute hydrofluoric and hydrochloric acids using the platinum as an etch-stop layer.

This wet etching however could undercut the electrodes enough to cause electrical shorts. This is why milling is preferred. Finally, the devices are release by etching the underlying silicon in XeF_2 (figure 3.3d).

3.2 Processing parameters and issues

Provided in this section, are the process parameters and issues for each individual fabrication step.

3.2.1 Film Adhesion

Figure 3.4 shows small cracks (1-3μm) that developed during the deposition of PZT on zirconia on Si_xN_y. This occurred after one or two layers had been deposited and annealed. Poor adhesion between the zirconia and silicon nitride was suspected. However, the cracking was not observed during the deposition and annealing of the zirconia. An attempt was made to oxidize the silicon-rich nitride in hopes of forming a thin oxynitride film. A wet oxidation was performed at 840°C for three hours. Mixed results were

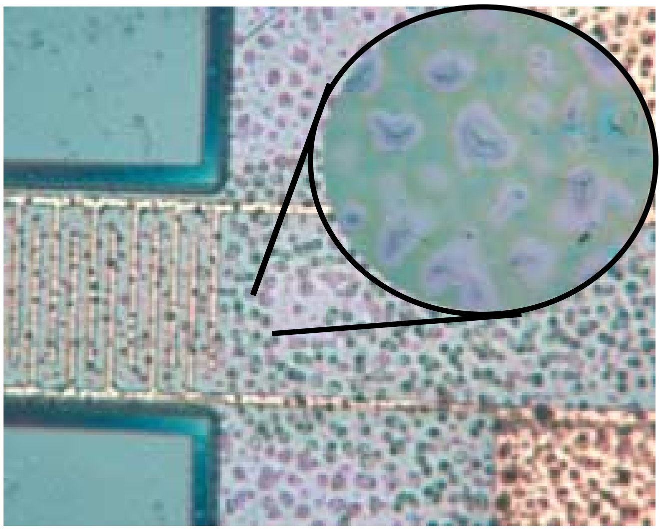

Figure 3.4 PZT and zirconia cracking due to poor adhesion with nitride.

obtained by this method. The problem has been eliminated completely by reactively ion-beam sputtering 100 nm of silicon oxide over the silicon nitride.

3.2.2 Titanium Oxide films

Titanium oxide films were investigated as an alternative to sol-gel deposited zirconium oxide barrier layers. The titania films were dc magnetron reactively sputtered from a Ti target in a parallel plate system using argon with 1% oxygen at 150 mtorr. Deposition occurred with the substrate heated to 180°C, a bias of 290 volts and a power level of 45 watts. After deposition, the films were annealed in an oxygen ambient at 700°C for 3 hrs to insure complete oxidation and to densify the film. This anneal also served to test if the films could withstand the elevated temperatures required to crystallize the PZT. Twelve minutes of sputtering resulted in a film thickness of about 100 nm. Unimorph actuators were produced using titania barrier layers.

3.2.3 Reactive Ion Etching (RIE)

Silicon nitride and silicon oxide films are patterned by reactive ion etching in a CF_4:O_2 (28:2.8) chemistry in a parallel plate system (Plasma Technologies). Conditions were as follows: 80 W, 100 mtorr, $150V_{dc}$. Nitride etch rates were observed to be 75-100 nm/min, with silicon oxide showing similar values. Shipley 1800 series photoresist (baked <120°C) was found to etch at 25 nm/min under these conditions.

3.2.4 Metallization: waveguides, contacts and electrodes

As with many other aspects of the process, the transmission lines, contacts and electrodes went through several design and test iterations. The first unimorph actuators produced, had Cr/Au IDEs patterned by a lift-off process using 1827 photoresist. This method resulted in a low and variable yield, but was adequate to demonstrate the concept. A photoresist designed for lift-off, BPRS100 (Olin Hunt), was tried in an effort to improve the yield, but the results were similarly poor. The same lift-off method was initially also used to pattern the transmission lines and contacts. Figure 3.5 (a) shows a transmission line, contact and IDE all patterned in a single step. It is readily apparent from the SEM image that flagging caused an electrical short across the transmission lines. The flagging was exacerbated by the oblique angle required during deposition. An alternative way to pattern the transmission lines was required.

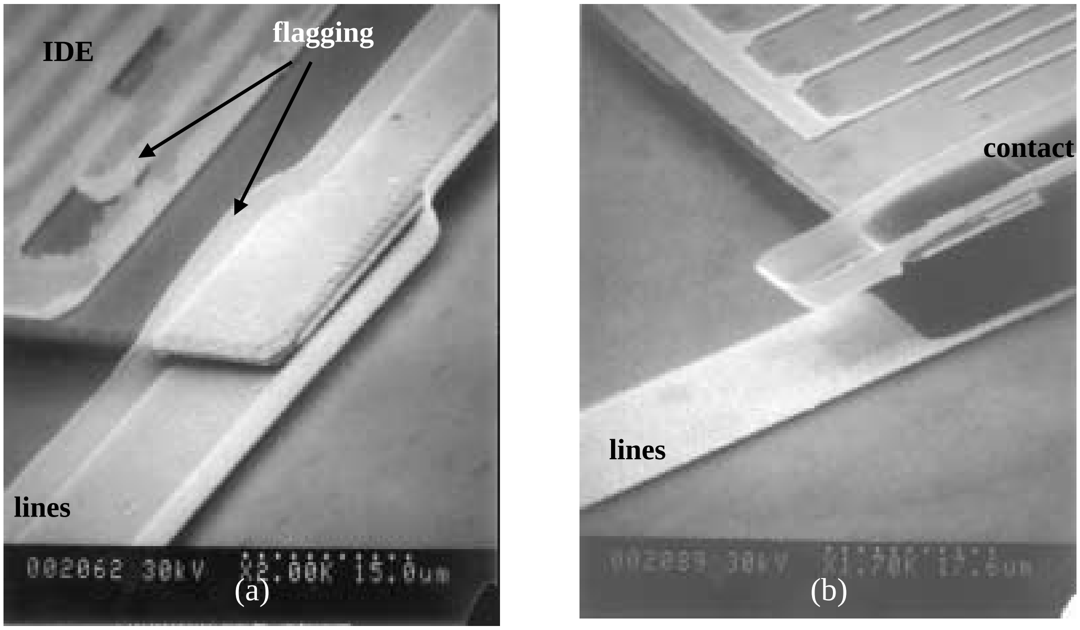

Figure 3.5 (a) Transmission lines, contacts and electrodes patterned by single resist lift-off method. Lines shorted due to flagging. (b) Etched lines and electrodes showing no flagging. Flagging on contact increases rigidity and is intentional.

Etching was investigated as a way to simultaneously pattern the IDEs and waveguides. The gold films were etched using an aqueous potassium iodide and iodine solution. This solution was prepared with 4g KI : 1g I_2 : 150 ml H_2O and etched at a rate of about 25 nm/min. Wet-etching the thin chrome adhesion layer however presented a problem. The chrome was etched in both acidic, $Ce(NH_4)_2(NO_3)_6$ + HNO_3, and basic, $K_3Fe(CN)_6$ + NaOH (Kodak) aqueous solutions. The electrodes were observed to delaminate due to the rapid undercutting of the chrome, probably a result of the galvanic effect.[1] Those that were not removed exhibited circular ferroelectric P-E loops. Experiments also showed that wet etching the gold, and dry reactive-ion-etching the chrome in a Cl_2 + Ar + O_2 plasma, produced good electrodes. Figure 3.5 (b) shows the end of a cantilever with IDEs and transmission lines deposited in a single step and patterned using etching (SAC1 process). The platinum contact was patterned by lift-off.

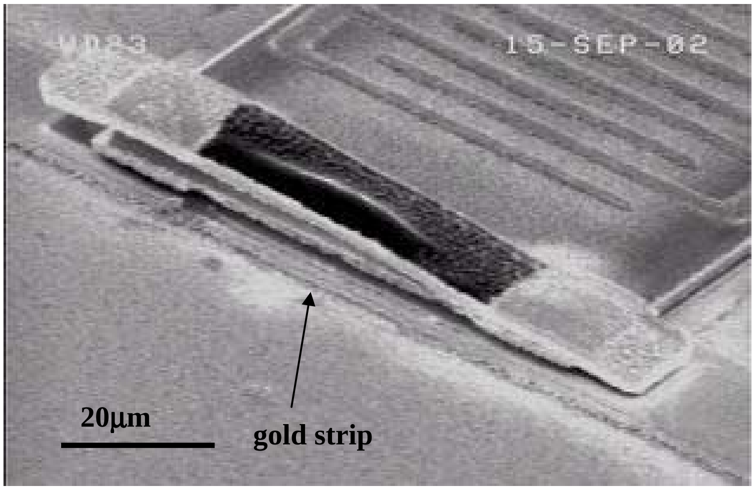

Figure 3.6 Residual gold strip, resulting from under exposed resist, shorting transmission lines.

Completion of the first switches revealed that most of the transmission lines were electrically shorted by a thin strip of residual gold at the end of the cantilevers that had not been removed (figure 3.6). This was caused by underexposed resist at the end of the cantilevers. Photoresist is thicker when spun over large step heights, and therefore requires a longer exposure. Compensation of this by increasing exposure however causes overexposure of the interdigitated electrodes, and complete removal during developing. For this reason, a single-step metallization was abandoned, and the IDEs mask was decoupled from the transmission lines mask. This allowed the exposure time to be tailored for each step. The two-step metallization approach introduced another problem: etching to pattern the IDEs would remove the transmission lines. To avoid this, the transmission lines were etched and a lift-off was performed for the IDEs. An improved lift-off process was then required.

The solution was a bi-layer process using Microchem's LOR series resist, which creates a re-entrant profile that facilitates lift-off (figure 3.7). Although this is a commercial process, a test matrix is required to find viable parameters. Test samples were prepared using LOR3A, LOR5A, and 1827 and 3012 photoresists. Positive results were not found with the 1827 resist. It was found that under certain conditions, LOR5A/3012 produces good electrodes with repeated high yield and no flagging (figure 3.5b). It was noticed that the dissolution rate of the LOR in developer is very sensitive to the bake time and temperature. The optimized process parameters for the bi-layer lift-off process are listed in Table 3.1. Based on visual observation and electrical testing it appears that the recommended developer, 0.26M TMAH (AZ300), is compatible with PZT.

Table 3.1 Bi-layer lift-off process for IDEs

1	Sample clean & dehydrate : acetone & IPA or DI H_2O
2	Spin LOR5A 3000 rpm 40 sec
3	HP* bake 150°C 60 sec
4	Spin 3012 4000 rpm 40 sec
5	HP soft bake 100 °C 60 sec
6	Expose 35 – 45 sec @ 3.0 mW/cm^2
7	Develop 1:15 – 1:30 min in 0.26M TMAH (AZ300)
8	Evaporate or ion-beam sputter metal (200 -300 nm)
9	Acetone to remove 3012 & developer for LOR

* Hot Plate

Figure 3.7 Re-entrant profile created with LOR resist in bi-layer lift-off process used for IDE.

3.2.5 Silicon oxide sacrificial layer & wet release

Micromachined structures are made freestanding by bulk etching the substrate or by surface etching an underlying sacrificial layer. The first iteration of the design followed the route of many micro sensors and actuators by employing silicon dioxide as the sacrificial layer. This layer is removed in aqueous hydrofluoric acid (HF) and the

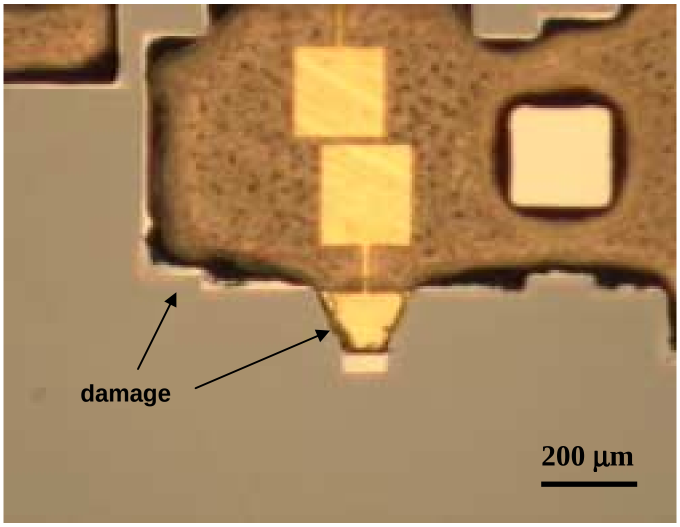

Figure 3.8 Damage to PZT encapsulated with hard-baked photoresist after HF etching.

silicon substrate serves as the etch-stop. This technique is problematic for a couple of reasons. First, HF readily attacks PZT even in low concentrations, and so, an effective encapsulation is required. Figure 3.8 shows a microscope image of the damage to PZT due to HF, even though it was protected with a double layer of hard-baked photoresist. The solution used was HF:HCL 1:1 and had a lateral etch rate of 12μm/min for a 2μm sacrificial low-temperature oxide.[2] Similar damage to PZT was observed using only dilute HF. The black areas on the image are where the acid penetrated the mask, probably at the interface, and attacked the PZT. Alternative encapsulating materials include silicon nitride, but pinholes and final removal become issues. This nitride can remain as part of the structure, but this may alter the operation of the device. The second difficulty with wet release is stiction, and is a common problem in a microsystems.[3] During drying, the surface tension of the rinse water can cause the released structures to deflect toward the substrate. If this deflection is large enough, the structure becomes pinned to the substrate as a result of van der Waals forces and hydrogen bonding. Ultimately, stiction reduces yield as the microstructures cannot be recovered. Changing to a dry etching technique, such as with xenon difluoride, eliminates both problems. This has been one of the cornerstones of a robust cantilever actuator process.

3.2.6 Xenon difluoride etching

The etching of silicon for MEMS has been demonstrated by various methods.[4] Vapor-phase etching of silicon has been reported using xenon difluoride. The substance is a white crystalline solid at standard conditions, and sublimes at about 4 Torr at room temperature.[5] XeF_2 reacts spontaneously with silicon by the reaction expressed in equation 3.1. The process occurs by the following steps: the adsorption of the XeF_2

$$2XeF_2 + Si \rightarrow 2Xe + SiF_4 \tag{3.1}$$

molecule to the silicon surface, dissociation, reaction of the atomic fluorine with silicon, and the desorption of the byproducts as gases.[6] The etch is generally isotropic and a high degree of selectivity has been observed over many materials used in microfabrication. The reaction is exothermic and may result in an increase in local temperature, especially in thermally isolated structures. This effect is mitigated by the use of pulsed rather than continuous etch systems.[7] The absence of any liquid phase eliminates stiction related problems.

Devices were etched in a Xactix Xetch® XeF_2 etch system at Carnegie Mellon University. Operation of the pulsed system is as follows. The cycle begins by evacuating the expansion and etching chambers to a tenth of a torr. This allows the XeF_2 crystals to sublimate and fill the expansion chamber to a selected pressure. The etching and expansion chambers are then connected and the pressure quickly equilibrates to 1.1 to 1.4 torr. Etching begins immediately and the pressure begins to rise due to an increase in the total number of moles of the gases. After a selected etch time has passed, both chambers are again evacuated to a tenth of a torr, held for 10 seconds and the process repeats. The advantage of pulsed systems over continuous systems is that the quantity of etchant delivered each cycle is known and can be controlled.

The etching conditions used in the fabrication of devices are detailed in Table 3.2. Data compiled over numerous runs revealed a lateral and vertical etch-rate for single crystal silicon of about 0.1 µm/cycle. The 2 µm thick polysilicon on oxide was observed to etch at 2.1 to 2.9 µm/cycle. These etch rates however are dependent on the quantity of silicon present in the chamber. It was also observed that the etch rate in the first few cycles was very low, presumably due to the native oxide on the silicon. Silicon undercutting was used as an indicator to ascertain the progress and completion of the release process. The undercutting of both the polysilicon and the silicon nitride, of a cantilever without the barrier oxide, are visible in figure 3.9. Claims were made in the literature that stoichiometric silicon nitride does not etch in $XeF_{2,}$ and that etching of silicon-rich nitride can be retarded or halted by the addition of nitrogen.[8] Tests however, showed that 0.4 µm of silicon-rich nitride was removed in 40 cycles (40min etch) with nitrogen partial pressures of three, and six torr. A dry thermal oxide (1000°C) was tested as a barrier layer to protect the nitride and found to etch at approximately one Å/cycle. An oxide layer (600 Å) below the nitride was therefore adopted as an etch-stop layer.

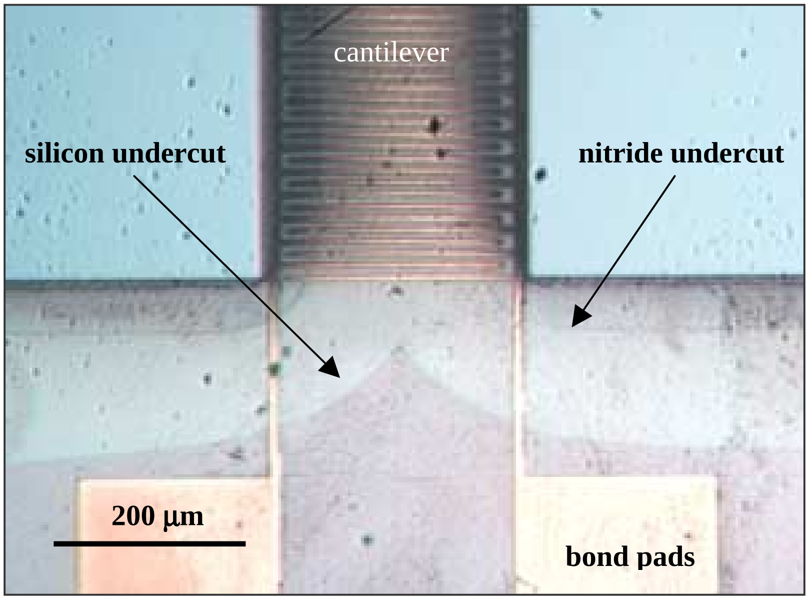

Figure 3.9 Undercutting of a cantilever (200µm wide) without barrier oxide layer during XeF_2 release etch. The undercutting of silicon and nitride are visible.

Table 3.2 Measured Xenon difluoride etch rates & parameters

	XeF_2 pressure	N_2 pressure	etch time/cycle	cycle time	Etch rate (μm/cycle)
SC-Silicon	3 torr	0 torr	45 sec	90 sec	0.1
Polysilicon (2μm)	3 torr	0 torr	45 sec	90 sec	2.5

[*] etch rate strongly dependent on quantity of silicon exposed

Observations made regarding the compatibility of gold films with XeF_2 mirror the same inconsistency reported in the literature.[4,7] During structure release, gold IDEs were exposed to the etchant for up to 450 cycles and showed no evidence of any reaction. This was confirmed on several occasions. On the last run, under the same etching conditions, the gold was attacked and completely removed in some areas. Figure 3.10 shows a device where one of the gold bond pads was almost completely removed. The gold films were deposited by two different methods. The gold deposited by ion-beam-sputtering showed no attack, while the electron-beam evaporated gold, on the last run, did. A curious

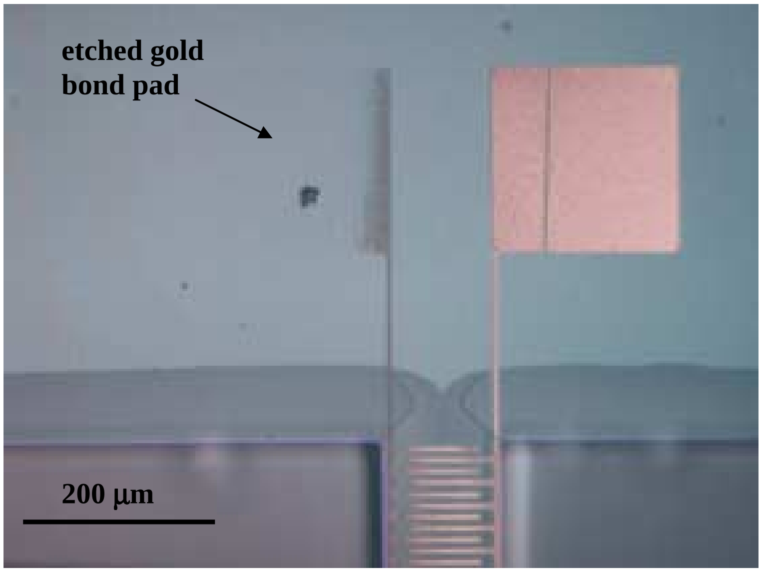

Figure 3.10 Evaporated gold IDEs attacked by XeF_2. Left bond pad almost completely removed while right one remains.

observation is that the same evaporated gold, deposited on a PZT test sample showed no attack. As the PZT test sample had little exposed silicon, the temperature may have not reached a critical level. Possibly, an elevated temperature is required for gold etching in XeF_2.

An new e1 series Xetch system was purchased from Xactix at the latter part of this work. The two systems are very similar in operation and design. The first runs on the new etch tool revealed a very rough silicon surface in comparison with samples etched on the older machine. Figures 3.11 and 3.12 show the surface of silicon etched with the older tool and the new tool respectively. A series of test etches were performed to find etch conditions that would reduce the apparent roughness. None were found to be successful and several plain silicon samples were observed to turn a light gray color during exposure. The color change and observed roughness are likely due to the formation of an unknown film on the silicon. Figure 3.13 shows this film on silicon in the area between devices, and figure 3.14 shows the film pulling a released cantilever causing it to bend downward. This film may be a silicon-fluorine polymer that is believed to form in the presence of water.[9] Further efforts to eliminate the film and decrease the roughness were not successful. It was later found that the pressure gauges on the etch tool were not properly calibrated. If the chambers were not pumped down to a low enough pressure, a partial pressure of

Figure 3.11 Smooth surface of SC-silicon etched in XeF_2.

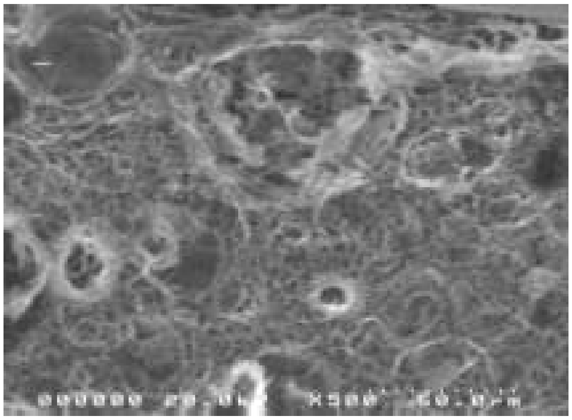

Figure 3.12 Rough surface of SC-silicon etched in XeF_2 with the new Xetch system with improperly calibrated pressure sensors.

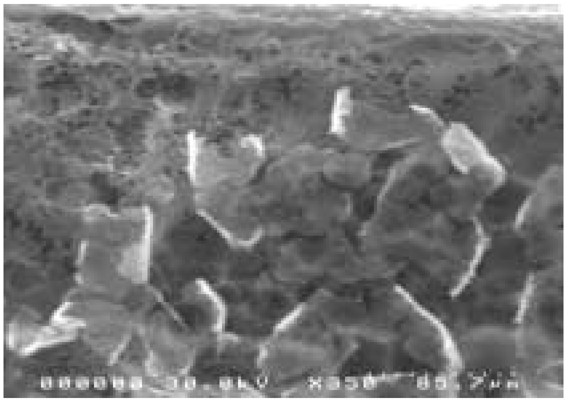

Figure 3.13 Unknown white/grey film growing on Si surface during XeF_2 etching.

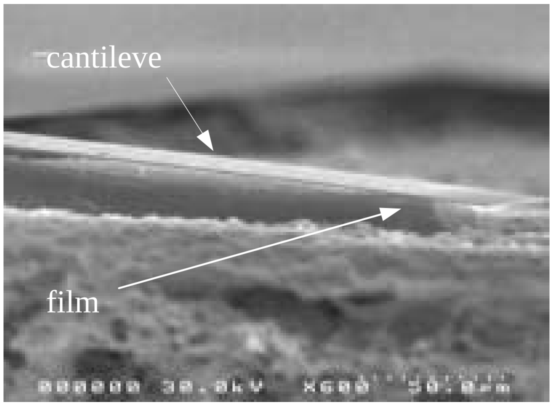

Figure 3.14 Film holding down a cantilever after silicon beneath has been etched

water could have been present as suspected. With the sensors now properly calibrated, additional tests can support this hypothesis.

3.3 PZT & zirconia films processing & characterization

The PZT and zirconia oxide films prepared in this study were deposited by a sol-gel method described in this section. The sol-gel method used is a modification of that originally developed by Budd et al.[10] The solution prepared was designed to produce PZT films with a 52mol% Zr and 48mol% Ti stoichiometry. This was the only composition made. The structural and electrical characterization of the zirconia and PZT films is also discussed.

3.3.1 PZT film processing

The process flow for the synthesis of PZT solution and spin-casting deposition is outlined in figure 3.15. The metalorganic precursors used were lead acetate trihydrate ($Pb(CH_3COO)_2{\cdot}3H_2O$), zirconium n-propoxide ($Zr(C_3H_7O)_4$) and titanium iso-propoxide ($Ti[OCH(CH_3)_2]_4$), and the solvent was 2-methoxyethanol ($CH_3OCH_2CH_2OH$) (2-MOE). In a dry rotary flask, the lead precursor and solvent were combined, and to aid the dissolution, the flask was rotated and heated to 115°C in an oil bath. 20 mol% excess Pb

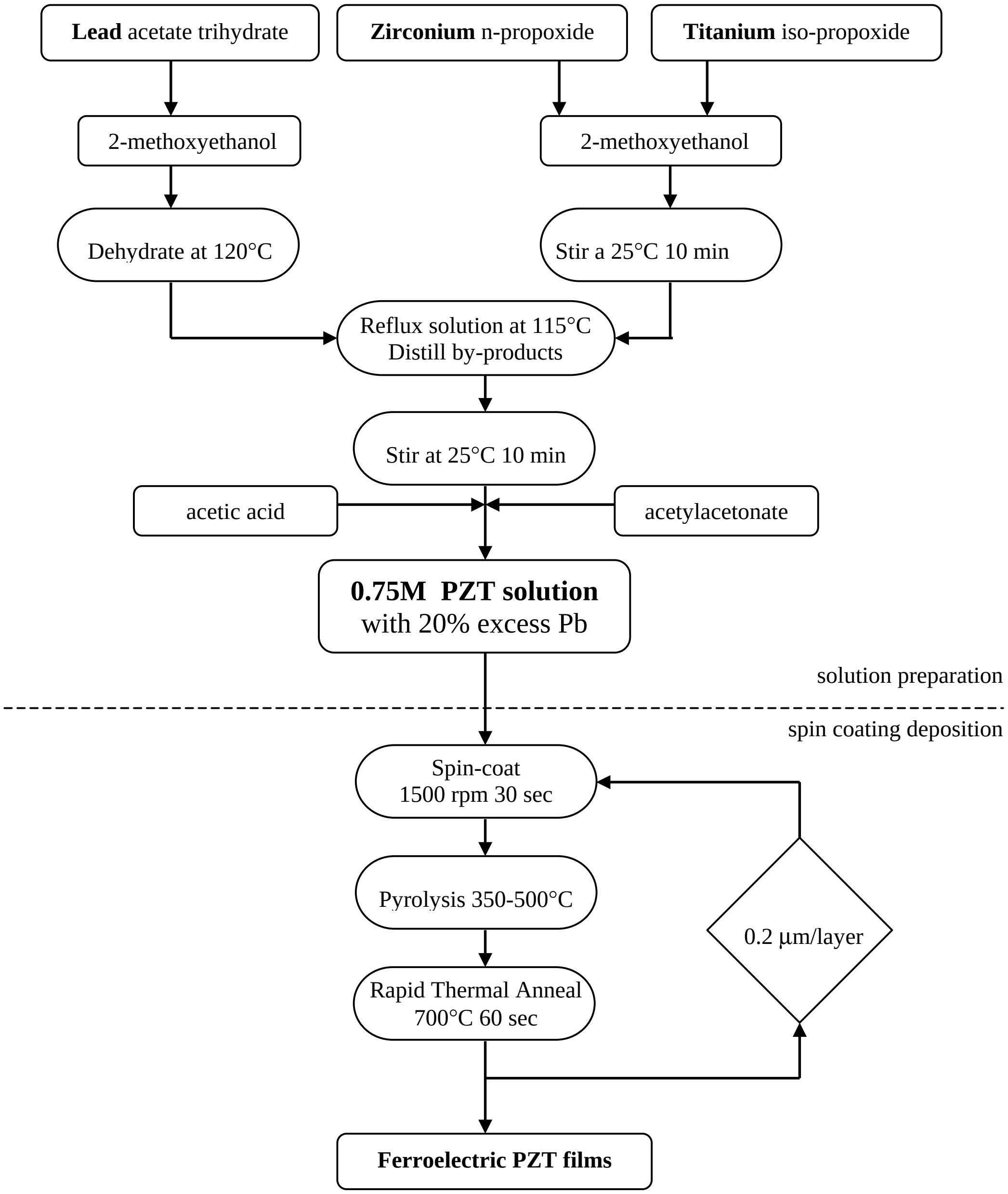

Figure 3.15 PZT solution preparation for sol-gel deposition

was used to compensate for its volatility during the deposition anneals. Separately and in a glove box, a mixture of 2MOE, zirconium n-propoxide, and titanium iso-propoxide was prepared with the zirconium n-propoxide added first to the solvent to keep the titanium iso-propoxide from hydrolyzing. The solution containing the lead precursor was then vacuum distilled to a dry white powder and after cooling to room temperature, it was combined with the titanium and zirconium precursors. The resulting solution was then allowed to react under argon for two to three hours at 115°C. The solution was again vacuum distilled to eliminate the by-products. Solvent was then added to achieve the desired molarity. Acetyl acetone (2,4-pentanedione) (22.5% volume) and acetic acid (5% volume) were added as chelating agents. This modification helps to deposit particle-free films but also reduces the shelf life of the solution. Thus, the modifiers were added just prior to use. Solutions prepared had a Zr/Ti ratio of 52/48 and a molarity of 0.75 and 0.375.

Film deposition from solution involved spin-casting to obtain a uniform thickness followed by two pyrolysis steps at successively higher temperature. Substrates were dehydrated by rapid thermal annealing (RTA) at 700°C for 60 sec just prior to deposition. The solution was dispensed onto the substrate using a syringe through a 0.1μm filter, and spun at 3000 rpm for 45 seconds on a photoresist spinner. On a hotplate, two anneals were performed for a minute each at 300°C and 500°C to evaporate the solvent and expel the organics. RTA was performed at 700°C for 60 seconds in a Heat Pulse 610 (AG Associates) to densify and crystallize the film. The RTA took ten seconds to reach temperature, and about eight minutes to cool to 400°C, at which point the sample was removed and cooled quickly to room temperature. Use of RTA minimizes formation of the non-ferroelectric pyrochlore phase. This procedure yielded about 150 nm/layer for the 0.75M solution, and about 75nm/layer for the 0.375M solution. The spinning and annealing steps were repeated to obtain the desired film thickness.

3.3.2 Zirconia films processing

Zirconia was deposited by the sol-gel method described in the previous section using zirconium propoxide as the precursor and 2MOE as the solvent.[11] The precursor and the solvent were mixed and reacted in a rotating flask for two to three hours at 115°C under argon. Under vacuum, the by-products and some of the solvent were evaporated. (10-15min). The modifiers acetic acid (23%) and acetyl acetone (9%) were then added. The solution was used immediately after preparation because with these modifications the shelf-life is only about a day. After spinning, the film was pyrolyzed at 300°C and 500°C each for one minute on a hot plate. The film was then RTA at 700°C for one-minute. A 0.4 M solution spun at 3000 rpm yielded approximately 75nm/layer. Four layers (300nm) of ZrO_2 were always used to prevent cracking and pyrochlore formation in the subsequent PZT. After the final RTA, a one to three hour furnace anneal at 700°C was performed to densify the zirconia film.

3.3.3 PZT & Zirconia films characterization

The thickness of the PZT films was measured using a surface profilometer (Tencor Inc.), an interference microscope (Zygo Corp.), and a scanning electron microscope (Hitachi S-4100). Test samples were prepared by spinning PZT on platinum coated silicon wafers (150nm Pt, 20nm Ti, 1 μm SiO_2) purchased from Nova Electronic Materials. After deposition, the PZT films must first be masked and etched to introduce a discrete step the same height as the film. An adhesive tape can be used as a quick method of masking, although lithographic patterning with photoresist yields better results. The PZT was etched in dilute hydrofluoric acid and the residue was removed in dilute hydrochloric acid. The bottom platinum electrode serves as an etch-stop. The mask was removed and the step height measured with the profilometer or interference microscope. A reflective coating, such as an electrode, was required when using the interference microscope and transparent films. Additionally, the thickness of the films was evaluated using a SEM by cleaving a sample and observing the cross-section, or observing the film stack profile after ion milling. Figure 3.16 shows a SEM cross section image of PZT deposited on ZrO_2. The sharp interface between the Si_xN_y, ZrO_2, and PZT indicates that the zirconia is an adequate barrier layer preventing Pb diffusion and reaction. The columnar structure of the films is evident. PZT films spun at 1500 rpm yielded 0.2 μm/layer while spinning at 3000 rpm reduced the thickness to 0.15μm/layer.

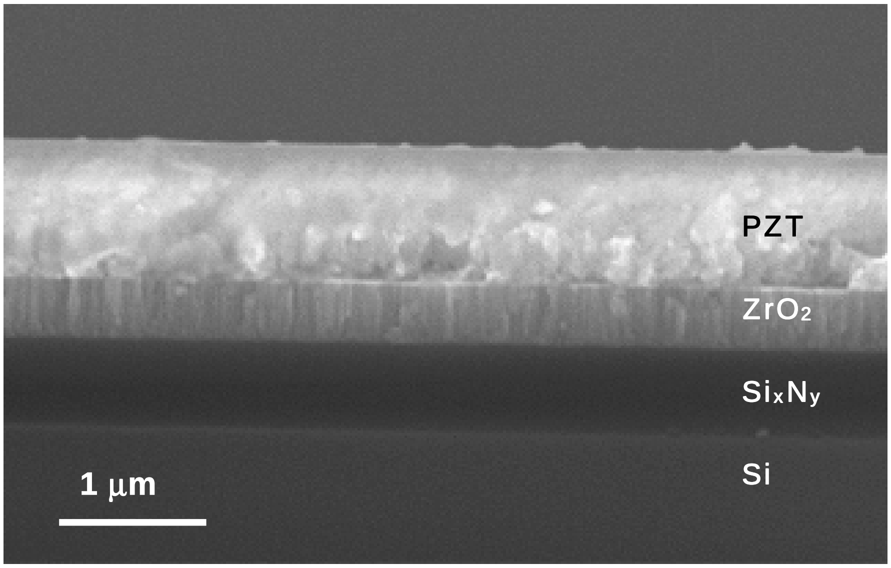

Figure 3.16 SEM image showing PZT deposited on ZrO_2, and the microstructure of the films.

The microstructure and crystal orientation of the deposited films were analyzed using x-ray diffraction and scanning electron microscopy. This is important since the dielectric, piezoelectric, and ferroelectric properties are affected by the microstructure. Figure 3.17a shows an XRD pattern for as-deposited sol-gel zirconia on an oxidized silicon wafer and after a 2hr anneal at 700°C.[12] The absence of a strong peak indicates low crystallinity. Figure 3.17b shows an x-ray diffraction pattern for PZT deposited on annealed sol-gel zirconia. It can be seen that the PZT film is well crystallized into the perovskite phase with the absence of any pyrochlore phase. The (110) peak exhibits maximum intensity, suggesting that the crystallites in the film are approximately randomly oriented – which is expected since the zirconia is mostly amorphous.

For electrical characterization, Pt or Cr/Au circular electrodes were sputtered as a top electrode through a shadow mask on the test samples. To test the PZT films deposited on zirconia, Cr/Au interdigitated electrodes prepared by the methods discussed in section 3.2.4 were used. The dielectric properties of the PZT films were evaluated using an impedance analyzer (4192A Hewlett-Packard). The capacitance and dielectric loss were measured at frequencies from 1kHz up to 100kHz with a 500 mV oscillating voltage. The ferroelectric behavior of the PZT films was characterized using a commercial test

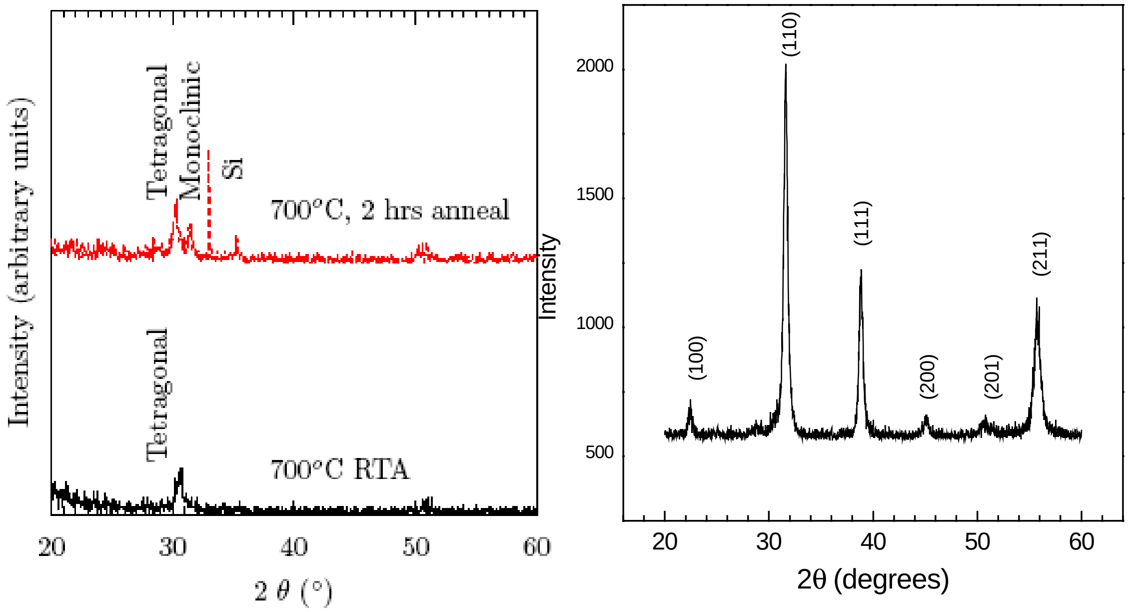

Figure 3.17 X-ray diffraction patterns of (a) sol-gel zirconia[12] (b) PZT on zirconia

instrument (RT66A Radiant Technologies). The piezoelectric properties were not measured in this work. Values for the coefficients are taken from previous studies that used films prepared and deposited in a similar manner.[13]

3.4 Ion-beam etching

Ion-beam etching, or milling, was investigated and successfully adopted as a method to delineate the multi-layered film stack. The etch process offers several advantages over wet etching and other plasma based techniques. The etch rates for the materials comprising the stack were measured under various conditions, and useful process parameters established. Photoresist and metal masks was studied and the pertinent issues are presented. The affect of the ion etching process on the electrical characteristics of ferroelectric PZT films is discussed and experimental data is provided.

3.4.1 Ion-beam etching of thin films

The faithful patterning of the film required etching the diverse materials that comprised the stacks. PZT can be wet etched by solutions containing hydrofluoric acid (HF). The reaction produces insoluble metal fluoride byproducts that are removed with HCl either during the etching or as a separate step.[2] Due to the fast etch rate, 120 nm/min in 10:1 buffered oxide etch, this approach can be used to pattern thick (~7 μm) PZT films with a 2:1 undercut.[14] HF was observed to attack the interface between photoresist and PZT resulting in damage to the PZT as shown in figure 3.8. Platinum can be wet etched in aqua regia ($HCl:HNO_3$), but the rate is slow (16 nm /min) and the acid solution attacks PZT.[15] Since no zirconia etchants were known, various acidic and basic solutions were tested.[16] The zirconia either did not etch at all, the etchant attacked the interface between the zirconia and substrate, or the etchant attacked the grain boundaries of the zirconia and the film cracked and peeled off. In any case, no suitable etching solution was found for zirconia. A general problem with isotropic wet etching is the undercutting of other films and of the mask. Plasma based processes increase the anisotropy of the etch and can avoid this problem. RIE of ferroelectric films, including PZT, with various chemistries has been demonstrated.[17,18] RIE of platinum, however, is difficult because the fluoride and chloride byproducts are not highly volatile.[19] Due to the difficulties with wet chemical etching and RIE, ion-beam etching was explored as alternative.

Ion-beam etching is a purely physical, plasma based etch process. During milling, the sputtering of material occurs by momentum transfer between the impinging ions and the surface. To first order, the etch rate V, is proportional to the product of the ion flux density, F, and the sputter yield, S(θ), and can be expressed by equation 3.2.[20]

$$V(\theta, IE) \propto F\cos(\theta) \quad S(\theta, IE) \tag{3.2}$$

The sputter yield is a function of the angle of incidence, θ, the target material, and the atomic weight and energy of the ions used. Most materials exhibit an increase in sputter yield with θ, up to a maximum at about 40° to 60°, followed by a sharp drop. The overall increase in etch rate for oblique angles of incidence is because the increased sputter yield generally exceeds the reduction in flux density. The sputter yield also varies with ion energy, IE, exhibiting an exponential increase between 20 and 100eV, followed by a linear increase up to about 500eV, and finally increasing more gradually up to a saturation point above 10 keV.[20]

The process is highly anisotropic so undercutting is generally not a concern, and very high resolutions, 100 Å, have been demonstrated.[21] There is no chemical component to the etch, unless one is intentionally added, so there is no attack of the mask or interface, as was observed with HF, and there are no residues to remove afterwards. The physical nature of the process means that all materials can be etched, allowing a single-step approach for patterning multi-material film stacks. However, the major drawback of ion milling is the poor selectivity, and there is typically less than a 10-fold difference in etch rate between materials. The etch-depth is therefore controlled by timing, or with the aid of an end-point detection system, rather than an etch-stop layer.

An Oxford series 300 dual-source etch and deposition system with a 15 cm diameter Kaufman type ion source was used for the milling. The etch rates for the various films, used in the devices were measured at various conditions and are summarized in Table 3.3. All tests were performed using argon at a pressure of 0.2 to 0.3 mtorr. The data confirms that the etch rate for PZT increases linearly with beam current. All the materials tested except Pt exhibited an increased etch rate with angle from 0° to 45°.

In the fabrication of the devices, milling was performed with argon ions at a pressure of 0.2 to 0.3 mtorr, 1000 V, currents of 0.45 mA/cm^2 (80mA). The platen was kept at an angle of 45° to the beam, and rotated during the process. The oblique angle was used to increase the etch rate as well as to avoid trenching and redeposition.[22] Although the neutralizer was not used, large non-uniformity across the samples was not observed. Due to the thick polysilicon sacrificial layer, over-etching was used to insure the complete removal of the zirconia, and so end-point detection was not required. Although the silicon nitride could have been etched by milling, along with the PZT and zirconia, RIE was used simply as a way to insure that all the zirconia had been removed. Occasionally, additional milling was required.

Table 3.3 Ion-beam etch rates and parameters for various materials.

	Beam current (mA)	Current density (mA/cm^2)	Voltage (volts)	Angle*	Etch rate (nm/min)
PZT	80	0.45	1000	45°	24
PZT	88	0.50	1000	45°	26
PZT	106	0.60	1000	45°	31
PZT	75	0.42	1000	0°	14
PZT	106	0.60	1500	55°	30
platinum	80	0.45	1000	45°	34
platinum	75	0.42	1000	0°	30
platinum	106	0.60	1000	0°	38
Si_XN_y	106	0.60	1000	0°	15
Si_XN_y	106	0.60	1000	45°	38
Si_XN_y	80	0.45	1000	45°	28
zirconia	106	0.60	1000	0°	16
zirconia	80	0.45	1000	45°	20

* Measured off-normal to surface being etched

Conditions: 0.2 – 0.3 mtorr argon, neutralizer off

3.4.2 Ion-beam etching of ferroelectric films

It is known that energetic ion-bombardment, as used in ion-milling, can degrade the properties of ferroelectric films.[23] A series of experiments was performed to evaluate the effect of ion-beam etching on the ferroelectric and dielectric properties of the PZT films. Samples were prepared by spinning 2 μm PZT films on Pt/SiO_2/Si substrates. Circular platinum top electrodes were sputter deposited on one of the samples using a shadow mask and the polarization versus electric field was measured (figure 3.18a). The remanent polarization (P_r) and coercive field (E_c) were measured to be 24 μC/cm^2 and 30 kV/cm respectively. To investigate the worst case scenario, samples without top Pt electrodes or any other masking material were ion-beam etched for 15 minutes with a beam current of 0.45 mA/cm^2 and energies of one keV. The background pressure was 2x10^{-4} torr and the samples were held at 45 degrees to the beam while rotating. After etching, electrodes were sputtered on to the film, and the ferroelectric characteristics for these samples were measured (figure 3.18b). The hysteresis loop is considerably distorted and a shift in the coercive field is observed in the etched samples. This shift is caused by an internal field E_i whose magnitude is given by the equation below.[24]

$$E_i = \frac{|E_{c+}| - |E_{c-}|}{2} \tag{3.3}$$

The samples possess an E_i of 4 kV/cm before etching, which increases to 84 kV/cm after the etch process. The etched samples with electrodes were then annealed at 450°C for fifteen minutes in an oxygen and nitrogen ambient (figure 3.18c). After the annealing process the E_i is reduced to 8 kV/cm, demonstrating recovery of the material. The shift in the hysteresis has been previously reported. Lee observed that the effect was a result of space charge trapping at domain boundaries caused by sputter deposition of the Pt electrode and RIE.[25] The internal field of the original sample in our study however, was small (4 kV/cm). Others have related the imprinting by thermal energy to the creation of defect dipole complexes involving oxygen vacancies.[26] The ion bombardment may also create vacancies and defect dipoles resulting in an internal field. Annealing increases the mobility of the displaced charges allowing the vacancies to be filled and restoring the original loop.

During normal etching, a masking material is used to protect the film. A test was conducted to investigate photoresist as a mask during the ion-beam etching of PZT. Samples were prepared by spinning 0.8 μm of PZT on Pt/SiO_2/Si substrates and sputter depositing Pt top electrodes through a shadow mask. Positive photoresist (Shipley 1827) was spun on at 4000 rpm (2.7 μm) and baked at 155°C for 10 min. The samples were then exposed to an ion bombardment of 0.45 mA/cm^2 and energies of 1100 eV for 30, 45, 60, 75, and 90 minutes. The hard-baked resist was removed with an oxygen plasma RIE for 60 min at 25 watts (100V). The samples were then annealed at 600°C for five

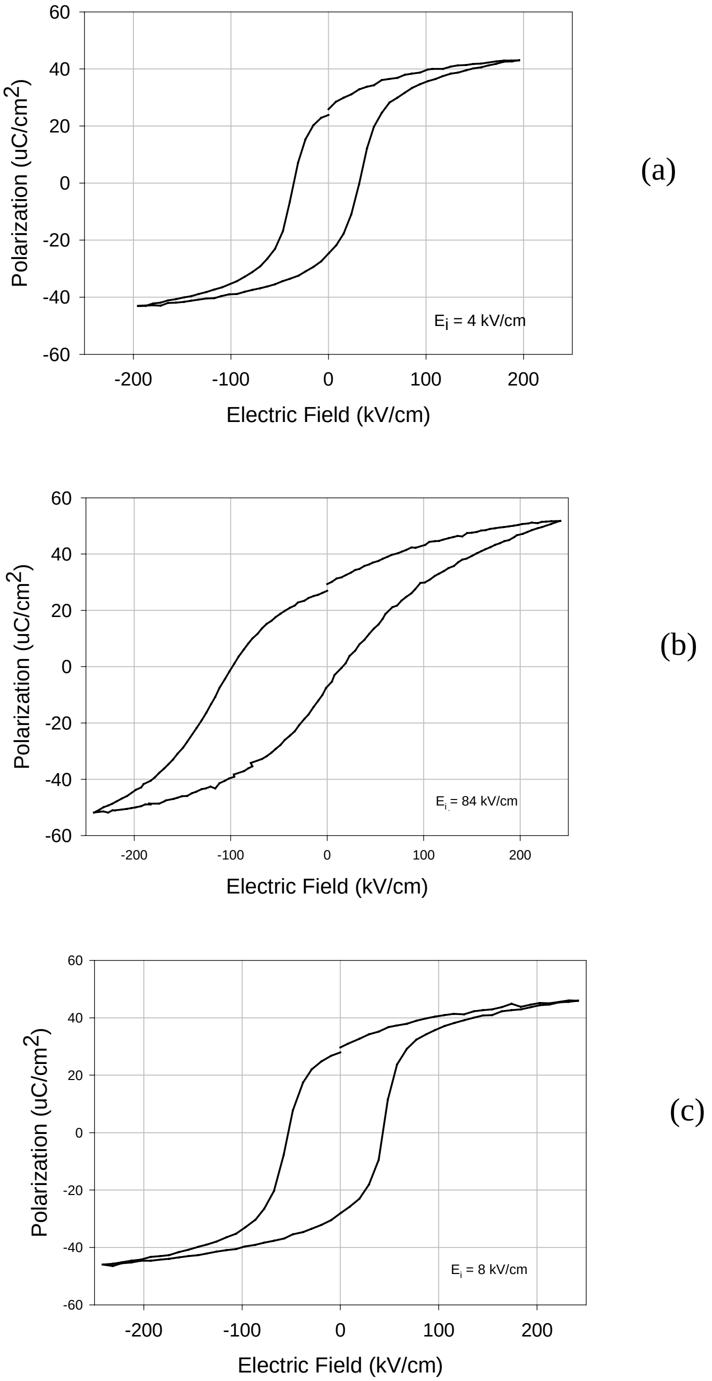

Figure 3.18 Polarization loops for PZT exposed to ion bombardment. (a) The pre-etch hysteresis loop. (b) Degradation of ferroelectric properties due to ion-induced damage. (c) Recovery after annealing.[16]

minutes. There was little change in the ferroelectric behavior of the film at all doses, indicating that the photoresist serves as an effective barrier to the energetic ions. Figure 3.19 shows the dielectric constant as a function of dose, before and after etching, and after annealing the samples at 600°C for 5 min. Although there is a small decrease in the permittivity after etching, the value is fully recovered after annealing. There was no change in the E_i. Since the decrease in permittivity appears to be independent of milling time, it was presumed that the effect originated from the oxygen plasma process. To test this hypothesis the samples were exposed to the RIE plasma for an additional 30 and 60 minutes. No significant change was observed in the induced polarization, coercive field or permittivity. Since there was no loop-shift, the decrease in permittivity may be a result of poling by the self-bias and heating during either etch process, and a saturation may have been reached such that additional etching did not alter the value further. It is difficult to determine from these experiments alone the origin of the decrease.

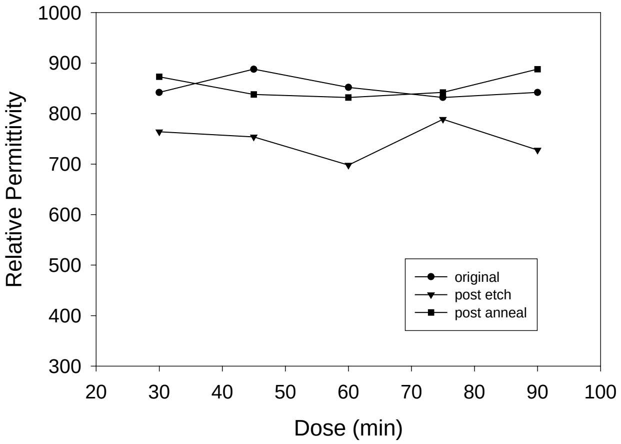

Figure 3.19 Affect of ion dose on the permittivity of photoresist masked PZT.

3.4.3 Hard masks

Two masks were investigated and employed in the fabrication of the devices. The first, out of simplicity, was Shipley’s 1827 photoresist spun at 3000 to 4000 rpm (2.5-3.0 μm), developed in a dilute sodium hydroxide solution and hard baked at 155°C for 10 minutes. Baking at temperatures below this would result in bubbles in the resist during the milling, causing large unwanted pitting in the PZT. Although the thermocouple on the etch system indicated a temperature of 70°C, temperature labels placed directly on the samples and on the substrate holder revealed that the true temperature exceeded 170°C. This was due to the poor heat transfer between the sample holder, and the water-cooled holder assembly. Exceeding the glass transition temperature at 118°C, caused the resist to flow, changing dimensions and becoming thinner at the edges as shown in figure 3.20. The loss of fidelity and thinning of the resist at the edges resulted in poor resolution (~3 μm), as shown in figure 3.21a. After milling, the resist hardened due to cross-linking and could not be removed by acetone nor resist stripper. Since a clean surface was required for good IDE, oxygen plasma for one to two hours was required to fully remove the residue shown in figure 3.21b. It was clearly evident that an alternative mask was required.

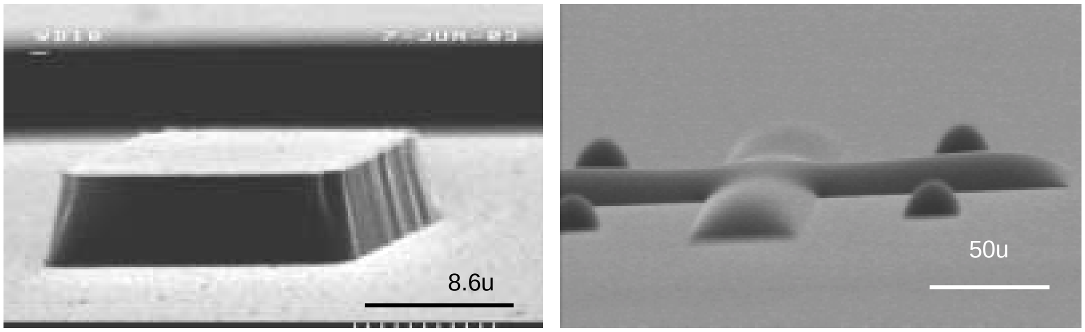

(a) (b)

Figure 3.20 Flowing of photoresist. Profile (a) after developing and (b) after 10 min at 160°C.

The addition of a partial pressure of oxygen during ion-beam etching has been noticed to reduce the sputter yield of certain metals which oxidize easily. [27] Figure 3.22 shows the etch rate as a function of oxygen concentration for various materials. The effect is likely the result of competition at the surface between the chemisorbtion of oxygen, and the sputtering removal of both the oxygen and metal atoms. This method can be used as a means to increase the selectivity of a mask over non-reactive materials, such as noble metals or oxides. To investigate this, chromium, titanium and aluminum were chosen as possible masking materials. It was assumed that the etch rate of PZT, zirconia, and platinum did not change appreciably by the addition of oxygen. The integration of such a masking approach with PZT required a couple of issues to be resolved. The hard masks had to be patterned and removed without damaging the PZT. Also, the minimum mask thickness to protect the PZT from radiation damage had to be ascertained for each mask material.

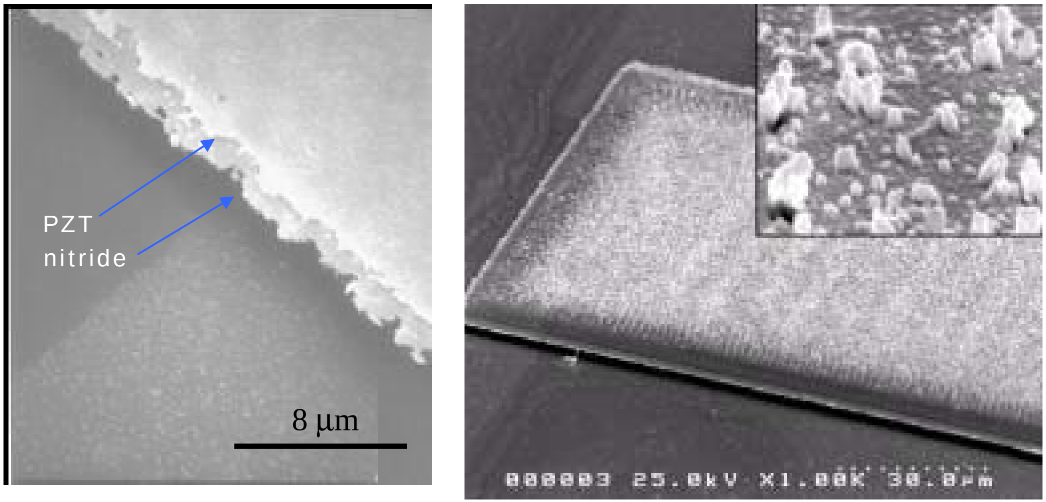

(a) (b)

Figure 3.21 (a) Edge showing poor resolution as a result of flowing and erosion of the photoresist mask during ion milling. (b) Photoresist residue on device surface after 45 min of oxygen plasma.

Table 3.4 provides the measured etch rates for the metal masks and PZT in 2:1 oxygen to argon ambient. The highest oxygen concentration possible was chosen to maximize the effect, however figure 3.22 indicates that lower partial pressures is adequate. If was found that the etch rate of the PZT did not change significantly and a selectivity of about three was found for all three metals over PZT. This is not surprising since PZT is a radiation-hard oxide with a relatively low etch rate.

The minimum mask thickness necessary to prevent damage to the PZT was simulated and analyzed. The software package, Stopping and Range of Ions in Matter (SRIM), was used to calculated the projected range and straggle for 1000 eV Ar ions incident on Cr and Ti at an angle of 45°. The results are provided in Table 3.4 and a graphic illustration of the ion penetration into chromium is shown in figure 3.23. It can be seen that 100 Å of Cr or Ti would be sufficient in stopping most ions. The simulation does not include channeling effects, but uncertainty in the etch rates dictated use of a margin of safety of more than 100Å.

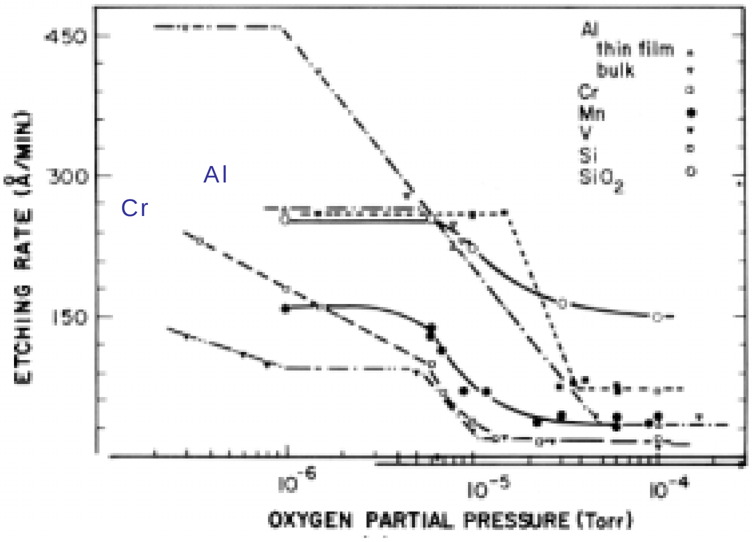

Figure 3.22 Etch rate of various materials with the addition of oxygen.[27]

Table 3.4 Ion-beam etch rates for mask materials in oxygen ambient.

	Deposition	Etch rate [1] w/O_2 (nm/min)	Etch rate [2] no O_2 (nm/min)	Projected range &(straggle)(Å)[3]	Selectivity over PZT [2]
PZT	Sol-gel	26	26	n/a	n/a
Chromium	Sputtered	7	20-40	12 (7)	3.5
Titanium	Sputtered	9	20	18(11)	3.0
Aluminum	Sputtered	9	45-75	n/a	2.8

[1] Conditions: 0.4 mtorr, 2:1 O_2:Ar, neutralizer off, ∠45°, 88mA, neutralizer off

[2] Source:22

[3] Simulated using SRIM ©

PZT (1.6 μm) was deposited on a platinized Si wafer, and samples were sputter coated with Cr, Ti, and Al masks. The dielectric and ferroelectric properties of the virgin PZT were measured. The chromium was patterned and removed with an acid based etchant of ceric ammonium nitrate, nitric acid, and water (1g:5ml:25ml). This solution was found to etch sputtered Cr at a rate of about 65nm/min. This solution, at the concentration used, has been observed to be compatible with PZT. The titanium was patterned and removed by CF_4 and Ar RIE. The aluminum mask was patterned in-situ during photoresist development with dilute NaOH. Surprisingly, the PZT peeled off the platinum. This is odd because PZT on platinized Si was routinely immersed in developer without any such adverse effects. TMAH based developer had the same effect so the Al mask was not pursued further. Samples with Cr and Ti, patterned and non-patterned masks, were ion-milled for about 20 minutes. After the etch the masks were removed and Pt circular electrodes were sputter deposited through a shadow mask to measure the properties of the PZT.

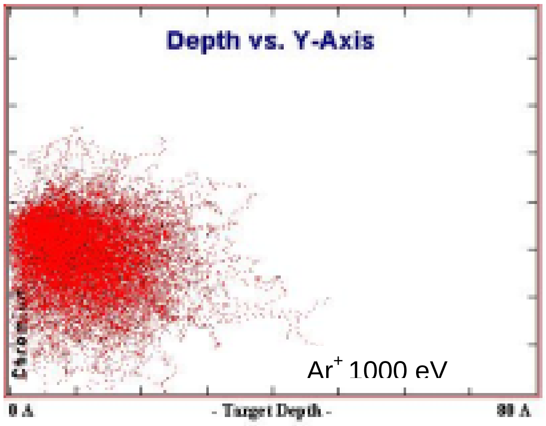

Figure 3.23 Simulated penetration of argon ions in chromium using SRIM©

Figure 3.24 shows the improved resolution and near vertical profile of the ion-beam etched PZT using the Cr mask and Ti masks. If the resolution is taken as a conservative 1/10 μm, then the improvement over resist masks is 30 fold. The edge profile is also a function of the milling angle. Figure 3.25 shows 1.5 μm lines patterned in PZT using Cr masks. Although the lines on the photolithographic mask were 3 μm wide, the width of the Cr mask can be controlled by wet etching, and thinner lines are possible. The dielectric and ferroelectric properties of the samples were measured after milling and

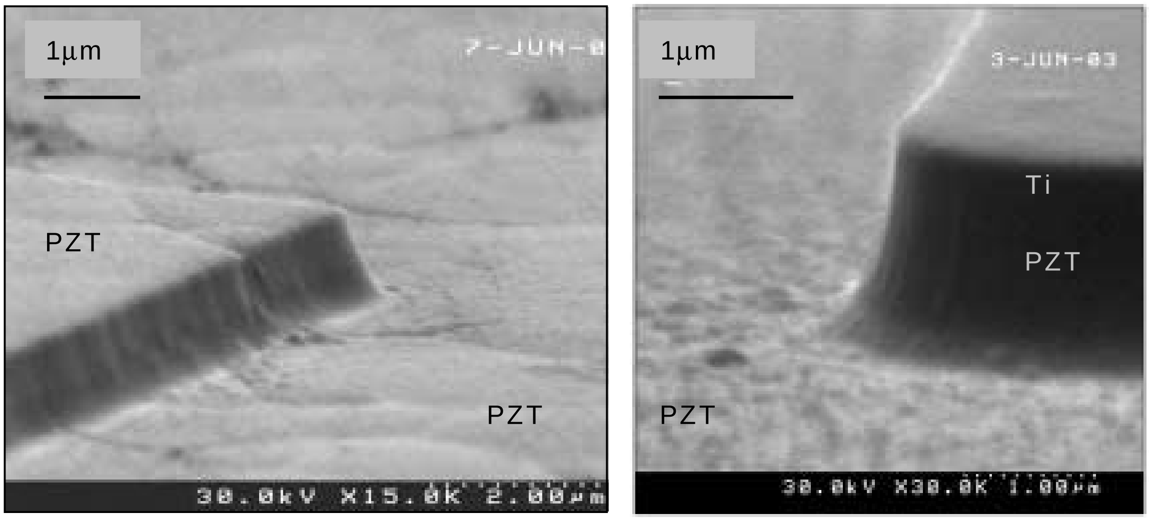

Figure 3.24 Ion-beam etching PZT with hard masks in O_2, showing excellent resolution. (a) PZT patterned with chromium mask. (b) Profile of PZT patterned with titanium

compared with those of the original sample. No significant difference was noticed. There was a small decrease in the permittivity of the Ti masked sample, but this was probably due to the RIE process used to pattern and remove the Ti mask. For this reason and the higher selectivity, Cr masks were selected for the fabrication of devices. Figure 3.26 shows the P-E loop measured after milling and removing the Cr mask.

Chromium masks were successfully used to pattern flat unimorph and bimorph micro-actuators. Difficulty however was encountered wet etching the Cr masks deposited directly on platinum. As was noticed with the wet etching of the Cr adhesion layer of the IDEs, the lateral etch rate was increased by several orders of magnitude. Again, likely due to a galvanic effect, the patterning of the Cr masks on bimorph samples in an electrolytic solution proved difficult. Therefore, the Cr mask was electrically isolated form the platinum by introducing a thin CrO_x (~100nm) layer by adding oxygen during the first 10 min of deposition. The ion-beam etching was adjusted for this added layer. From a fabrication perspective, the hard masking was superior to photoresist. Although an additional deposition step is required, there are numerous advantages to using the hard masks. Removal of the Cr mask required only a 10-15 min wet etch, with no RIE-induced damage. In addition, there was less concern over the integrity of the mask if additional

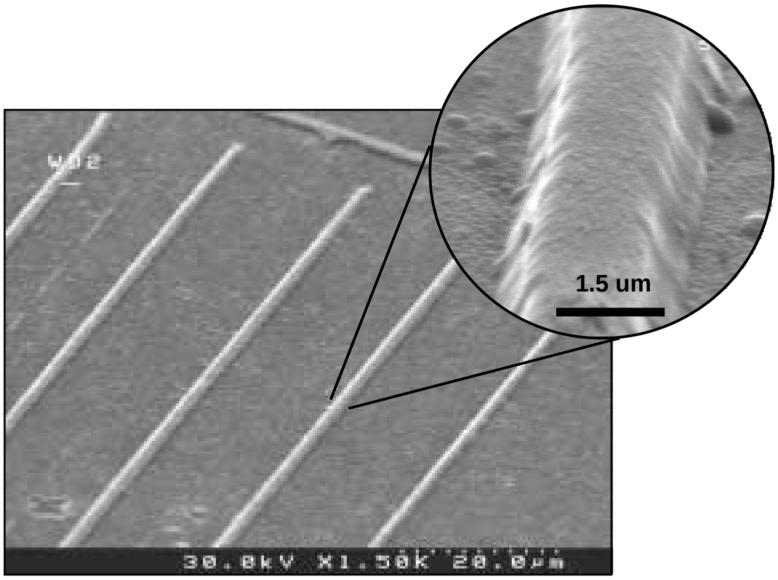

Figure 3.25 Fine lines patterned in PZT by ion-beam etching using chromium masks.

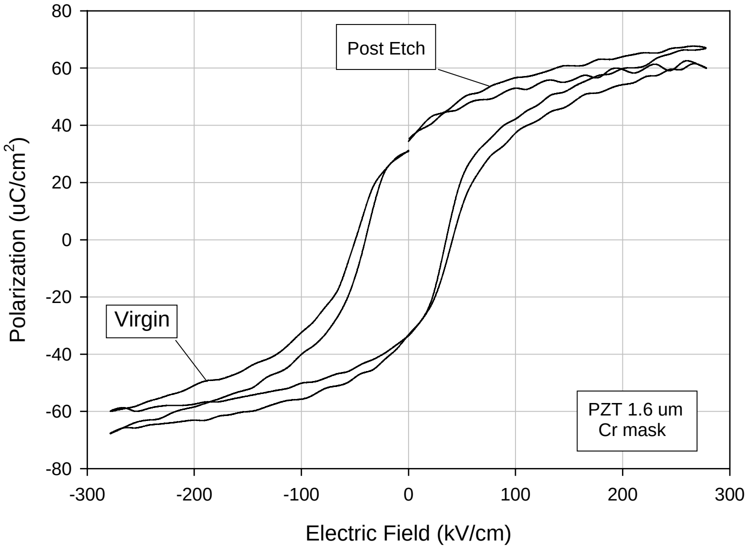

Figure 3.26 P-E loop of PZT protected with Cr mask during ion-beam etching. Cr mask removed.

milling is required. The addition of oxygen improves the selectivity and makes the technique a more robust fabrication process. Since the hard masks do not erode at the edges the way the photoresist did, both the critical dimension and the aspect ratio are greatly improved. All these factors conclude that chromium hard masks with oxygen are a viable solution for patterning ferroelectric PZT films and multi-material stacks.

3.5 Conclusions

The fabrication sequence was presented along with the critical issues pertinent to each processing step. The sacrificial polysilicon and silicon nitride were deposited by LPCVD. The zirconia and PZT layers were deposited by a sol-gel method. A combination of ion-beam etching and reactive ion etching was used to pattern the microactuators. The gold transmission lines were sputter deposited and patterned using wet and dry etching. The IDE were sputter-deposited and patterned using a bilayer lift-off approach. The structures were released in a dry xenon difluoride etch that eliminated any stiction related losses greatly improving actuator yeild. Hard masking with oxygen was developed for ion milling to replace photoresist masks. The resist masks yielded poor resolution and were difficult to remove completely due to cross-linking. The hard masking technique was shown to be compatible with PZT. The hard masks also demonstrated greater resolution, improved aspect ratios, and easy removal.

References

---

[1] J.R. LaRoche, R. Ren, J.R. Lothian, J. Hong, S.J. Pearton, E. Lambers, "The use of amorphous SiO and SiO_2 to passivate AuGe-based contact for GaAs integrated circuits," Elect. Chem. Solid-State Let., 2(8), pp.395, 1999.

[2] S.E. Trolier, "Use of photolithography and chemical etching in the preparation of miniature piezoelectric devices from lead zirconate titanate (PZT) ceramics," M.S. Thesis, The Pennsylvania State University, 1987.

[3] M. Madou, Fundamentals of Microfabrication, CRC press, 1997.

[4] N.H. Tea, V. Milanovic, S. Zincke, J. Suehle, M. Gaitan, M. Zaghloul, J. Geist, "Hybrid postprocessing etching for CMOS-compatible MEMS," J. MEMS, 6(4), pp. 363-371 1997.

[5] I.W.T. Chan, K.B. Brown, R. Lawson, A. Robinson, Y. Ma, D. Strembicke, "Gas phase pulse etching of silicon for MEMS with xenon difluoride," Proc. IEEE Canadian Conf. Elec. Comp. Eng., Alberta, pp. 1637-1642, 1999.

[6] H.F. Winters, J. W. Coburn, "The etching of silicon with XeF_2 vapor," App. Phys. Lett. 34(1), pp. 70-73, 1979.

[7] G.T.Kovacs, N.Maluf, K.E. Petersen, "Bulk micromachining of silicon," Proceedings of the IEEE, 86(8), pp. 1536 – 1551, August, 1998.

[8] Berkeley lab manual chapter 7.15, http://microlab.eecs.berkeley.edu/labmanual/chap7/7.15.html

[9] P.B. Chu, J.T. Chen, R. Yeh, G. Lin, J.C.P.Huang, B.A.Warneke, K.S.J. Pister, "Controlled Pulse-Etching with Xenon Difluoride," IEEE Inter. Conf. Transducers'97, pp. 665-668, 1997.

---

[10] K.D. Budd, S.K. Dey, D.A. Payne, “Sol-gel processing of $PbTiO_3$, $PbZrO_3$, PZT, and PLZT thin films,” Brit. Ceram. Proc., 36, pp.107, 1985.

[11] B. Xu, Y. Ye, L.E.Cross, J.J. Bernstein, R.Miller, “Dielectric and hysteresis from transverse electric fields in lead zirconate titanate thin films,” Applied Physics Letters 74, pp. 3549, 1999.

[12] E. Hong, Surface micromachined peristaltic pumps using lead zirconate titanate film, Ph.D. thesis, The Pennsylvania State University, 2004.

[13] R. A. Wolf, S. Trolier-McKinstry, “Temperature dependence of the piezoelectric response in lead zirconate titanate films,” J. Appl. Phys. 95(3), pp. 1397, 2004.

[14] L.-P. Wang, “Microelectromechanical Systems (MEMS) sensors based on lead zirconate titanate (PZT) films,” Ph.D. Thesis, The Pennsylvania State University, 2001.

[15] P. Walker, W. Tarn, *Handbook of metal etchants*, CRC, 2000.

[16] S.J. Gross, Q.Q. Zhang, S. Tadigadapa, S. Trolier-McKinstry, T.N. Jackson, F. Djuth, “Reliable integration of piezoelectric lead zirconate titanate with MEMS fabrication processes,” SPIE 4558, pp.72-80, 2001.

[17] R.J. Zeto, B.J. Rod, M.Dubey, M.H. Ervin, R.C. Piekarz, S.Trolier-McKinstry, T.Su, J.F. Shepard, “High-Resolution Dry Etch Patterning of PZT for Piezoelectric MEMS Devices,” IEEE, pp. 89-92, 1998.

[18] W. Pan, C.L. Thio, S.B. Desu, “Reactive ion etching damage to the electrical properties of ferroelectric thin films,” J. of materials research, 13(2), pp. 362-367, 1998.

---

[19] G.E. Menk, S.B. Desu, W. Pan, D.P. Vijay, “Dry etching issues in the integration of ferroelectric thin film capacitors,” MRS symposium proceedings, 433, pp. 189-200, 1996.

[20] R.E. Lee, ‘Ion-beam Etching (Milling)’, Chapter 11 in “VLSI electronics: microstructure science” vol.8, Academic Press, 1984.

[21] A.N. Broers, W.W. Molzen, J.J. Cumno, N.D. Wittels, “Electron-beam fabrication of 80-Å metal structures,” Appl. Phys. Lett. 29, pp.596, 1976.

[22] C.M. Melliar-Smith, “Ion etching for pattern delineation,” J. Vac. Sci. Technology. 13(5) Sept/Oct, pp. 1008-1022, 1976.

[23] C. Soyer, E. Cattan, D. Remiens, “Ion beam etching of lead-zirconate-titanate thin films: Correlation between etching parameters and electrical properties evolution,” J. of Appl. Phys., 92(2), pp. 1048, 2002.

[24] C.W. Chung, C.J. Kim, “Etching effects on ferroelectric capacitors with multilayered electrodes,” Jpn. J. Appl. Phys. 36, pp. 2747-2753,1997.

[25] J.K. Lee, T.-Y. Kim, I. Chung, S. B. Desu, “Characterization and elimination of dry etching damage layer in Pt/Pb($Zr_{0.53}Ti_{0.47}$)O_3/Pt ferroelectric capacitor, Appl. Phys. Lett., 75(3), pp. 334-336, 1999.

[26] W.L. Warren, D. Dimos, G.E. Pike, B.A. Tuttle, M.V. Raymond, “Voltage shifts and imprints in ferroelectric capacitors,” Appl. Phys. Lett., 67, pp. 257-266, 1995.

[27] M. Cantagrel, M. Marchal, “Argon ion etching in a reactive gas,” J. of Materials Science, 8, pp. 1711-1716, 1973.

Chapter 4

Cantilever Curvature and Residual Stress

An understanding of the residual stresses present in almost all deposited films is of paramount importance in microsystems, especially in freestanding multi-layer structures. Released structures can warp, leading to a loss in yield, resonance frequencies may shift, and the electrical characteristics may degrade if stresses are not controlled.[1] In addition, the dielectric and piezoelectric properties of PZT films are affected by the residual stress.[2] Stresses are generally categorized as arising from intrinsic (growth, impurities, lattice mismatch, phase transition) and extrinsic (thermal expansion, non-uniform plastic deformation) sources.[3]

4.1 Cantilever curvature

Understanding and balancing the residual stresses in the cantilevers has been the greatest challenge of this work. Figure 4.1 shows the catastrophic effects of large and unbalanced stresses, and the resulting out of plane deflection of the released cantilevers. Control of the curvature, and therefore the tip deflection and gap spacing, is an essential requirement for producing functioning switches. Controlling the distance between the contact and transmission lines is important because it affects the turn-on voltage and switching speed of the devices. Too large a gap will result in nonfunctioning switches.

4.1.1 Stress-induced curvature

A quantitative analysis based on beam theory was undertaken to understand the relationship between residual stresses in the films and cantilever curvature. The same technique, discussed in chapter two, that was employed to calculate the quasi-static tip deflection and blocking force, was also applied to the stress analysis. Using beam theory, the field-induced stress was replaced by the residual stress in the deposited films. With simplifying assumptions, such as one-dimensional stress along the length of the cantilever, no gradients in the films, and no external loading, a condition of zero curvature for discrete films can be obtained by equation 4.1, where t,y,σ are the

$$\sum_{i=1}^{n} t_i \sigma_i y_i = \sum_{j=1}^{m} t_1 \sigma_j y_j \tag{4.1}$$

thickness, residual stress and distance from the neutral plane respectively. The indices n and m represent the number of films above and below the neutral plane. The equation reveals an intuitive relationship; for zero deflection, the net force above and below the neutral plane must balance. Achieving this condition however requires accurate knowledge or control of the parameters. This presents a problem since the residual stress,

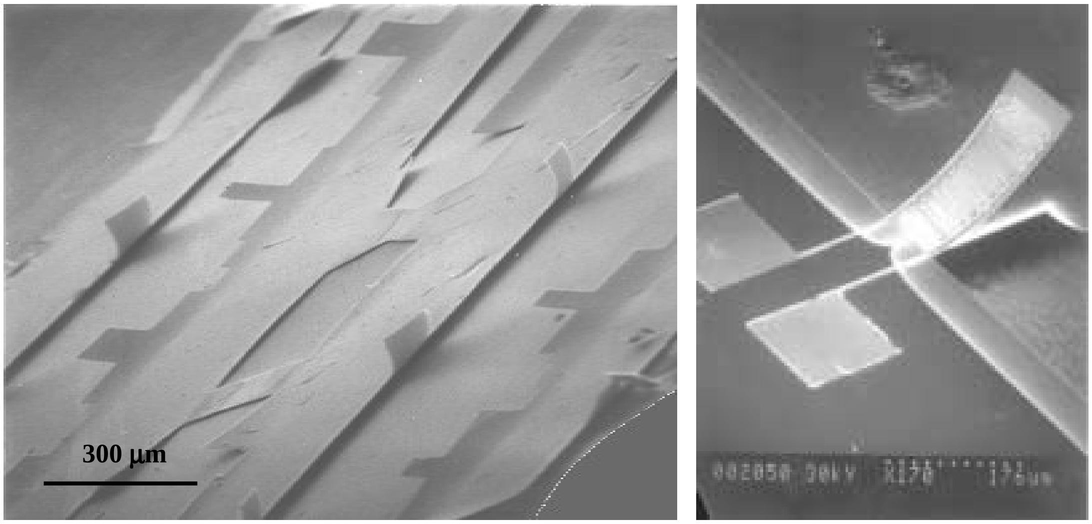

(a) (b)

Figure 4.1 Out of plane bending resulting from unbalanced residual stresses in films. (a) Various cantilevers on a die, (b) and a single device.

and stress gradient, of a film may not be known and are difficult to measure accurately. In addition, there is always uncertainty in the thickness of the films. Calculating the location of the neutral plane requires knowledge of the elastic moduli of the films, which are also difficult to ascertain.

As an example, the deflection of a simple two-layer cantilever was calculated for various lengths as a function of the residual stress difference between the two films. The results, and the equation used in the calculation, are shown in figure 4.2. In the equation, t is the total thickness of the beam and L is the length. The elastic moduli (200 GPa) and the thickness of the two films (0.5 μm) are equal, so the neutral plane lies at the interface and mid-plane of the structure. For the longest device, 280 μm, a difference in stress of less than about 12 MPa is required to keep the contact from rising more than 5 μm. Since the intended gap is 2 μm, and the residual stresses of the films are on the order of 100 to 300 MPa, it is evident that achieving flat cantilevers is not a trivial task.

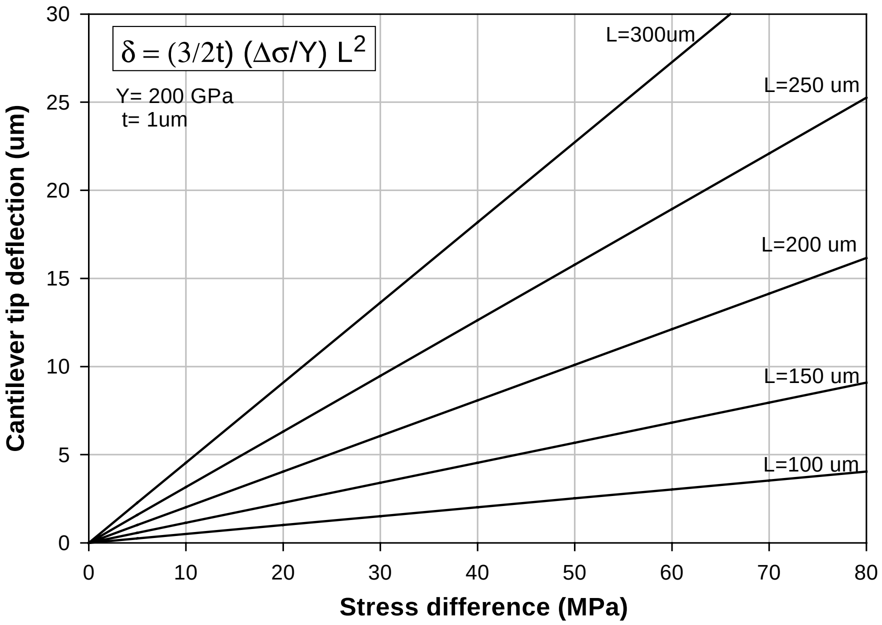

Figure 4.2 Bi-layer cantilever tip deflection resulting from a residual stress difference between two films of equal thickness.

4.1.2 Curvature measurement

The curvature of released cantilevers was measured using a New View 100 white light interference microscope (Zygo Corp.). The instrument measures the height of features by vertically scanning the objective, using a piezoelectric transducer, to generate a series of interferograms. Using Fourier analysis, ranges of phases are calculated for each wavelength. The phase information uniquely defines the height for each pixel and a 3-dimensional image is generated based on this data. The company claims a resolution of 0.1 nm in the vertical direction and 1.5 μm (10X) in the horizontal direction. The accuracy of the instrument was confirmed against a standard prior to use, and by observing the variance of a series of measurements. Since poling the PZT reorients the domain states, curvature measurements made after release were performed on unpoled samples.

4.1.3 Fabrication methodology

A systematic approach was therefore devised to obtain flat cantilevers without complete and precise knowledge of the parameters. The method involved producing a set of test samples in which all parameters were kept constant except one that was varied. The PZT thickness was chosen as the variable parameter, due to the relative ease of control. Varying the stress or thicknesses of the other layers would have proven more difficult. The thickness of the PZT was varied by the number layers deposited and by the concentration of the solution.

Listed in Table 4.1 is a summary of selected fabrication runs and the samples produced using the methodology. A somewhat arbitrary scale is used to classify the curvature of the cantilevers as flat, small, medium, or large, and is provided at the end of the table. The curvature measured and listed was prior to poling. All samples in the first run (BSXL) yielded flat structures. However, micro-cracks discovered in the PZT and zirconia probably allowed for stress relief, leading to the low curvature on all samples.

Actuation did not lead to any significant deflection, corroborating this assumption. The second run provided support for the approach by yielding flat cantilevers. A near linear relation between PZT thickness and curvature was also observed (figure 4.3). With the success of this batch, attention was focused on the fabrication of switches – believing that the stress issue had been resolved. Runs three and four were able to replicate the previous results and produce the first working switches, as well as devices delivered to the project sponsors. Only cantilevers classified as either 'flat' or 'small' produced functioning switches.

Table 4.1 Single-parameter methodology results.

Run	Sample	layers	PZT thickness	condition†	comments
1	BS2L	2	272 nm	flat	cracks in PZT/ zirconia
	BS4L	4	544 nm	flat	cracks in PZT/ zirconia
	BS6L	6	816 nm	flat	cracks in PZT/ zirconia
	BS8L	8	1088 nm	flat	cracks in PZT/ zirconia
2	BPTO2	2	272 nm	flat	
	BPTO4	4	544 nm	up -med	
	BPTO6	6	816 nm	N/A	zirconia not removed
	BPTO8	8	1088 nm	up- large	
3	W1RSL	6	450 nm	up - med	non –functioning switches
	W2Q1	3	225 nm	flat	first functioning switches
4	W2Q2	5	375 nm	up -small	switches sent to army
	W2Q4	5	315 nm	up - small	
5	CANQ2-2	2	150 nm	up - med	first Cr mask
	CANQ2-3	3	225 nm	up - med	first Cr mask
	CANQ2-4	4	300 nm	up - med	first Cr mask
	CANQ2-5	5	375 nm	up - med	first Cr mask
	CANQ2-6	6	450 nm	up - med	first Cr mask
6	Nitanl	2	300 nm	flat	Cr mask, test no IDE
	NS2-3	3	450 nm	up - small	Cr mask, test no IDE

† For length ≥200 μm: deflection ≤ 5μm flat, ≤ 10μm small, ≤ 25μm med, >25μm large

The approach was validated by several runs and there seemed to be consistency in the results. PZT thicknesses below 300 nm yielded flat devices, and the curvature increased with PZT thickness. A simple model was proposed to describe the measured switching characteristics. To accurately validate the model required the actuation characteristics of the unimorph cantilevers, such as the deflection and contact force as a function of the applied field. This data could not be extracted from the switches due to the small gap. Fabricating unimorph actuators directly on the silicon substrate, without the polysilicon layer, resulted in a large cavity (>60 µm) below the actuators, allowing ample space for deflection. The next set of samples, CANQ2, was produced for this purpose. Surprisingly, none of the dies yielded flat actuators, and all samples had roughly the same curvature. These results not only cast doubt upon the methodology, but also on the stress mechanisms involved. Initially it was suspected that the chrome mask, used for the first time, was a factor. It was also hypothesized that the polysilicon may have acted as a stress relief layer, and its absence was altering the stress of the other films. Another batch of unimorphs on SC-Si was produced (run 6) and the results were more consistent with the previous runs. This indicated that the chromium masks could be used successfully and that the polysilicon sacrificial layer was not a critical component.

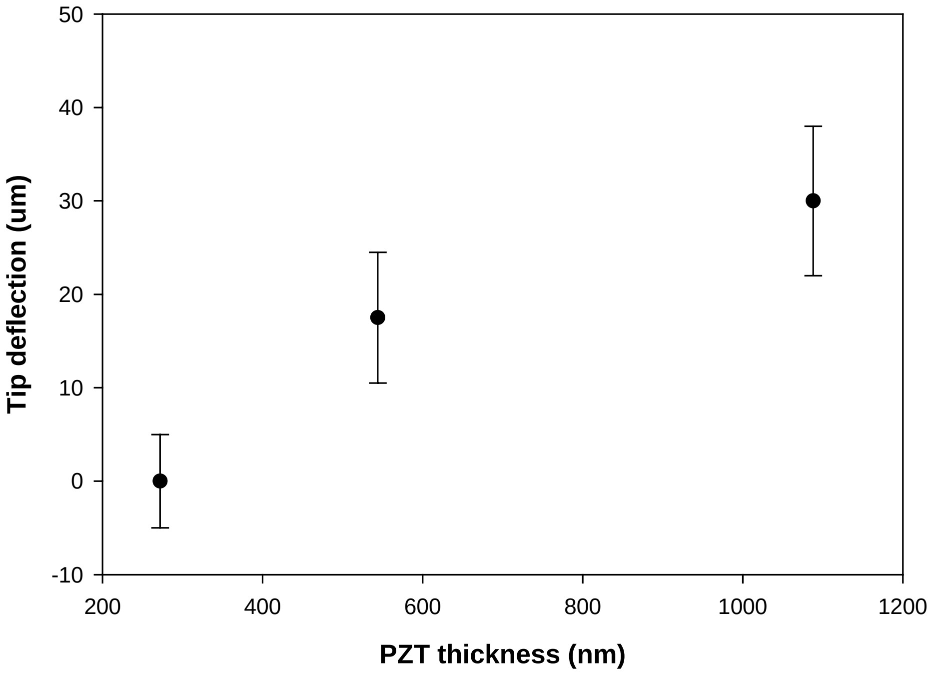

Figure 4.3 Cantilever deflection (curvature) as a function of PZT thickenss for actuators 230 µm and 280 µm.

It was later realized, that altering the thickness of a single layer changed the location of the neutral plane and therefore the y_i parameters. Nonetheless, the ‘single – parameter’ method was an invaluable tool because it allowed the fabrication of flat unimorph actuators and switches without a precise knowledge of the residual stress of each layer nor a full understanding of the stress mechanisms. The approach also highlighted that additional stress-effects were likely involved.

4.1.3 Thermal effects

It was observed that exposure of released devices to elevated temperatures resulted in an upward change in curvature. An investigation was undertaken to quantify this effect and the results are summarized in Table 4.2. The tip deflection of ten cantilevers, from a single die was measured using the interference microscope. The die was placed on a hot plate and the temperature was ramped up to 100°C, held for 1.5 hours, and allowed to cool to room temperature. The tip deflection of each device was again measured and compared against the pre-anneal value. The samples were not poled in either case. The increase in tip deflection ranged from 1 to 3 μm for all cantilevers. The top four rows of Table 4.2 provide the length of the cantilever (x) and the deflection (y) data of four select devices. The experiment was repeated by annealing at 300°C for 10 min. The next four rows of Table 4.1 summarize these results. In this case, the 'x' value specified is the lateral measurement distance. As can be seen, there is a more significant change in curvature upon annealing at a higher temperature even though the anneal time was reduced. To observe if this change was permanent, the deflection of the same devices was

Table 4.2 Cantilever curvature change with annealing.

device#	temp.	Virgin (μm)		Post –anneal (μm)		24 hrs	
		x	y	x	y	x	y
1	100°C	230 †	18	230 †	19	n/a	n/a
8	100°C	280	23	280	26	n/a	n/a
19	100°C	180	16	180	17	n/a	n/a
14	100°C	180	13	180	15	n/a	n/a
3	300°C	215	3	215	15	183	15
23	300°C	229	6	233	16	194	15
8	300°C	279	7	262	19	260	19
26	300°C	221	2	227	17	196	15

† design length of cantilever.

measure after about 24 hours and the value is listed in the last column of the table. Although the deflection on two of the devices seems to have decreased, the measurement length is also reduced. This investigation indicates that the curvature of the devices is very sensitive to temperature. The lack of a spontaneous reduction in curvature after annealing precludes thermal expansion as an explanation, and it appears that the process is irreversible, or very slow.

Additional information related to this effect was obtained by another set of experiments. After dicing a sample, there was concern that processing had degraded the properties of the PZT. Half of the dies were annealed at 400°C for 20 min, prior to release, to restore their piezoelectric response. After release, the curvature of various devices on each die was measured and compared. Table 4.3 shows the deflection of six cantilevers that are representative of all devices. For comparison, devices of similar length were chosen and listed consecutively. As can be clearly seen, the deflection of the annealed devices is greater than the non-annealed devices. This was true for all cantilever of comparable length. This behavior suggests that annealing, prior to or after release, altered the residual stress of one or more of the films.

Table 4.3 Curvature change with pre-release anneal .

die#	device#	annealed	Deflection (μm)	
			x	y
5	6	not annealed	245	6
12	26	400°C	245	19
7	32	not annealed	130	3.2
14	17	400°C	137	8
7	3	not annealed	280	6.8
15	28	400°C	280	31

4.2 Residual stresses and stress mechanisms

It was evident based on the results of the ‘single-parameter’ method, the observed thermal effects, and on numerical models, that a better understanding of the residual stresses, or stress mechanisms in the structure was required. A more thorough investigation was therefore conducted to help devise a more reliable fabrication methodology for producing flat structures. The details of the study, the quantitative results, and an analysis are presented in this section.

4.2.1 Measurement method

The evaluation of film stress was made by the wafer curvature method. The curvature of a circular substrate is measured before and after film deposition, removal, or annealing. The average residual stress, σ, of the film is calculated using Stoney's equation given below.[4]

$$\sigma_f = \frac{Y}{(1-\nu)} \frac{t_s^2}{6t_f} \left(\frac{1}{R_f} - \frac{1}{R_i}\right) \tag{4.2}$$

t_f and t_s are the thicknesses of the film and substrate, R_f and R_i are the final and initial radii of curvature, and Y and ν are the elastic modulus and Poisson's ratio of the substrate respectively. The quantity $Y/(1-\nu)$ is known as the biaxial modulus and for silicon (100) is 180 GPa.[5] Implicit in the above equation is that the film is thin compared with the thickness of the substrate, and stress gradients in the films are assumed negligible. A benefit of this method is that the calculation of the stress does not require knowledge of the mechanical properties of the film. Those of the substrate are needed and since the properties of single-crystal silicon (SC-Si) are well characterized, these wafers make excellent test substrates. The critical assumption made in the application of this method is that the process performed does not mechanically alter the substrate, or affect any underlying film. This makes the measurement of multi-layer films, such as PZT on an electrode stack, difficult and care must be taken in the interpretation of the results.

All curvature measurements were made at room temperature using 4" <100> silicon wafers on a Tencor FLX-2320 dual wavelength commercial system. The instrument calculates the radius of curvature of the substrate by scanning across the surface and measuring the position of a reflected laser beam. Since the stress calculation is sensitive to uncertainties in t_s, the thickness of each wafer was carefully measured at three points along the radius using a micrometer. For each wafer, the curvature was measured along four diameters, 45° apart.

4.2.2 Stress measurements

The first film in the structure is the barrier silicon oxide grown by the thermal oxidation of the polysilicon or SC-Si. The residual stress of the polysilicon sacrificial layer was not measured. As a visual aid, the stack for a unimorph actuator is shown in figure 4.4. To measure the stress in the oxide, a silicon wafer was wet thermally oxidized (960 Å) at 1000°C. Due to viscous flow at this temperature, the SiO_2 grows in a stress-free state and the only contribution to the residual stress is thermal.[6] The stress was calculated at –390 MPa (compressive) which is in the range given in the literature.

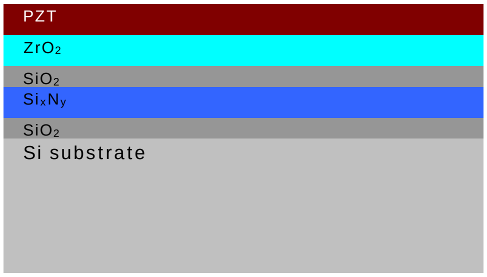

Figure 4.4 Unimorph actuator film stack

To measure the residual stress of the silicon nitride films, the curvature of the wafers was measured prior to, and after removing the nitride. The front side of the wafers was coated with photoresist, and the backside nitride was removed by reactive-ion etching. Two wafers were used for this measurement; nitride on 640Å of thermal oxide, and directly on silicon. The average stress of the nitride was calculated and found to be 467 MPa. Berkeley claimed the previous batch, deposited at similar conditions, to be around 320 MPa. It was critical to empirically confirm that the nitride stress remained constant during thermal treatments, even in an oxidizing environment. To ascertain this, the nitride on oxide wafer was annealed at 840°C for 2hrs in dry, and then 2hrs in wet oxygen. After striping the backside silicon oxide in buffered hydrofluoric acid, the change in curvature detected was within the uncertainty of the measurement. This result indicates that the stress of the Si_xN_y and thermal oxide are stable under thermal treatments in an oxidizing ambient below the nitride deposition temperature of 850°C.

The residual stress of the sputtered silicon oxide adhesion layer was measured by depositing a thin (500Å) layer on two nitride coated wafers and annealing in N_2/O_2 at 750°C for 2.5 hrs. Anneals were performed to simulate the zirconia thermal treatment. After the annealing, a compressive stress was calculated at -232 MPa with no significant change after four one-minute RTA cycles at 700°C. This indicates that further thermal processing does not alter the stress of the sputtered oxide by a large amount.

Zirconium oxide was sol-gel deposited on nitride coated silicon wafers. Six layers were deposited and then annealed at 750°C for 1.5 hrs. The residual stress in the zirconia film for each process step is given in figure 4.5. The error bars denote the high and low measurements, and the point indicates the average of the four. Three days later, the stress was again measured and the wafer was subjected to five RTA cycles at 700°C to simulate

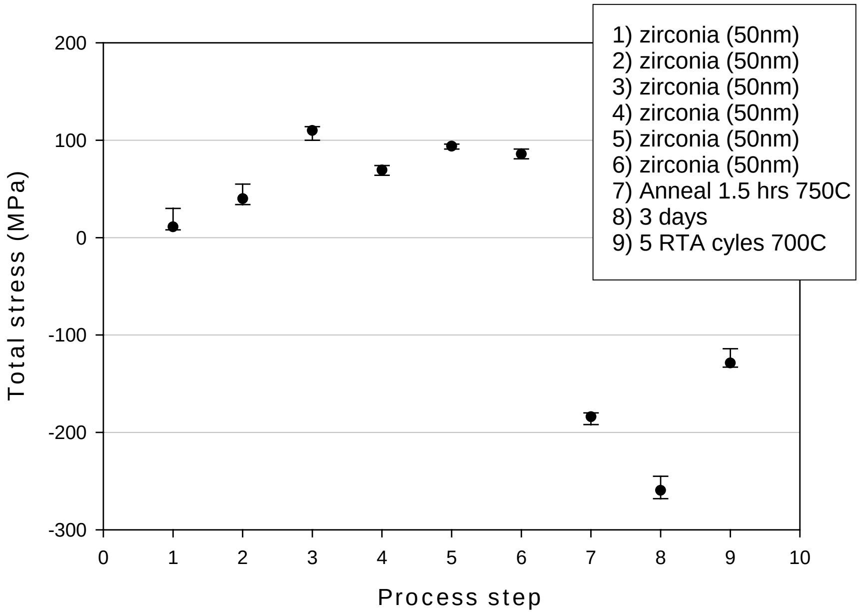

Figure 4.5 Residual stress and aging of sol-gel deposited zirconium oxide films on nitride coated silicon wafer

the PZT anneals. The residual stress of the zirconia film became significantly more compressive during the three days and changed again, becoming less compressive, after annealing.

The stress of the complete stack was investigated by depositing zirconia and PZT on the wafer with sputtered oxide. Figure 4.6 shows the total stress in the stack excluding the silicon nitride after each process step. As in figure 4.5, the zirconia became more compressive after annealing at 700°C for two hours. Four layers of PZT (300 nm) were then deposited and annealed. The stress of the stack was measured after 2.5 hours and again after one, and two days. No significant change in stress was observed. The wafer was then annealed on a hot plate at 390°C for 40 min. Again, no large change in stress was noticed.

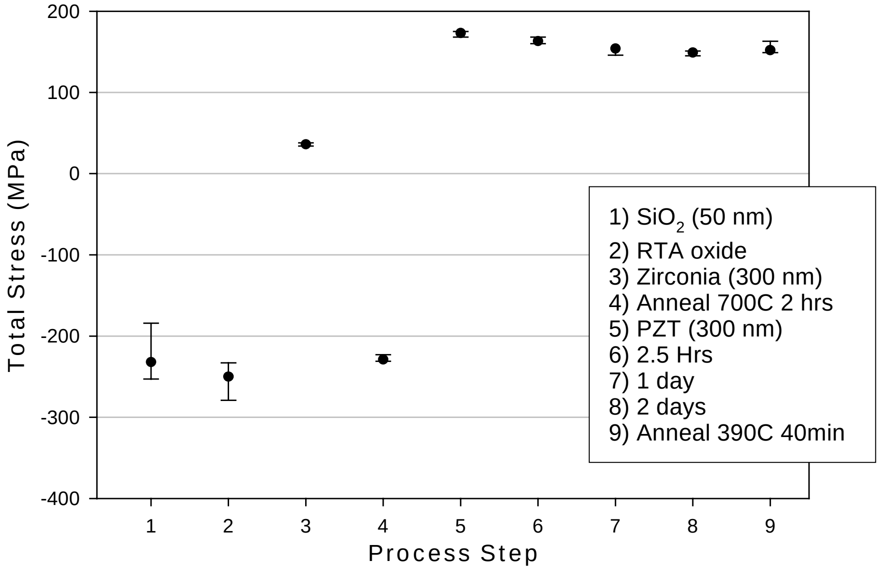

Figure 4.6 Total residual stress in film stack deposited on nitride coated wafer. Stress change with annealing also examined.

Platinum films for bimorph microactuators were deposited using a parallel plate sputter system with heated platen and the process conditions as given in chapter three. Films deposited at room temperature cracked during annealing at 700°C due to the large stresses that developed. It was found that a minimum temperature of 250°C was required during deposition to prevent this. The residual stress of platinum was measured by depositing Ti/Pt (20/200nm) on an oxidized silicon wafer. Neglecting the contribution of the titanium adhesion layer, the stress in the platinum was calculated at 410 MPa. The wafer was then annealed for ten minutes at 700°C and the stress in the platinum increased to 880 MPa.

4.2.3 Film stress analysis and discussion

Stress relaxation or aging of films, such as with the zirconia shown in figure 4.4, has been previously reported. Brenier observed that sol-gel zirconia films annealed at 400°C were porous and adsorbed moisture during exposure to atmosphere.[7] He proposed that like the hydration of SiO_2, Zr-OH species are formed. The repulsion of the OH dipoles in zirconia films introduces a compressive component to the stress. Therefore, the affect of water exposure on the intrinsic component of the stress is influenced by the porosity of the film.[8] The observed logarithmic change in stress with time of similar sol-gel zirconia films annealed at 700°C supports this explanation.[9] Structural changes such as grain growth or migration, offer an alternative or additional mechanism for the aging of films. However, the observed increase in compressive stress during exposure to air is inconsistent with stress–induced diffusion. This mechanism results only in a stress relaxation and never in an increase in the magnitude of the stress as was observed (figure 4.5). In addition, these processes are slow at room temperature and large stress changes appeared to occur in only a few minutes. During annealing at temperatures above 100°C the trapped water desorbs returning the state of the film to the more tensile as-deposited stress state. This was demonstrated with the sol-gel zirconia films. The empirical results discussed, support the hypothesis of the hydration of the zirconia films exposed to moisture. Figure 4.6 indicates that once the PZT has been deposited, encapsulating the zirconia, the total stress of the stack is stable with time and additional thermal treatment. Although possible, it is unlikely that the stress in each film is changing in a manner to result in a net zero change for the complete stack. Therefore, it can be claimed with reasonable confidence that the stress of each individual layer is also constant, and that the PZT acts as good barrier to moisture penetration.

For stress measurements involving multiple films, the stress in a single layer is calculated from the total stress by equation 4.3,

$$\sigma_T t_T = \sum_{i=1}^{n} \sigma_i t_i \tag{4.3}$$

where σ_i and t_i are the stress and thickness for each of the n layers, and σ_T and t_T are the total stress and stack thickness. Again, implicit are the assumptions that inter-diffusion and reactions between the layers are limited. With the values from figure 4.6 the stress of the annealed zirconia is calculated to be –230 MPa which is similar to the value shown figure 4.5 of –190 MPa. As explained above, this value is variable and changes with time and annealing. This makes the calculation of the stress of the PZT film and the zirconia in the stack difficult. The combined stress of these two films is calculated at 160 MPa. Most reports in the literature claim the residual stress of sol-gel derived PZT films to range from 70 - 150 MPa and results mainly due to difference in thermal expansion between the film and the silicon substrate.[10] Some, using XRD to measure the inter-planar spacing, have calculated the stress of PZT to be as high as 250 MPa.[11] If a stress value for the PZT is chosen in the range of 100- 150 MPa, the stress of the zirconia in the stack is calculated as 146 - 219 MPa. The results of the stress study are summarized in Table 4.4.

The thermal component of the residual stress arises from the difference in thermal expansion between the substrate and the film during temperature changes. The thermal stress, σ_{th}, can be calculated using equation 4.4,

$$\sigma_{th} = \frac{Y}{(1-\nu)_f} \int_{Ti}^{T_f} (\alpha_s - \alpha_f)\, dT \tag{4.4}$$

where $Y/(1-\nu)_f$ is the biaxial modulus of the film, T_i and T_f are the initial and final temperatures of the process. The thermal expansion coefficient (TCE) of the substrate, α_s, and the film, α_f, may sometimes vary considerably across a temperature range. This is the case with both silicon and PZT. Listed in Table 4.4 is the calculated thermal stress expected for each film. The values used for the TCE and modulus of the films, were obtained from the literature taking care that the deposition method and conditions were similar to those used in this study. Despite this, there is a wide range in both properties. The porosity of the zirconia increases this uncertainty. Nonetheless some general conclusions can be drawn.

Table 4.4 Measured and calculated stresses of films in the stack.

Film	Process	Deposition Temp.	Expected Stress (MPa)	TCE (ppm/°C)	Modulus[5] (GPa)	Thermal Stress (MPa) [2]
SiO_2	Oxidation	1000°C	-390	0.05	90	-306
SiO_2	Sputter & anneal	700°C	-232	0.05	90	-214
Si_xN_y	LPCVD	850°C	320 - 467	1.6	370 [1]	581
ZrO_2	Sol-gel	700°C	146 – 219 [3]	6.4 – 7.4[4]	220 -280	531- 630
PZT	Sol-gel	700°C	70 – 150 [6]	2.0 – 9.0	70 - 100	100 - 143
Pt	Sputtered	300°C	430	8.8	255	410
Pt	Anneal	700 °C	880	8.8	255	956

1) stoichimetric LPCVD nitride
2) TCE silicon (100) 2.4 – 4.1 ppm/°C (25 – 800 °C)
3) In stack based on PZT value
4) Y stabilized zirconia
5) Biaxial modulus
6) From literature

The value of the measured stress of the thermally grown silicon oxide is close to the calculated thermal stress. As supposed, viscous flow at 1000°C may result in solely a thermal component to the residual stress of the silicon oxide. The calculated thermal stress of the silicon-rich nitride films seems to indicate that there exists an intrinsic compressive stress. Studies have shown the total stress of the nitride at a given temperature to be a function of the SiH_2Cl_2/NH_3 gas ratio.[12] The large difference between the calculated thermal stress of the zirconia and the measured valued, indicates a large intrinsic component to the total residual stress. Figure 3.17 shows that, although mostly amorphous, some monoclinic phase was formed during the annealing step. It is known that a phase change from tetragonal/cubic to monoclinic is accompanied by a volume increase of 4%.[13] Shown in figure 4.7 is the temperature dependence of the TCE for bulk PZT for both the poled and unpoled conditions.[14] An average value was used in the calculation. The result of the calculation confirms that most of the residual stress in sol-gel-deposited PZT on silicon substrates is thermal in origin. It appears that most of the platinum stress, both as-deposited and annealed, is also thermal.

As mentioned previously, the residual stress of each of the films in the stack was found to be stable during annealing. The stress of the zirconia however was shown to vary with thermal processing when exposed to atmosphere and not encapsulated by the PZT. Tests also showed that the curvature of the cantilevers increased when annealed before or after release, and that the change was permanent on the time scales measured. Patterning the devices by ion-beam etching, exposed the zirconia at the edges. This exposed surface is small, 170 μm^2 even for the longest device. It is likely, that high temperature processing that occur after the stack is etched, and the zirconia is exposed, dehydrate the film causing a change in stress and curvature. The elevated temperature is the driving force for expelling the water and explains the observed cantilever deflections with annealing. The reverse process, the re-hydration of the entire zirconia layer through the small surface area, may be very slow at room temperature. The stress in the zirconia did not return to the original value and therefore, the cantilevers remained permanently deformed. The fabrication runs revealed that thin (300nm) PZT was optimum for flat cantilevers (Table 4.1). Based on the explanation above, the flat cantilevers with thin PZT may have been a result of a shorter ion-beam etch time and a reduced thermal budget. Regardless of the exact mechanism, the experiments and fabrication results indicate that films that are not

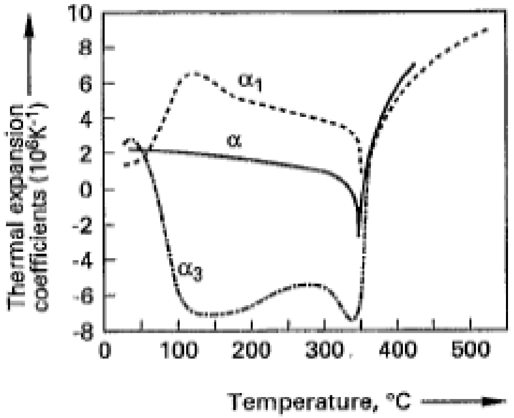

Figure 4.7 Coefficient of thermal expansion of bulk PZT with Nb_2O_5 1%. α unpoled, and α_1, α_3 poled.[14]

stress-stable, such as this sol-gel zirconia, are not suitable for free-standing MEMS structures.

4.3 Alternative structures

Two alternative structures for cantilever actuators were investigated in order to overcome the two problems discussed in the previous sections. The first problem was the difficulty in consistently balancing the stresses to produce flat devices. The uncertainty in the measured residual stresses substantiated the difficulty. The second problem was the instability in the stress of the sol-gel zirconium oxide buffer layer with temperature. This resulted in devices that were very sensitive to thermal processing.

4.3.1 Titania buffer layers

As discussed in the previous section, experiments suggested that the stress instability and the cantilever curvature were due to hydration and dehydration of the zirconia films. The supposed porous nature of the films is likely a result of the sol-gel deposition process. The expelling of the organics during pyrolysis creates voids that partially collapse during higher temperature annealing. Therefore, an alternative to sol-gel deposition was sought. It is known that void reduction can be achieved by the bombardment of the growing film during sputter deposition. The momentum transfer between the high energy ions and the surface results in forward sputtering into the voids, and a higher surface mobility due to impacts and local heating.[3] A zirconium target was not readily available to deposit ZrO_2, but a titanium target was. Therefore, sputtered titanium oxide was investigated as a possible alternative to sol-gel zirconia. Well-crystallized PZT without pyrochlore phase has been reported on titania barrier layers deposited by pulsed laser ablation on silicon substrates.[15] Due to the electrode configuration, the ferroelectric properties were not known.

Titania films 30 nm thick were reactively sputtered deposited with Ar and 1% O_2 on a silicon nitride and oxide-coated 4” silicon wafer. Three layers of PZT (450 nm) were spun on two test samples. The titania on one sample was annealed at 700°C for one hour while the other was as-deposited. The titania anneal was performed to insure the full oxidation of the film, and to confirm the integrity of the film at the PZT anneal temperature. The XRD pattern for both samples is shown in figure 4.8. Both patterns indicate that the PZT is crystallized in the perovskite phase with all orientations present. The broader peak at 29° suggests the possibility of the presence of the non-ferroelectric pyrochlore phase. This peak was reduced when the titania was annealed. Since titania was annealed at 700°C it was expected that both the anatase and rutile phases be present.[16] The small peak near 28° could be the [110] peak of the rutile phase.

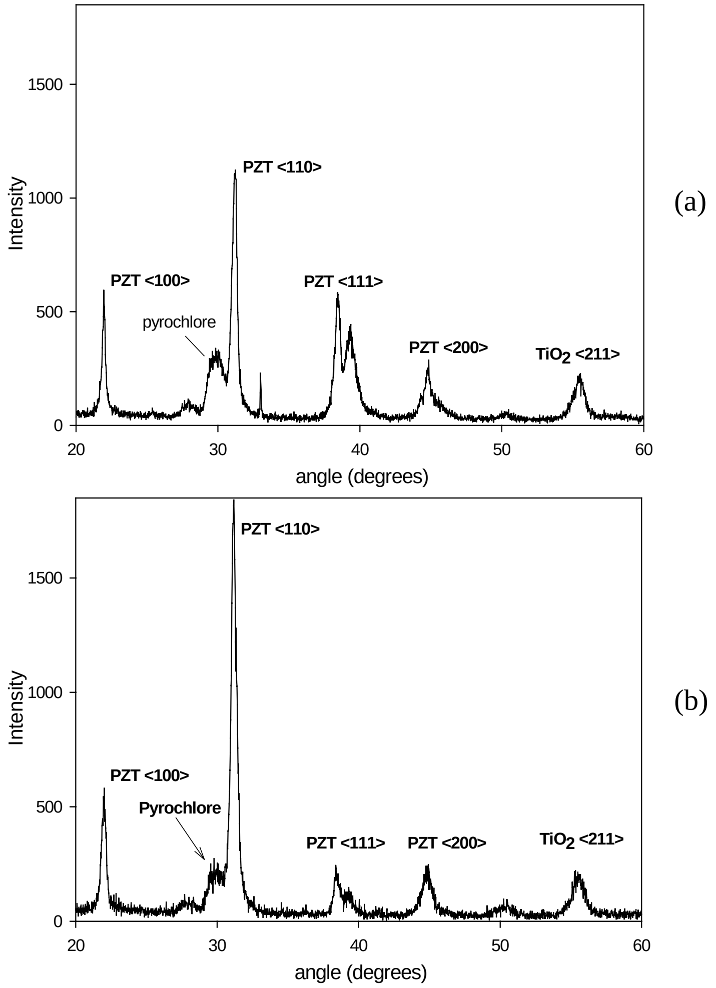

Figure 4.8 XRD pattern of sol-gel PZT (450nm) on reactively sputtered TiO_2 (100nm) (a) as deposited titania (b) titania annealed in air at 700°C for 1 hr.

PZT films, using 2 (300nm), 3 (450 nm), and 4 (600nm) layers, were deposited on titania samples annealed for three hours. Gold IDE electrodes were deposited on each of the test samples and the dielectric and ferroelectric properties were measured. The dielectric properties were measured with a 500 mV oscillation at 1 to 100 kHz. The permittivity was calculated using equation 2.2. Figure 4.9 shows the polarization-hysteresis loops and dielectric data for each sample. The data shows good ferroelectric behavior for all three samples. There is a clear increase in remanent polarization and permittivity with increasing PZT thickness. In addition, the loop becomes less shifted and more rectangular. This trend has been reported for PZT films, 0.25 to 6 μm thick, on platinized wafers.[17] As was suggested, due to the substrate effect, domain wall clamping becomes more severe in thinner films. In addition, the possible dissolution of the titania into the PZT would decrease the Zr/Ti ratio, shifting the composition away from the MPB and reducing the properties. This decrease would be more pronounced for thinner films since this alternate composition would account for more of the total thickness. The loops however did indicate ferroelectric and piezoelectric behavior comparable to that of PZT on zirconia.

The residual stress and stress stability of the sputtered titania films was measured to justify the use in released structures. Titania film was deposited on a 4” wafer under the same conditions listed above, the curvature of the wafer was measured and the stress values are shown in figure 4.10. The measurement indicates that the film posses a residual stress of about 320 MPa, and is stable with annealing and exposure to ambient humidity. Due to these two positive results, unimorph actuators using the titania buffered PZT were fabricated.

Figure 4.11 shows an SEM image of the titania buffered unimorphs after ion beam etching the film stack. All the layers are visible including the thin silicon oxide etch-stop layer. After release, most devices from all samples, with 2,3, and 4 PZT layers, were observed to possess a large upward curvature. Several however were flat or nearly flat. Figure 4.12 shows cracks that developed at the corners on many devices. As corners act

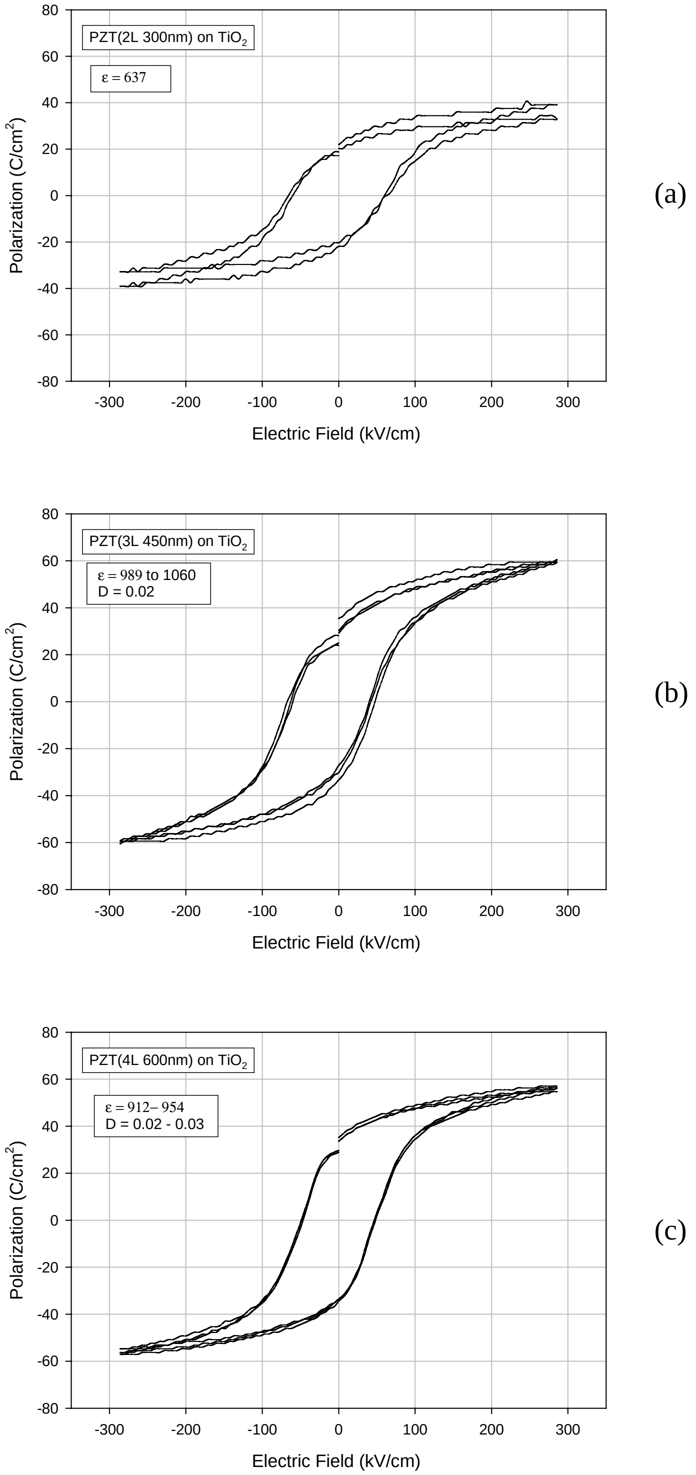

Figure 4.9 Polarization hysteresis curves, permittivity and loss (1 kHz) for PZT on sputtered titania barrier layers. PZT thickness is (a) 300 nm (b) 450 nm (c) 600 nm

as stress concentrators, it is probable that the cracks developed at these points.[18] All devices from the two-layer sample were cracked. As discussed, the large curvature indicates a stress imbalance in the structure. Flat devices with no cracks were observed adjacent to cracked devices and seems to suggest a non-uniform stress distribution. These results indicate that the stress mechanisms of titania buffered unimorphs is not well understood at this time. Devices were packaged, wire bonded and the deflection was measured. The deflection results are presented in chapter five.

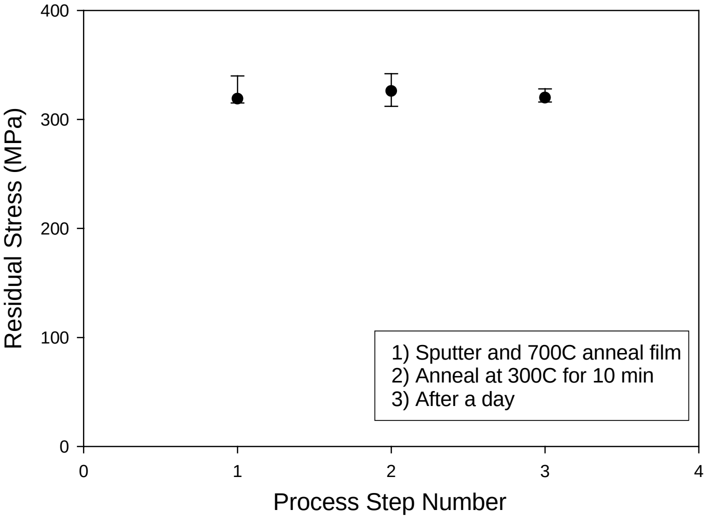

Figure 4.10 Residual stress in sputtered titanium oxide film

4.3.2 Bimorph microactuators

Due to the inherent symmetry of the bimorph structure, residual stresses in the layers are expected to balance, and result in cantilevers with a low curvature. Bimorph microactuators were fabricated in order to investigate this hypothesis and to measure device performance. Figure 4.13a shows a cross-section SEM image of a bimorph film stack after ion-beam etching. Each layer is clearly visible including the silicon oxide barrier layer at the bottom. Figure 4.13b shows the window that was opened by ion-beam etching to contact the middle platinum. The devices fabricated were unimorph actuators with a PZT passive layer because the second window was not opened to contact the bottom platinum electrode. The devices however, were used to verify the approach.

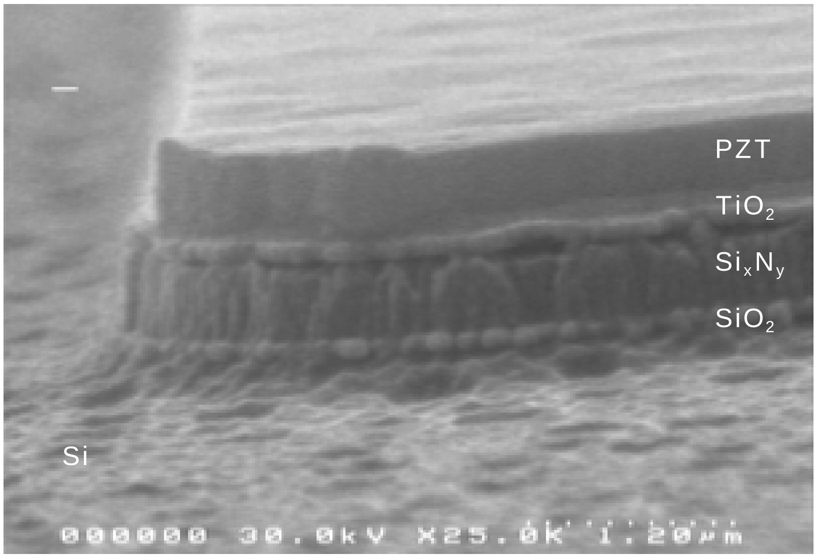

Figure 4.11 SEM image of titania unimorph film stack after ion-beam etching.

After the etch release step in XeF_2, the devices were observed under an SEM to assess the curvature. As can be seen in figure 4.14, there is a significant downward curvature to all the released devices. This was expected because the top platinum layer was deposited at

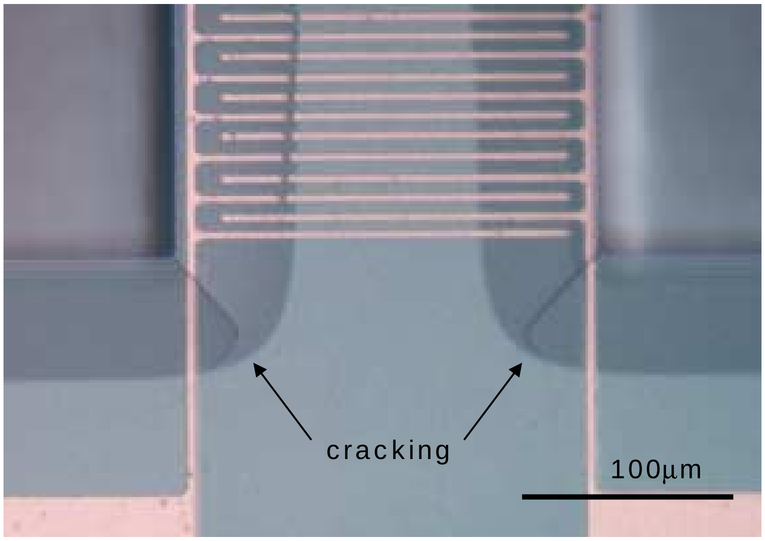

Figure 4.12 Titania buffered unimorphs exhibited cracking at corners of cantilever during release. Shown here, a partially released 200 μm wide device.

300°C, and possessed a measured stress of 430 MPa compared with 880 MPa for the bottom Pt. The stress of the bottom and middle platinum increased during the 700°C PZT crystallization anneals. The stress of the middle platinum layer is not expected to contribute significantly to the curvature since, in principle, it lies on the neutral plane. An anneal performed at 300°C had no affect on the curvature of the bimorphs. The sample was then annealed in a furnace at 590°C for five minutes. As expected, the curvature decreased so that the tip of a 230 μm long cantilever was raised about 30 to 40 μm. Figure 4.15 shows the same sample after an additional five minute anneal at 650°C. The two SEM images clearly show that the devices are flat, or nearly flat, indicating that the top Pt stress has increased and is balancing the bottom Pt stress. The apparent curvature of the corner seen in figure 4.15b is unique, and not an indication of a larger effect. A hot plate anneal at 300°C for ten minutes did not change the curvature, indicating the devices were stable at lower temperatures.

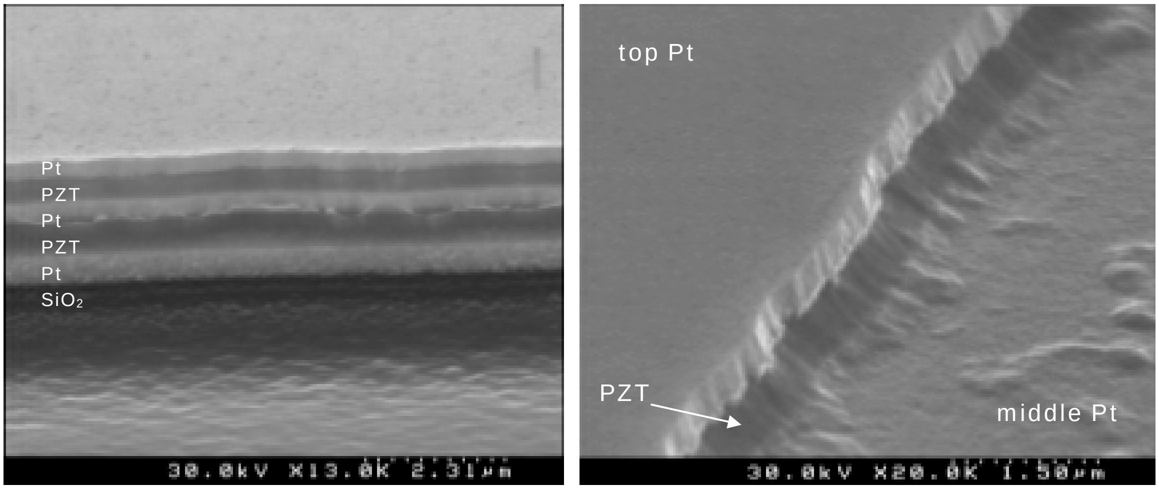

(a) (b)

Figure 4.13 SEM image of bimorph actuator structures. (a) cross-section of stack showing each individual layer. (b) Etched window exposing middle platinum.

The compressive thermal oxide layer below the bottom platinum breaks the desired symmetry of the structure, and imparts an upward curvature. This could explain why an anneal at only 650°C was required instead of 700°C. Despite the slight asymmetry, flat structures were produced because of post-release annealing. With the ‘single-parameter’ method employed with the unimorphs, a series of samples were produced and only one or two were flat enough to yield functioning switches. Cantilevers with excessive curvature could not be recovered. The benefit of the bimorphs is two fold. First, the design symmetry promotes stress balance. There are always however, variations in thickness and material properties due to processing which lessen the symmetry. Second, a series of post-release anneals at successively higher temperature allows a thermal treatment to be tailored for each individual sample. By controlling the residual stress in this manner, the curvature and therefore the tip deflection can be adjusted. In principle, this method could also be applied to unimorph cantilevers if designed properly.

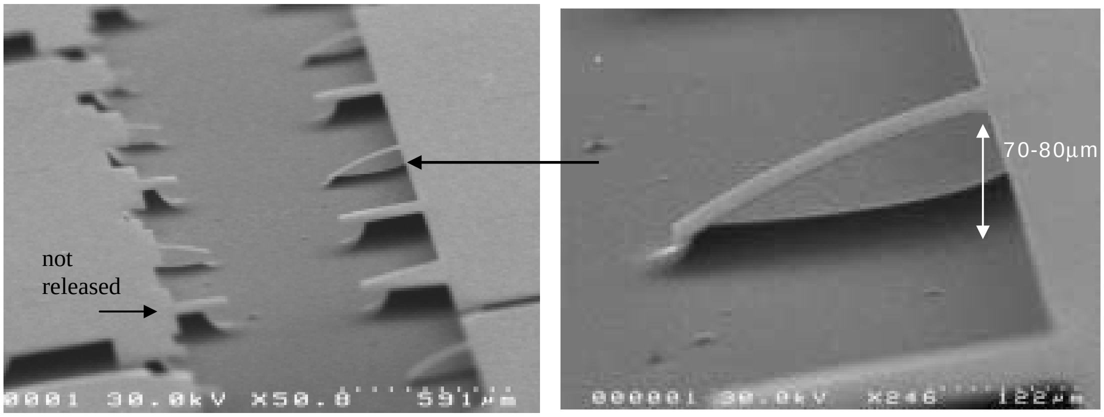

(a) (b)

Figure 4.14 Large downward deflection of released bimorph actuators due to unbalanced stresses in the stack. (a) Multiple devices on die and (b) close up of 280 μm device making contact with etched sc-silicon substrate.

The bimorph microactuators were tested and, due to pinholes and other defects, it was discovered that the two platinum layers were electrically shorted. Since the top platinum covered the entire island, all 20 devices on each island were shorted. This was true for all islands tested. A separate etching step was required to isolate each device. Due to time constraints, and the lack of an appropriate photolithography mask, a pulsed laser cutter was used to ablate material in an effort to isolate the devices. This was done to about 10 devices. The procedure was successful on two devices and a tip deflection with an applied electric field was observed. The modified devices could not handle high voltages or cycling and so quantitative data could not be collected. The laser treatment probably introduced additional defects in the PZT, which assisted in breakdown at the perimeter at moderate fields.

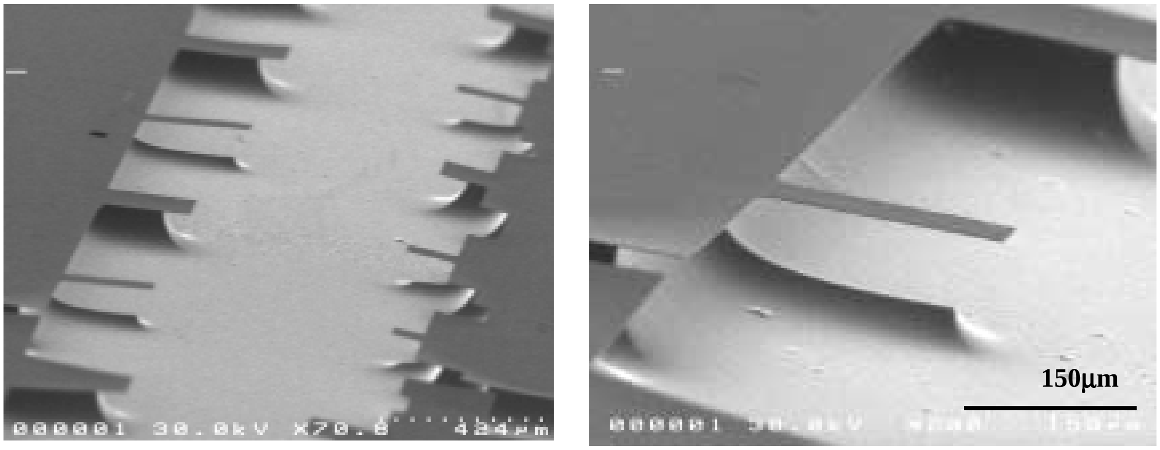

(a) (b)

Figure 4.15 Bimorph actuators after annealing at 650°C for five minutes. Most devices are flat and some bend up slightly. (a) Several devices and (b) close-up view of 230 µm long device.

4.4 Conclusions

Released cantilever actuators exhibited out-of-plane bending due to an imbalance in the residual stresses of the constituent films. An analysis based on beam theory dictated that the equal moments above and below the neutral place must exist to obtain flat structures. With out precise knowledge or control of the material properties, a methodology was conceived to obtain this required condition. This method was successful and allowed the fabrication of functioning switches. It was discovered however, that the curvature and hence the stresses were not stable. After a series of experiments, this was attributed to the possible hydration/dehydration of the sol-deposited zirconia barrier layer. The residual stress of the zirconia was observed to become more tensile with time and exposure to ambient air, and become more tensile after thermal treatments. To solve this problem, two alternatives were investigated: sputtered titanium oxide barrier layers for unimorph actuators, and bimorph structures. PZT films deposited on sputtered titania barrier layers were shown to exhibit ferroelectric and dielectric properties comparable to those deposited on zirconia films. Bimorph actuators were fabricated, and though shorting prevented actuation, the fabrication reveal two important advantages. First, the inherent symmetry of the bimorph structure lends itself more favorably to stress balancing, and hence flat cantilevers. Second, tailoring the post-release annealing allows control of the curvature of the structures, and can enhance the yield dramatically.

References

---

[1] M. Madou, Fundamentals of Microfabrication, CRC press, 1997.

[2] J. F. Shepard, S. Trolier-McKinstry, M. Hendrickson, R. Zeto,“Properties of PZT thin films as a function of in-plane biaxial stress,” Proc. 10th IEEE ISAF, pp. 161-165, 1996.

[3] D. L. Smith, Thin-film Deposition Principles and Practice, McGraw Hill, 1995.

[4] G.G. Stoney, “The Tension of Metallic Films Deposited by Electrolysis,” Proceedings of the Royal Society of London, vol. A82, pp.172-175, 1909.

[5] K.E. Petersen, “Silicon as a mechanical material,” Proc. of IEEE, 70(5), pp.420, 1982.

[6] E.P. EerNisse, “Stress in thermal SiO_2 during growth”, Applied Physics letters, 35(1), pp. 8–10, 1979.

[7] R. Brenier, A. Gagnaire, “Densification and aging of ZrO_2 films prepared by sol-gel,” Thin Solid Films, 392, pp. 142-148, 2001.

[8] G. Atanassov, J. Turlo, J. K. Fu, Y. S. Dai, “Mechanical, optical and structural properties of TiO_2 and MgF_2 thin films deposited by plasma ion assisted deposition,” Thin Solid Films, 342, 1999.

[9] E. Hong, Surface micromachined peristaltic pumps using lead zirconate titanate film, Ph.D. thesis, The Pennsylvania State University, 2004.

[10] B.A. Tuttle, J.A. Voigt, T.J. Garino, D.C. Goodnow, R.W. Schwartz, D.L. Lamppa, T.J. Headly, M.O. Eatough, “Chemically prepared $Pb(Zr,Ti)O_3$ thin films: the effects of orientation and stress,” Proc. 8th Int. Sym. Appl. Ferroelectrics, 344, 1992.

[11] K. Yao, S. Yu, F. Tay, “Residual stress analysis in ferroelectric $Pb(Zr_{0.52}Ti_{0.48})O_3$ thin films fabricated by a sol-gel process,” Appl. Phys. Lett., 82(25), pp. 4540-4542, 2003.

---

[12] M. Sekimoto, H. Yoshihara, T. Ohkubo, "Silicon nitride single-layer x-ray mask," J. Vac. Sci. Tech., 21(4), pp. 1017-1021, 1982.

[13] A. Mehner, H. Klumper-Westkamp, F. Hoffman, P. Mayr, "Crystallization and residual stress formation of sol-gel-derived zirconia films," Thin Solid Films, 308-309, pp. 363-368, 1997.

[14] W.R. Cook Jr., D.A. Berlincourt, F. Scholz, "Thermal expansion and pyroelectricity in lead titanate zirconate and barium titanate," J. Appl. Phys, 34(5), pp. 1392, 1963.

[15] X. Liu, Z.G. Liu, J. Lin, J.M. Liu, " Microstructure and electrical properties of ferroelctric $Pb(Zr_{0.53}Ti_{0.47})O_3$ films on Si with TiO_2 buffer layers", J. Phys Condensed Matter 12, pp. 9189 (2000)

[16] S. Seifried, M. Winterer, H. Hahn, " Nanocrystalline titania films and particles by chemical vapor synsethis," Chem. Vap. Deposition, 6(5), pp. 239-244, 2000.

[17] F. Xu, F. Chu, S. Trolier-McKinstry, "Domain wall motion and its contribution to the dielectric and piezoelectric properties of lead zirconate titanate films", Journal of applied physics, 89(2), 2001.

[18] R.C. Hibbeler, *Mechanics of materials, Prentice-Hall,* 1994.

Chapter 5

Device Characterization

5.1 Cantilever microactuators

Experiments to quantify the quasi-static, field-induced characteristics of the d_{33} mode unimorph microactuators were performed. The deflection of zirconia buffered devices, with a small upward curvature, fabricated on polysilicon was measured. Flat devices were used to measure the resonance frequency in vacuum. The curvature and deflection of a titania buffered actuator fabricated on SC-Si was also measured.

5.1.1 Unimorph microactuators

Figure 5.1 shows the sign convention for all the actuator deflection measurements with the PZT surface at the support taken as the origin. Initial deflection experiments on unimorph actuators yielded nonsensical results that led to the supposition of a post-poling relaxation effect. To test this hypothesis, a virgin packaged cantilever (L=280μm) was poled at room temperature for 20 min at 100V(167KV/cm). The field was removed and the tip deflection was measured as a function of time. The results are shown in figure 5.2. Since the poling of ferroelectric materials is accompanied by a strain as the domains align with the field, it was expected that poling the devices would result in a small permanent downward deflection. Upon removal of the field a 3 μm change in tip deflection was observed, however after 30 minutes, perhaps due to the elastic restoring force, this deflection was lost and the cantilever returned to its original curvature. Poling at elevated temperatures or exposure to ultraviolet light is sometimes used to lock in the domain

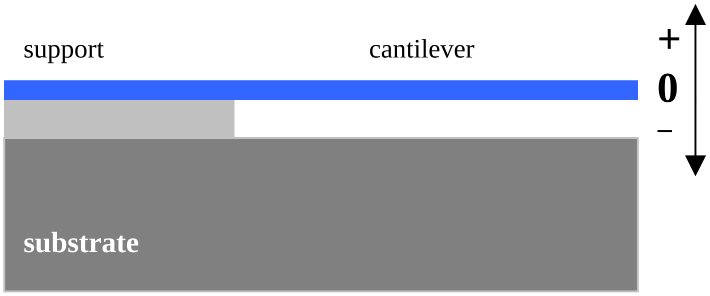

Figure 5.1 Sign convention for actuator deflection measurements. Positive deflection is away from substrate, with the PZT surface at the support as the origin.

states.[1,2] This technique has also been used to improve the aging behavior of PZT films.[3] The same device was subsequently used to test deflection versus the applied voltage. The voltage was changed, and the deflection was measured once per minute. The results are shown in figure 5.2, with the line representing the theoretical deflection calculated using equation 2.3 including the IDE factor. The deflection hysteresis is likely due to poling since the last measurement was made only a few minutes after the field was at a maximum. The change in slope at about fifty volts can be attributed to anticlastic bending which causes an increase in the stiffness of the beam.

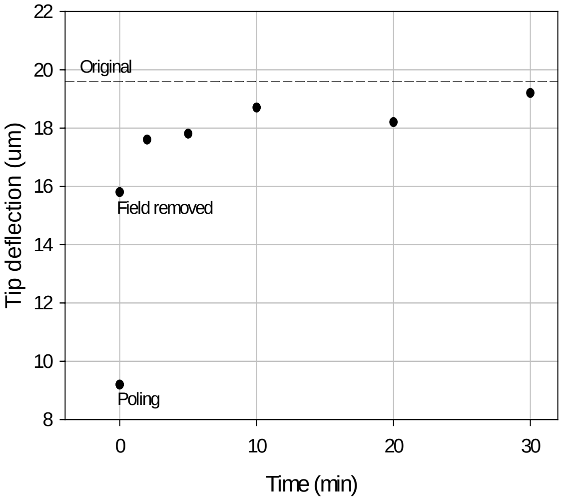

Figure 5.2 Poling relaxation

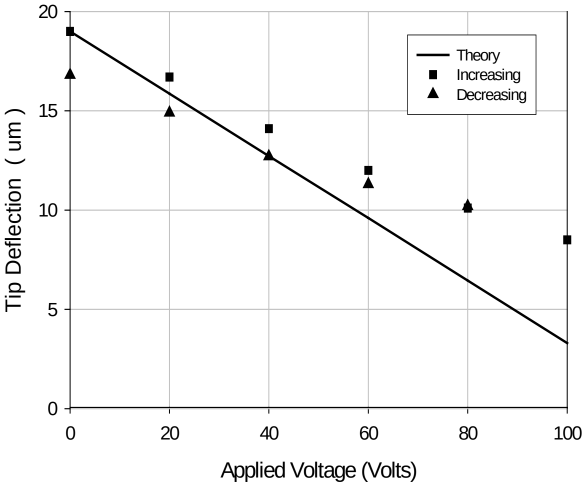

Figure 5.3 Deflection vs. actuation voltage

The MEMS design and analysis software CoventorWare, formerly known as MEMCAD, was used to simulate the deflection of the microactuators. A finite element model was created to confirm and help explain the origin of the observed non-linear behavior. The device modeled was a d_{33} mode bilayer unimoph actuator with various widths, a length of 400μm, and total thickness of 2 μm. Figure 5.3 shows the field-induced tip deflection results from the numerical modeling and the calculation using equation 2.3. No IDE factor was included in either analysis, as the field is assumed uniform. From the model, the curvature across the width of the cantilever indicates that the non-linear behavior is due to anticlastic bending. The figure also shows that the deflection is reduced as the width is increased from 20μm to 400μm. As discussed in chapter two, when the width is large compared with the thickness, a larger portion of the beam is in a state of plane stress. The decrease in deflection with width however could also be a result of anticlastic bending.

Due to squeeze damping, the resonance frequency of unimorph actuators fabricated on

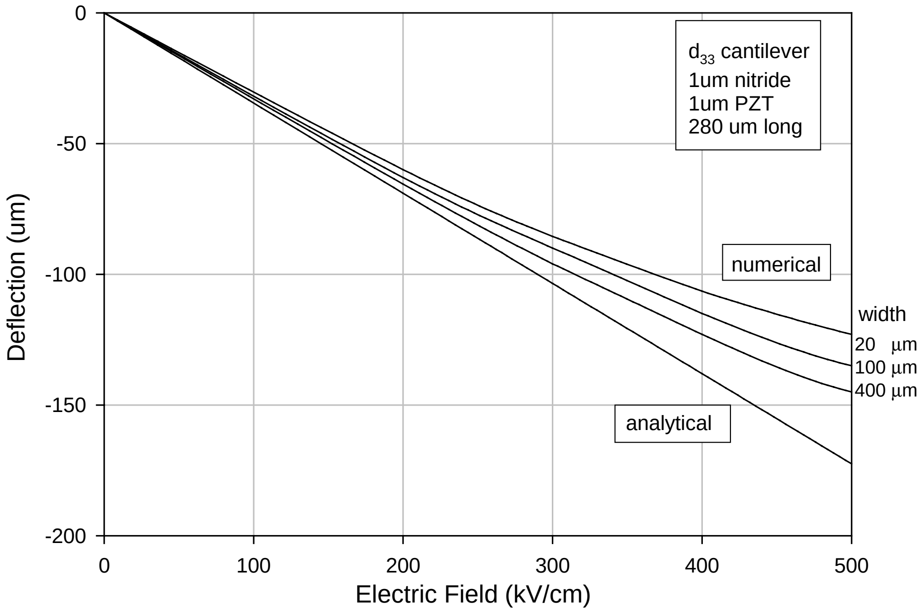

Figure 5.4 Comparison between analytical and numerical solutions for the field-induced deflection in a d_{33} mode bilayer unimorph. Finite element model predicts expected non-linear behavior.

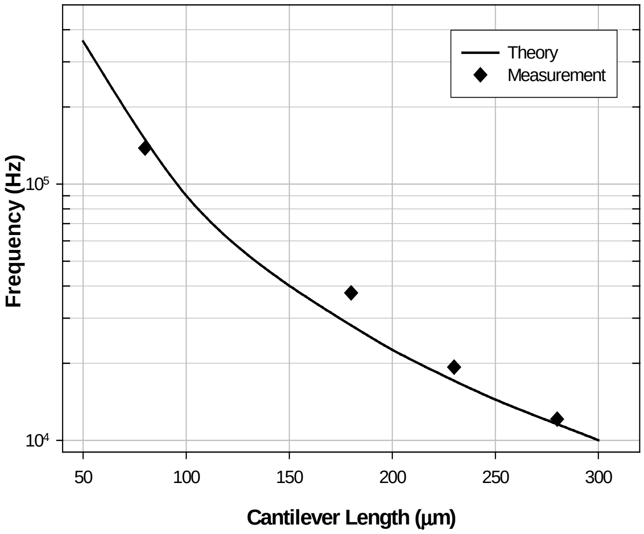

Figure 5.5 Unimorph vacuum resonance

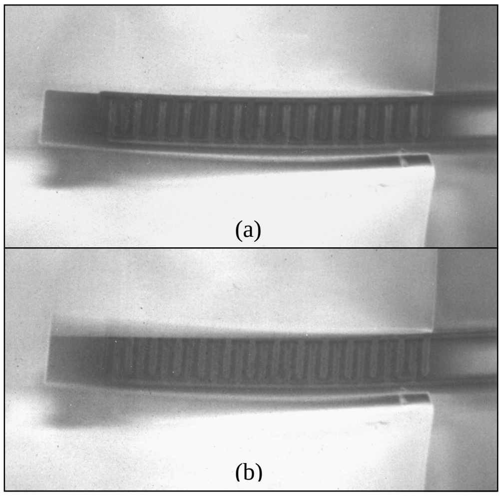

Figure 5.6 SEM image of unimorph excited off (a) and at resonance (b).

two microns of sacrificial polysilcon was measured under vacuum in a SEM. Resonance was determined by measuring the impedance as a function of frequency using an HP4194A impedance analyzer. Shown in figure 5.4 are the measured frequencies for various length devices and a theoretical curve calculated using equation 2.10. Figure 5.5 shows two SEM images of a 280 µm long unimorph excited by 600 mV off-resonance at 11 kHz, and at resonance at 12.86 kHz. The increased tip displacement at resonance is evident from the images.

5.1.2 Zirconia buffered unimorph actuators

Although many titania buffered unimorphs were cracked, several good devices were packaged and tested. A 280 µm long and 100 µm wide device was poled with 200 volts (333 kV/cm) at room temperature for 15 minutes. The field was removed and the deflection was observed and compared with the original deflection. There was no significant change after 20 minutes. The tip deflection versus applied voltage was

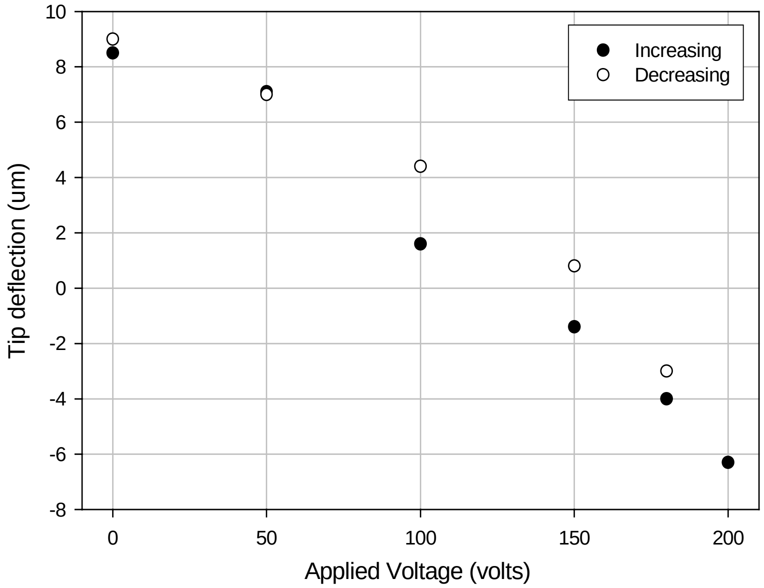

Figure 5.7 Measure tip deflection of titania buffered unimorph with increasing and decreasing voltage.

measured immediately after, and the results are shown in figure 5.6. Surprisingly, the deflection with increasing field is very linear, not exhibiting the expected decreasing slope resulting from anticlastic bending. The difference in deflection at 100 volts was also not expected. Figure 5.7 shows an interference microscope image of the device with the maximum applied voltage (200 volts). These results indicate that the PZT is piezoelectric, and that titania buffered unimorph microactuators can function properly. With additional understanding, sputtered titania buffer layers may be a viable alternative to sol-gel deposited Zirconia.

5.2 Switching Characteristics

The switching characteristics of devices based on d_{33} mode unimorph actuators is presented in this section. The switching speed was measured and a model is introduced to support the results and explain the relationship between the relevant parameters. Switching RF signals up to 100 MHz was also demonstrated using a switch based on a tapered d_{33} mode unimorph actuator.

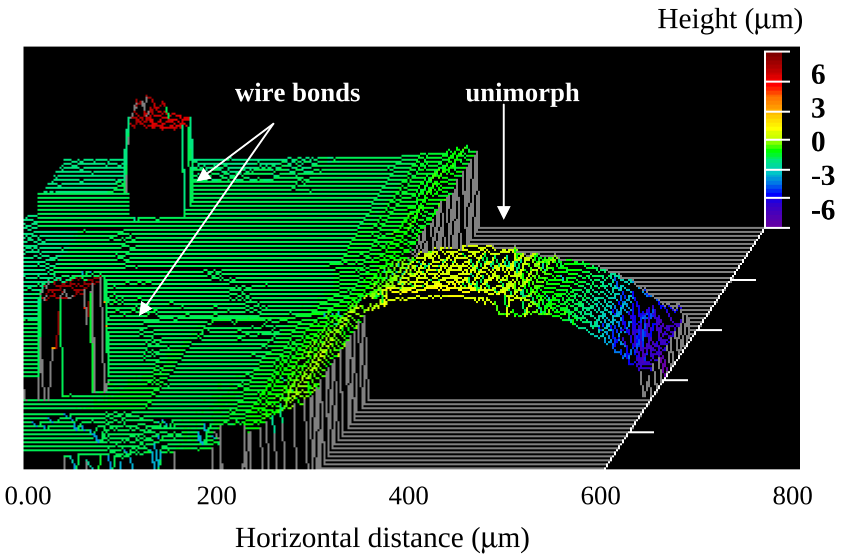

Figure 5.8 Interference microscope image of unimorph microactuator with titania buffer layer. Downward deflection from +9 μm to 15 μm with 200 volts applied (333 kV/cm).

5.2.1 DC switching characteristics

An SEM image of the device used to test the switching characteristics is shown in figure 5.8 and is based on a d_{33} mode unimorph actuator of 230μm in length, 100μm width and with a resonance frequency of 19kHz. The contacts are of the SAC2 design. The electrical set-up to measure and record the switching characteristics of the devices is shown in figure 5.9a. Resistor R_1 (300kΩ) limits the current through the switch contacts, while R_2 (10kΩ) is used to protect the device. Figure 5.9b shows the operation of the switch in response to a one Hertz square wave (20 Vpp + 10 volts d.c). The ten volts were used to make the device flat. The trace confirms the operation of the device by the switch opening and closing with the applied signal. A subsequent test showed operation at 100 Hz with a drive signal of 20 Vpp. The figure shows the device closing in about 2 μs and opening in about the same time. The highest working frequency attained for this device was 500 Hz. This frequency limit was a result of squeeze damping of the air between the switch and the substrate. Operation at lower pressures is expected to increase the maximum working frequency.

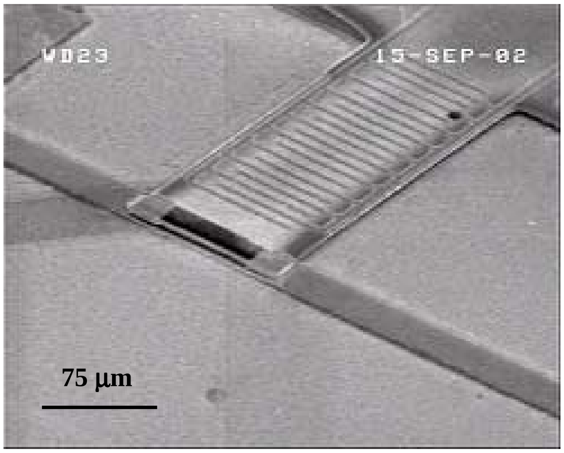

Figure 5.9 Device used in switching experiments. Based on d_{33} mode unimorph 100 μm long and 230 μm wide, f_n = 19kHz.

A series of tests explored the response of the same device to short pulses. Figure 5.10a shows an oscilloscope trace of a 30 volts, 4 μs pulse and the switch response. The noise seen on the bottom trace during switching is a result of coupling between the electrodes and contact. Figure 5.10b shows the response to a pulse of higher voltage but same duration: 50 volts, 4 μs. As can be seen, the switching-on time is decreased from 2 μs to about 1.5 μs while the switching-off time remains constant.

5.2.2 Analysis of switching speed

A simplified analysis of the switching time begins with a dynamic model for a one-degree of freedom system. The equation of motion is given as,

$$F_{ext} = m\frac{d^2z}{dt^2} + b\frac{dz}{dt} + kz \qquad (5.1)$$

where m is the mass, z is the position of the tip at time t, and k is the spring constant of the cantilever. $F_{ext,}$ is an external force and is equal to the blocking force (F_b) generated by the piezoelectric effect. All forms of damping including squeeze damping have been

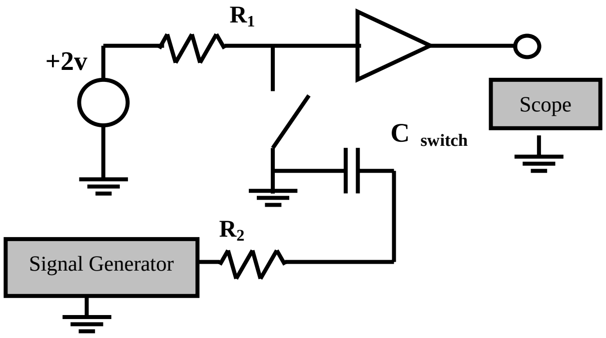

(a)

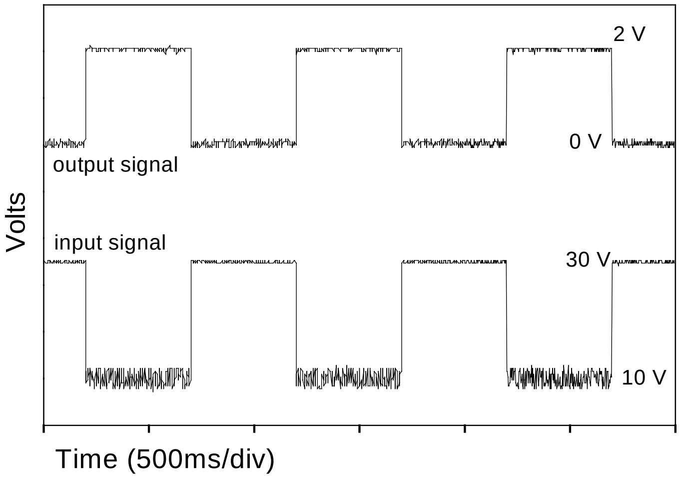

(b)

FIG. 5.10 (a) Measurement setup (b) Switching response (output) to a 1 Hz 20 $V_{peak-peak}$ + 10 V_{dc} square wave (input)

ignored; b=0. The blocking force is modeled as a step function by ignoring the IDT electrode capacitance charging time, and material mechanical relaxation. With the tip displacement and velocity set to zero as boundary conditions, the particular solution is given by,

$$z(t) = \frac{F_b}{k} - \frac{F_b}{k}\cos(\omega_n t) \tag{5.2}$$

where the natural frequency $\omega_n = 2\pi f_o = \sqrt{k/m}$. The time ($\tau_{on}$) required to close the gap, δ, can be obtained from equation (7) as,

$$\tau_{on} = \frac{1}{2\pi f_o}\cos^{-1}\left(1 - \frac{\delta}{z_o}\right) \tag{5.3}$$

z_o is the static deflection, F_b/k. For this device δ=1μm, z_0=19μm @50V (calculated), f_0=19kHz (calculated) and by (5.3) τ_{on}=2.7μs, which is comparable to the measured value. Since z_0 is proportional to the driving voltage, the larger the driving voltage, the shorter τ_{on}, and is consistent with experiments. The turn-off time however, is determined

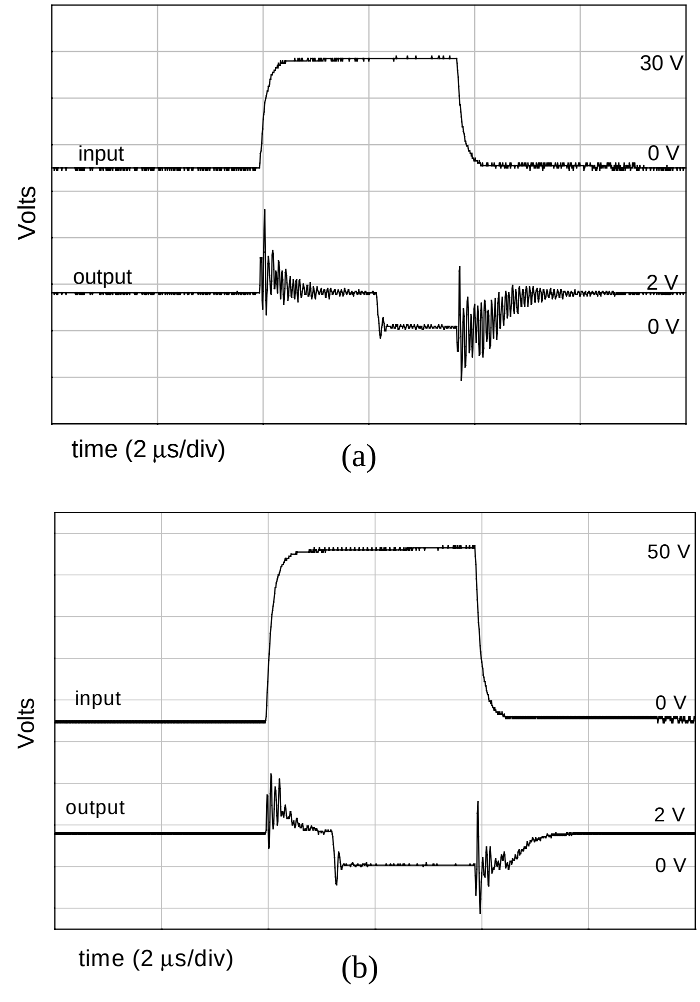

(a)

(b)

Figure 5.11 Switching response (output) to 30 volt (a) and 50 volt (b) 2 μs pulse (input).

by the gap spacing and the natural frequency rather than the applied voltage, and is consistent with the data. Piezoelectrics offer the ability to drive the switch off, reducing τ_{off}, by applying a small negative voltage. Electrostatic switches do not allow for this unless a top electrode is fabricated. By expression (5.3) we see that there is a design trade-off between the off-state isolation (which is a function the gap spacing δ), the switching speed, and the applied voltage. Fast switching compared with resonance frequencies has also been observed in electrostatic switches, with the fastest reported electrostatic switch closing in two microseconds with a bias of 73 volts.[4]

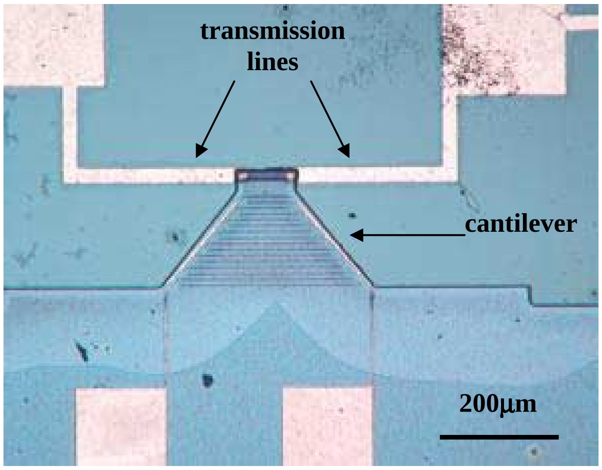

Figure 5.12 Switched based on tapered cantilever design used in RF measurements. Actuator is 150 µm long and 100µm wide at free end with a 40° taper.

5.2.3 RF switching characteristics

Basic tests were performed at frequencies up to 100 MHz to characterize the switching behavior of RF signals. The oxidized silicon substrate and the transmission lines design, were not optimal for RF frequencies. During the testing, the RF signal applied to the transmission lines was generated, and measured, using an HP4194A gain/phase analyzer. The device used for these tests is shown in figure 5.11 and is based on a tapered cantilever design with an angle of 40°. Figure 5.12 shows the transmitted power as a

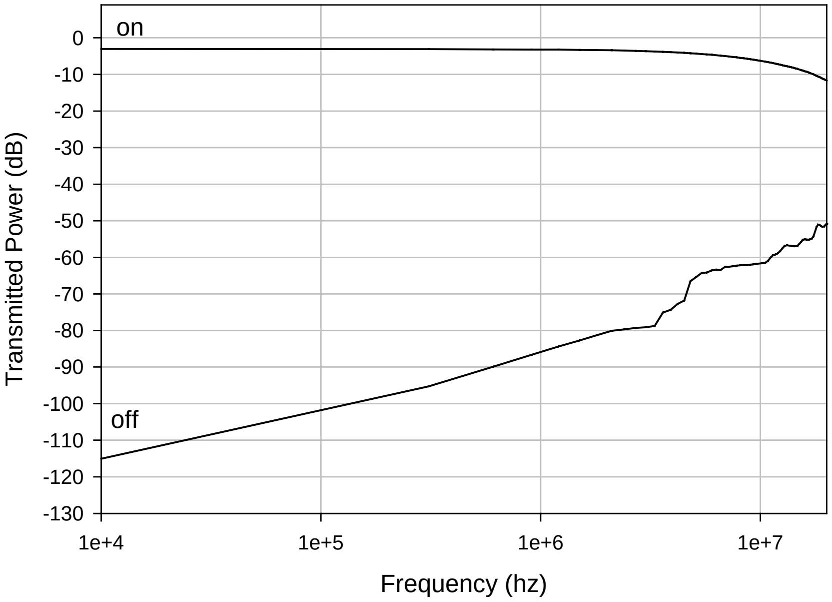

Figure 5.13 On and off transmitted power frequency sweep 10 kHz to 20 MHz.

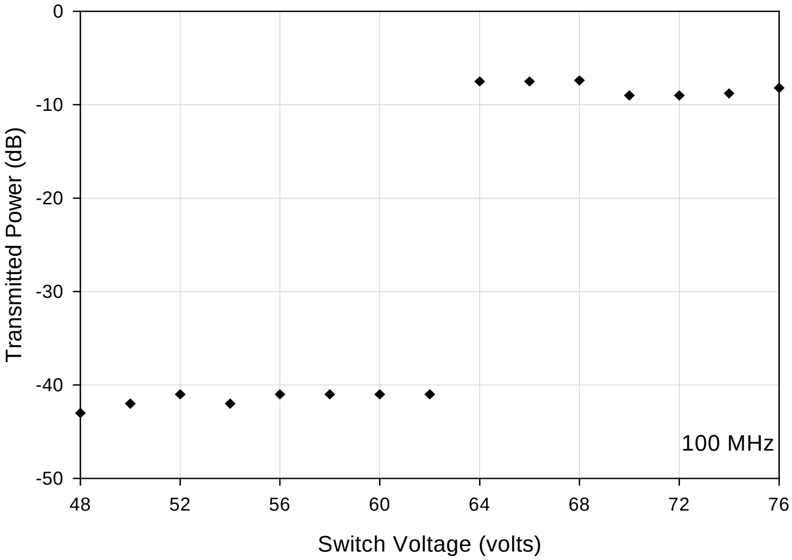

Figure 5.14 Transmitted power as a function of actuation voltage.

function of frequency for the device in the on and off states up to 20 MHz. Figure 5.13 shows the transmitted power as a function of applied voltage at 100 MHz. In principle, as the contact comes closer to the transmission lines and the gap is closed, the series capacitance should increase, decreasing the impedance. From figure 5.2, a two-micron gap is closed in approximately 12 volts and so a gradual change in transmission should be observed. The abrupt change in transmission could be due to a gap of less than two microns, or a very small capacitance due to the small area of the contact. Regardless the mechanism, the observed abrupt change in transmitted power at 64 volts is a desirable characteristic for RF MEMS switches.[5]

5.3 Conclusions

Deflection measurements were made on two unimorph microactuators. A relaxation effect was observed in the deflection after poling, likely resulting from a loss in domain alignment. A zirconia buffered actuator 280 µm long was observed to deflect 10 µm with 100 volts (166 kV/cm). A titania buffered actuator of the same length deflected 15 µm with 200 volts (333 kV/cm). Computer modeling showed deviations from linearity in the deflection versus applied electric field. It is suspected that anticlastic bending and actuator width affect the deflection characteristics. The resonant frequencies of actuators of various lengths was measured under vacuum, and agree well with theory. PZT based MEMS switches were demonstrated and switching speeds below 2 µs were observed. A tapered switch was used to test the characteristics of switching an RF signal. An isolation of >60 dB was measured up to 10 MHz.

References

---

[1] W.L.Warren, D.Dimos, G.E. Pike, B.A.Tuttle, M.V.Raymond, “Voltage shifts and imprints in ferroelectric capacitors,” Appl. Phys. Lett., 67, pp. 257-266, 1995.

[2] J. Lee, R. Ramesh, V.G. Keramidas, W.L. Warren, G.E. Pike, J.T. Evans Jr., “Voltage offsets in (Pb,La)(Zr,Ti)O_3 thin films,” Appl. Phys. Lett., 66, pp. 1337, 1995.

[3] R.G.Polcawich, S.Trolier-McKinstry, “Piezoelectric and dielectric reliability of lead zirconate titanate thin films,” Journal Materials Research, 15(11), pp. 2505-2513, 2000.

[4] M-A Gretillat, F. Gretillat, N. F. de Rooij, “Micromechanical relay with electrostatic actuation and metallic contacts,” J. Micromechanics and Microengineering, 9(4), pp. 324-331, 1999.

[5] C.B. Freidhoff personal communication (2002)

Chapter 6

Conclusions & Future Work

6.1 Conclusions

This thesis discussed the development of fast micromachined switches, with a low actuation voltage, and cantilever actuators based on piezoelectric lead zirconate titanate thin films.

Device Design A design was developed for a piezoelectric microswitch employing a cantilevered bender actuator. The bender actuator was utilized to magnify the available displacement. A metal contact at the free-end makes and breaks electrical contact with gold transmission lines. The longitudinal (d_{33}) actuation mode was chosen for two reasons. First, the d_{33} coefficient is about two times larger than the d_{31} coefficient and therefore a larger strain is possible for the same field. Larger strains allow for lower actuation voltages in switches. Second, the maximum tip deflection for the d_{33} mode is generated in the downward (toward the substrate) direction. This allowed the transmission lines to be on the substrate, reducing fabrication complexity by eliminating the need for flip-chip bonding or additional structures. An interdigitated electrode (IDE) configuration was used to generate the required in-plane electric field. An analysis of the quasi-static deflection and blocking force of the microactuators was undertaken. A relation between the elastic properties and thickness ratios of the films, and the actuation characteristics was observed. The analysis included a model for the IDE and concluded that the generated deflection and force for the d_{31} mode are several times larger than the

d_{33} mode. The lesser deflection of the d_{33} mode is a result of the lower electric field due to the inter-electrode spacing, and due to the lost piezoelectric strain in the volume beneath the electrodes. In addition, the performance of the bimorph is superior to either mode unimorphs. Since the switching speed is a function of the resonant frequency of the structure, the dynamic characteristics were studied. It was shown that the resonant frequency could be increased by tapering the geometry. The effective piezoelectric and elastic parameters applicable to micro-scale actuators was investigated. It was concluded that in a state of plane strain, the deflection and blocking force for the d_{31} mode unimorph and bimorph are increased slightly. A small decrease in the deflection of d_{33} mode unimorphs was predicted.

Fabrication Process The switch design was successfully realized using a surface micromaching process refined over numerous iterations. A cornerstone of the reliable processes was the elimination of the acid based wet release, and the adoption of gas-phase etching of sacrificial silicon using xenon difluoride. Eliminating stiction and damage to the PZT in this manner, resulted in a dramatic increase in cantilever yield. Two processes for the machining of contacts and transmission lines, post film deposition, were demonstrated. The etch rates of the films using ion-beam etching were evaluated, and the stack was patterned using this etch process. Due to the poor resolution, and difficulty with removal of the photoresist residue, a hard masking technique was investigated. By adding oxygen during milling, the etch rate of titanium and chromium masks were reduced yielding a selectivity over PZT of 3 to 1. These hard masks were incorporated successfully in the fabrication of microactuators. The affect of ion-beam etching on the ferroelectric and dielectric properties of PZT films was also investigated. Consistent with the literature, it was found that PZT film exposure to Ar ion bombardment, as in the ion-beam etching process, resulted in a drop in the remanent polarization and a shift in the polarization – electric field loop. This degradation in the properties however, was fully recoverable by hot plate annealing in atmosphere at 450°C. Films protected by both the photoresist and metal masks showed no degradation of the ferroelectric properties indicating the viability of the etch process for the delineation of ferroelectric films and multilayer stacks.

Producing flat cantilevers was the greatest challenge in demonstrating functioning microswitches. Based on a rudimentary analysis of the residual stress and cantilever curvature mechanisms, a methodology was devised for producing flat structures. This systematic approach led to the demonstration of the first functioning switches. A quantitative investigation into the residual stresses, and stress mechanisms, of the films and stack was conducted. It was discovered that the stress of the sol-del deposited zirconia barrier layer was not stable when exposed to atmosphere. The change in stress was attributed to the hydration of the film as a result of its supposed porosity. The stress of the other films in the stack was evaluated and found to be stable. Based on the results, it can be concluded that sol-gel zirconia deposited by the manner described in this work, is not suitable for freestanding MEMS. Reactively sputtered titanium oxide was therefore explored as an alternative barrier film. It was found that PZT films deposited on 100 nm of titania exhibited ferroelectric properties comparable to those deposited on zirconia. Cantilever actuators were fabricated with the new barrier material and shown to actuate. The large fraction of devices that developed cracks indicated the possibility of large stresses and that the process is still immature.

Due to the symmetric nature of the bimorph, and its predicted superior performance, this structure was explored as an alternative to the unimorph actuators. A fabrication sequence was developed and microbimorphs were produced. From a fabrication perspective, the bimorph structure offers a two-fold advantage. First, the inherent symmetry favors low curvature upon release. Second, by annealing the top electrode after release, the curvature can be controlled. Increasing the deflection requires only a higher temperature anneal. The curvature of the released bimorph actuators was found constant up to 300°C – an excellent trait for MEMS switches embedded in hot environments. Due to the large surface area and pinholes, the bimorph actuators were electrically shorted and could not be tested.

Device Characterization The deflection as a function of applied voltage was measured for zirconia and titania buffered unimorph actuators. Both actuators had an initial upward curvature. A maximum deflection for the zirconia buffered actuator of 10 μm was observed at 100 volts (160 kV/cm). The electrically induced deflection matched the calculated deflection well up to about 40 volts. The change in slope at 50 volts was attributed to a stiffening of the structure due to anticlastic bending. To see if this was indeed the reason, a finite element model was constructed. Results from the model confirmed the non-linear relationship between applied voltage and deflection, and the occurrence of transverse or anticlastic bending. The model also showed that the deflection was smaller for wider beams. The large actuation voltage is, in part, a result of the IDE configuration. Due to the IDE microfabrication, the supposed benefits of the d_{33} mode are mitigated and a lower switch actuation voltage is likely achievable with the d_{31} mode. The deflection characteristics for a titania buffered actuator were also measured. A maximum deflection of 15 μm was obtained for a 280 μm long device at 200 volts (333 kV/cm). These results suggest that with further work, titania might be an effective barrier layer for PZT MEMS.

Working switches based on zirconia/PZT unimorph actuators were tested. A switching speed of about 2 μs was measured with an actuation voltage of 30 and about 1.5 μs with 50 volts. A simple model was constructed and used to evaluate the switching speed. The model predicted a switching speed of 2.7μs. The maximum working frequency of the tested switches at atmospheric pressure was found to be 500 Hz. This is likely due to squeeze damping and is expected to increase with lower pressures. A tapered switch was used to test the switching of RF signals up to 100 MHz. The transmitted power as function of frequency was measured, and showed an isolation of more than 60 dB up to 10 MHz. The transmitted power as a function of voltage showed a step-wise behavior with the switch turning on abruptly at 64 volts - a desirable trait for RF systems.

Initial Objectives Of the five objectives stated at the end of chapter one, four were met fully, and the last was partially completed. These accomplishments are presented again here.

1) A piezoelectric, PZT based, MEMS RF switch with high speed switching was designed.

2) An actuator microfabrication process was developed.
    a. Titania barrier layers was investigated as an alternative to the zirconia.
    b. Bimorphs actuators were investigated to control curvature and improve yield.
3) A switch microfabrication process was developed.
4) Functioning devices were successfully fabricated demonstrated.
5) Device characteristics were measured.
    a. General switching behavior was characterized.
    b. Simple deflection measurements were performed on slightly curved actuators.

6.2 Future Work

Microactuators A complete characterization of the performance of microactuators, both unimorph and bimorph is important for several reasons. First, as was discussed in chapter five, the switching characteristics of the devices are inherently related to those of the actuator. An improvement in MEMS switches can therefore only result from an understanding of the relationship between the device design, and operating characteristics. Second, cantilever microactuators and microsensors are universal, and current and future applications are quite numerous. The knowledge base gained therefore has applications extending far beyond RF switches.

Although preliminary measurements were made, the primary goal is still to measure the tip deflection and blocking force as a function of applied electric field, as well as the spring constant of the actuators. The devices, with both titania and zirconia barrier layers, need to be flat and have ample space for deflection. Devices and various lengths and widths need to be tested in order to evaluate the effect of these parameters on the performance. The deflection can be measured using an interference microscope and the tip deflection might be measured using the stylus of either an atomic force microscope or a profilometer. This would depend on the stiffness of the actuator under study and the stylus. Measurements of individual actuators would be repeated numerous times to check for hysteresis and repeatability. Results obtained from a single device are not significant and not much can be deduced from the data. By measuring many devices of the same dimensions, a statistical analysis could be applied to the results to determine confidence limits on the observed deflection and blocking force.

Titania Actuators Elimination of the pyrochlore phase in PZT films deposited on sputtered titania may be achieved by increasing the titania barrier thickness. Samples can be produced to find the minimum thickness required. The stress stability of these thicker titania films would have to be evaluated. Unimorph actuators would be fabricated using the new titania thickness and observe if cracking at the edges occurs after release.

Bimorph Switches The success had with the fabrication of bimorph actuators and the larger calculated deflection and force, suggest that these structures are well suited for producing switches. The greater symmetry, along with post-release annealing, greatly promotes and facilitates low curvature actuators. The next step in this development would be to open the second window, contact the bottom platinum layer, and test the actuators. Although attractive as switch actuators, upon initial inspection bimorphs would introduce new problems. First it needs to be determined if the bottom platinum layer could be used as a contact to short the transmission lines. This would result in coupling between the drive signal and the RF signal – not a desirable situation if the drive signal contains high frequency components that cannot be filtered. To isolate the bottom platinum electrode from the contact a dielectric could be used but at high frequencies, the thickness would have to be large to again prevent coupling. This argument indicates that the platinum would need to be removed from the end of the cantilever to provide adequate isolation. If the bottom platinum is patterned before the first PZT deposition, then an alignment strategy to etch the complete stack is required. Development of switches based on bimorphs hence requires that these and other unforeseen issues be resolved.

Switches As with the characterization of the microactuators, numerous devices must be tested in order to gain a true understanding of the performance of these devices. Testing would be performed on switches of various dimensions measuring the switching speed of devices with differing geometries. In addition, as the maximum working frequency is only 700 Hz, this measurement should be made as a function of pressure. As the pressure is reduced, the squeeze-damping changes and alters the resonance frequency of the devices and hence the switching characteristics.

Vita

Steven Gross

Steven Gross was born in Turin, Italy in 1971. He received a Bachelor's of Science degree from the University of Massachusetts, Amherst, in Mechanical Engineering along with a minor in Physics in 1995, and was inducted into Pi Tau Sigma, the International Mechanical Engineering Honor Society. After graduation, he worked briefly for General Electric Aircraft Engines as a manufacturing/quality engineer and subsequently with Osram Sylvania as an industrial engineer. In 1999, Steven obtained a Master's of Science degree in Electrical Engineering from the Pennsylvania State University for work on the characterization of the electrostricitive strain in P(VDF-TrFE) copolymer. His doctoral work involved the development of micromachined switches based on piezoelectric PZT films.